CEREBRAL WASTE CLEARANCE: MEASUREMENTS AND APPLICATIONS

by

JASLEEN KAUR

A dissertation submitted in partial fulfillment of the
requirements for the degree of

DOCTOR OF PHILOSOPHY IN BIOMEDICAL SCIENCES:

MEDICAL PHYSICS

2023

Oakland University
Rochester, Michigan

Doctoral Advisory Committee:

Yang Xia, Ph.D., Chair
Quan Jiang, Ph.D., Co-Chair
Bradley J Roth, Ph.D.
Li Zhang, M.D.
Zhenggang Zhang, M.D., Ph.D.
Michael Chopp, Ph.D.

Dedicated to

The Universe for making everything happen.
My loving husband, Amanveer Singh, who inspires me and always has my back.
My Parents and Parents-in-law, who provide unwavering support to me.
My late brother, Jagjit Singh, who will always be loved and remembered.
My Furry cat baby, Pumpkin, who melts my heart and makes me a better person.
Blessed to have you all!!

ACKNOWLEDGMENTS

These studies were performed through the Department of Neurology at Henry Ford Hospital. I am grateful and obliged to my adviser, Quan Jiang, Ph.D., for his unwavering encouragement, inspiration, and direction during my research years. I extend my sincere gratitude to Yang Xia, Ph.D. for his invaluable support and help with the academic matters. My genuine thanks and admiration to Bradley J Roth, Ph.D. for having faith in me and supporting me in a selfless manner. Special appreciation to Li Zhang, M.D. for her expert guidance, supervision in the projects, and extensive discussions. I am indebted to Zhenggang Zhang, M.D., Ph.D. and Michael Chopp, Ph.D. for generously sharing their expertise and time in improving all the projects and publications. I am thankful to the entire Neurology Lab group, especially Dr. Gaungliang Ding, Qingjiang Li, Dr. Edward Boyd, Dr. Lian Li, Dr. Hao Luo, Min Wei, and Dr. Yong Lu, for all of their assistance and knowledge while working with them closely. I want to extend my gratitude to the faculty and staff members of the Physics Department, Oakland University and the Neurology Department, Henry Ford Hospital for their guidance and assistance throughout the years. Thanks to all dissertation committee members for their invaluable time and participation. Last but not the least, heartfelt gratitude to all the rats who were ethically used in the research projects. I thank the journals for permitting me to reproduce my papers in this dissertation. I am also thankful for the grant support from the National Institutes of Health (RF1 AG057494, R01 NS108463, R21 AG052735, R21 AG070173).

Jasleen Kaur

ABSTRACT

CEREBRAL WASTE CLEARANCE: MEASUREMENTS AND APPLICATIONS

by

JASLEEN KAUR

Adviser: Yang Xia, Ph.D., Quan Jiang, Ph.D.

Cerebral Waste clearance (CWC) is an essential process for brain homeostasis, which is required for the healthy functioning of all cerebrovascular and parenchymal brain cells. This dissertation features our current understanding of CWC, both within and external to the brain parenchyma. We describe the role of the cerebrospinal fluid (CSF) and its exit routes in mediating CWC. Recent discoveries of the glymphatic system and meningeal lymphatic vessels (mLVs), and their relevance to CWC and various neurological conditions are highlighted. Controversies related to CWC research and potential future directions are presented.

This dissertation is divided into seven chapters that discuss investigations that used magnetic resonance imaging (MRI) and confocal microscopy imaging to evaluate the recently identified CWC routes, namely the glymphatic system and the mLVs. The dissertation begins with an introduction (Chapter- 1). It proceeds with background (Chapter- 2) based on two published peer-reviewed ‘review’ articles, and three research projects based on one submitted, one published ‘original research’ articles (Chapters- 3, 4) and one project with negative results (Chapter- 5). Among the three projects described in this dissertation, the first project (Chapter- 3) aimed to investigate the controversy of

glymphatic convective bulk flow in the interstitial spaces and explore the association of perivascular macrophages (PVMs) in assisting the glymphatic system for CWC. Our findings solidify the glymphatic system hypothesis and indicate the interaction of PVMs with the glymphatic CSF influx along the arteries and glymphatic CSF efflux along the veins. The second project (Chapter- 4) aimed to examine the changes in the glymphatic system in rats with glioblastoma multiforme (GBM) and our results identify reduced glymphatic influx and clearance due to GBM. The third project (Chapter- 5) aimed to assess the mLVs as a potential efflux pathway of the glymphatic system under healthy and diabetic mellitus (DM) conditions. Our results suggest that mLVs are not the major efflux pathway of the glymphatic system, which is a negative result. The dissertation then discusses a translational issue for clinical MRI evaluation of the glymphatic system (Chapter- 6) based on a submitted 'review' article and concludes with a summary and future directions (Chapter- 7).

TABLE OF CONTENTS

TABLE OF CONTENTS—Continued

TABLE OF CONTENTS—Continued

TABLE OF CONTENTS—Continued

TABLE OF CONTENTS—Continued

TABLE OF CONTENTS—Continued

LIST OF FIGURES

LIST OF ABBREVIATIONS

CWC	Cerebral waste clearance
BBB	Blood-brain barrier
CSF	Cerebrospinal fluid
ISF	Interstitial fluid
MRI	Magnetic resonance imaging
CE-MRI	Contrast-enhanced magnetic resonance imaging
T1WI	T1-weighted imaging
DWI	Diffusion-weighted imaging
ADC	Apparent diffusion coefficient
DTI	Diffusion tensor imaging
ICM	Intra-cisterna magna
GFP	Green fluorescent protein
AQP4	Aquaporin-4
Aβ	Amyloid-beta
AD	Alzheimer’s disease
SVD	Small vessel disease
TBI	Traumatic brain injury
DM	Diabetic mellitus
CNS	Central nervous system
CLNs	Cervical lymph nodes
dCLNs	Deep cervical lymph nodes

ECM	Extracellular matrix
PVMs	Perivascular macrophages
PBMs	Parenchymal border macrophages
MMP	Matrix metalloproteinase
GBM	Glioblastoma multiforme
TSC	Time signal curve
ROIs	Regions of interest
ICP	Intracranial pressure
mLVs	Meningeal lymphatic vessels
iNPH	Idiopathic normal pressure hydrocephalus
DTI-ALPS	DTI based analysis along the perivascular space
PC-MRI	Phase contrast MRI
CBF	Cerebral blood flow

LIST OF PUBLICATIONS

Chapters- 2 and 6 in this dissertation are based on the following first author peer-reviewed 'review' articles:

I. **Kaur, J.**, Davoodi-Bojd, E., Fahmy, L. M., Zhang, L., Ding, G., Hu, J., Zhang, Z., Chopp, M., Jiang, Q. (2020). Magnetic Resonance Imaging and Modeling of the Glymphatic System. *Diagnostics (Basel), 10*(6). doi:10.3390/diagnostics10060344

II. **Kaur, J.**, Fahmy, L. M., Davoodi-Bojd, E., Zhang, L., Ding, G., Hu, J., Zhang, Z., Chopp, M., Jiang, Q. (2021). Waste Clearance in the Brain. *Front Neuroanat, 15*, 53. Retrieved from https://www.frontiersin.org/article/10.3389/fnana.2021.665803.

III. **Kaur, J.**, Davoodi-Bojd, E., Ding, G., Chopp, M., & Jiang, Q. (2023). Clinical MRI Evaluation of Glymphatic Function. *submitted to NMR in Biomedicine*.

I, being the copyright holder, have the permission to reproduce I & II open access 'review' articles.

Chapters- 3 and 4 in this dissertation are based on the following first author peer-reviewed 'original research' articles:

I. **Kaur, J.**, Boyd, E., Ding, G., Zhang, L., Luo, H., Li, Q., Li, L., Wei, M., Landschoot-Ward, J., Chopp, M., Zhang, Z., Jiang, Q. (2023). The Association between Glymphatic System and Perivascular Macrophages in Brain Waste Clearance. *submitted to Scientific Reports*.

II. **Kaur, J.**, Ding, G., Zhang, L., Yong, L., Luo, H., Li, L., Boyd, E., Li, Q., Wei, M., Zhang, Z., Chopp, M., Jiang, Q. (2023). Imaging glymphatic response to glioblastoma. *Cancer Imaging, 23*(1), 107. doi:10.1186/s40644-023-00628-w

I, being the copyright holder, have the permission to reproduce II open access 'original research' article.

CHAPTER ONE

INTRODUCTION

Homeostasis is critical for the proper functioning of the human body, particularly, homeostasis of high-energy consuming organs like the brain. The substantial amount of toxic metabolic by-products/interstitial waste products (such as CO_2, lactate, proteins including amyloid-β (Aβ) and tau proteins, etc.) released into the brain due to the high metabolic activity of neurons in the brain, require rapid exit by several CWC mechanisms. Otherwise, the accumulation of these metabolic by-products/interstitial waste products may initiate and or exacerbate several neurological diseases, including the accumulation of Aβ in Alzheimer's disease (AD) and tau in traumatic brain injury (TBI) [1-12]. Therefore, regulating the entry and exit of various substances in the brain is essential for proper neuronal functioning and healthy aging [13-15]. There are two distinct systems set in place to help the brain with this type of regulation, the CSF and the vascular systems. Interestingly, the CSF and BBB are unique to the central nervous system (CNS).

The idea that CSF is involved in CWC via a network of perivascular spaces has existed since at least 1974 [16]. But it did not receive much attention until 2012 when Nedergaard and colleagues expanded our understanding of the role of CSF in CWC and proposed the glymphatic system [17]. They and others demonstrated that glymphatic system dysfunction is associated with a broad range of neurological diseases including, but not limited to, AD, stroke, TBI, multiple sclerosis, diabetes, and chronic traumatic encephalopathy, suggesting its involvement in most neurodegenerative diseases [1, 11,

17-23]. Although dysfunction of the glymphatic system and its impact on CWC is related to a variety of neurological diseases, controversial aspects concerning the convective bulk flow of CSF/ISF within the brain parenchyma and the role of aquaporin-4 (AQP4) water channels in solute transport in the glymphatic system still exist [24-27]. Augmenting the importance of the glymphatic system's role in CNS homeostasis is the (re)discovery of the previously unappreciated meningeal lymphatic vessels (mLVs) in the dura [28, 29], originally proposed at the end of the 18th century [30-32]. Two independent research groups in 2015 confirmed the existence of the mLVs, and furthermore, indicated that CSF tracers utilize these mLVs for CWC. Due to the association of various neurological conditions with the glymphatic system, investigation of their interactions may lead to new approaches to reduce neurological deficits and to sustain healthy aging. Moreover, by investigating these neurological diseases using various imaging techniques, particularly prior to clinical symptom onset, we can potentially identify a therapeutic target for treatment.

This dissertation is divided into seven chapters. All chapters are based on individual papers published/submitted to journals. Due to same background context of the glymphatic system, there may be some repetition between the texts in these chapters.

Chapter- 2 of this dissertation presents background information on fluids in the brain and their functions, CWC within the brain parenchyma (including the brain stroma infiltrating the brain parenchyma such as blood vessels and perivascular spaces), and CWC external to the brain parenchyma. The brain parenchyma consisting primarily of neurons and glial cells (surrounded by ISF) is the functional tissue for cognitive and systemic management and is considered responsible for nutrient uptake, and CWC to

maintain homeostasis. The remaining structural tissue in the brain, the stroma, is comprised primarily of the blood vessels, which provide the brain with oxygen and nutrients, and connective tissue. It is important to note that CWC processes taking place within and external to the brain parenchyma in the CNS are connected and affect one another. This 'review' manuscript has been published in *Frontiers in Neuroanatomy* [33]. Furthermore, this chapter discusses the role of the glymphatic system in various neurological diseases based on current evidence and controversies and focuses mainly on new magnetic resonance imaging (MRI) modeling techniques, along with traditional computational modeling, for a better understanding of the glymphatic system function. This 'review' manuscript has been published in *Diagnostics (Basel)* [34].

Chapter- 3 aimed to investigate if diffusion in the brain interstitial spaces is sufficient to account for the intra-striatally administered tracer dynamics within the striatum and the corpus callosum of the rat brain utilizing MRI. We first addressed this argument to determine the involvement of the glymphatic system in brain waste clearance. Using contrast-enhanced 3D T1-weighted imaging (T1WI) and diffusion tensor imaging (DTI), the apparent diffusion coefficients (ADC) in the striatum and corpus callosum of the rat's brain were evaluated after the intra-striatal infusion of high molecular-weight contrast agent (Gd-albumin, 70 kD). Furthermore, perivascular macrophages (PVMs), which are immune cells located within perivascular spaces, have not been thoroughly explored for their association with the glymphatic system. Therefore, we investigated tracer uptake by PVMs and the potential association of PVMs in assisting the glymphatic system for CWC utilizing confocal microscopy imaging after intra-striatal

and intra-cisternal administrations of the tracers, respectively. This ‘original research’ manuscript has been submitted to *Scientific Reports* for consideration.

Chapter- 4 aimed to investigate the impact of glioblastoma multiforme (GBM), which is a highly aggressive form of malignant brain cancer, on the functioning of the glymphatic system in rats utilizing MRI and advanced kinetic modeling. Dynamic 3D contrast-enhanced T1-weighted imaging (T1WI) with intra-cisterna magna (ICM) infusion of paramagnetic Gd-DTPA contrast agent was used for MRI glymphatic measurements in both GBM-induced and control rats. Glymphatic flow in the whole brain and the olfactory bulb was analyzed using model-derived parameters of arrival time, infusion rate, clearance rate, and residual that describe the dynamics of CSF tracer over time. Also, the perineural pathway along the optic nerves was assessed for its functioning in GBM and control rats. This ‘original research’ manuscript has been published in *Cancer Imaging* [35].

Chapter- 5 aimed to investigate the meningeal lymphatics as a potential efflux pathway of the glymphatic system in Prox1-EGFP^{+} reporter rats under healthy (non-DM) and diabetic mellitus (DM) conditions using confocal microscopy imaging. We hypothesize that DM decreases waste clearance through the meningeal lymphatics. Although significant strides have been made in characterizing the glymphatic system pathways through perivascular routes, the efflux pathways of the glymphatic system external to the brain parenchyma remain largely unclear, mainly due to technical difficulties of performing minimally invasive in-vivo, ultra-high detection sensitivity measurements of influx and efflux pathways, and whole brain imaging.

Chapter- 6 discusses the translational issues of clinical MRI evaluation of the glymphatic system intended for early diagnosis, prevention, and treatment of various neurological conditions. Evaluation of glymphatic system function by means of MRI has thus far been largely focused on rodents due to the limitations of intrathecal delivery of gadolinium-based contrast agents to humans. Although the clinical glymphatic system-based MRI research is in its early stages, recent studies have identified promising non-invasive MRI markers associated with glymphatic system alterations in neurological diseases. This 'review' manuscript is under review by *NMR in Biomedicine*.

Chapter- 7 provides the summary of the dissertation and future directions.

CHAPTER TWO

BACKGROUND

2.1 Fluids in the brain and their functions

2.1.1 CSF production and circulation

CSF is produced in the human brain at a rate of about 0.3-0.4 ml/min, mainly by specialized ependymal cells such as choroid plexus epithelial cells located in each of the ventricles. The CSF travels from the lateral ventricles to the third ventricle via the interventricular foramen of Monro and enters the fourth ventricle via the cerebral aqueduct of Sylvius. CSF then enters the central canal of the spinal cord via the obex and also reaches the subarachnoid space via the median aperture of Magendie and the two lateral apertures of Luschka [36-39]. CSF is eventually drained via the arachnoid villi, perineural spaces of spinal and cranial nerves, and meningeal lymphatics. However, part of the CSF is also proposed to enter the brain parenchyma via the periarterial spaces of the penetrating arteries, mixes with interstitial waste products and ISF, enters the perivascular spaces (alongside veins by the glymphatic system or along arteries by intramural periarterial drainage (IPAD) pathway), and finally drains via the CWC pathways, as indicated in **Fig- 2.1A**. Recent studies, however, suggest that there may be additional, previously underappreciated mechanisms involved in CSF production and regulation [40, 41]. It has been suggested that in addition to the choroid plexus, capillaries located inside the brain parenchyma also generate CSF [42].

2.1.2 CSF functions and flow behavior

The CSF has multiple functions in the brain including, providing buoyancy and buffer against injury, and by serving as the CWC route, it maintains CNS homeostasis. The CSF is also very important for removing high molecular weight waste products and other debris during recovery from brain injuries, and it provides a pathway for nutrients and hormones to promote the brain's normal development [43, 44]. The flow of CSF in the cerebral aqueduct, in the ventricles, and the subarachnoid space is pulsatile due to the cardiac flow (arterial hemodynamics in the choroid plexus) and pulmonary respiration [36, 38, 39, 45-47], facilitating rapid influx via the periarterial spaces into the brain parenchyma. However, within the brain parenchyma, CSF flow may be either via convective bulk flow and/or diffusion.

2.1.3 ISF production and circulation

ISF is a filtrate of plasma secreted at the BBB of the capillary walls. ISF surrounds neural cells, makes its way through intercellular clefts of the neuropil, and is present in the extracellular spaces of the gray and white matter within the brain parenchyma. It contains interstitial waste products excreted by the cells due to cellular metabolism and nutrients from capillaries through diffusion. ISF acts as an intermediate between blood capillaries and brain cells for rapid delivery of oxygen and nutrients (such as glucose, lactate, and amino acids, etc.) for reliable cellular activity. ISF also acts as a vehicle for rapid removal of the cellular waste by-products (such as CO_2, lactate, etc.), and cell-to-cell communication [43, 48-51]. The CSF acts as a sink for the ISF, and the CSF-ISF exchange helps in the removal of interstitial waste products from the brain parenchyma.

2.2 Barriers (BBB and blood-CSF barrier) and their functions

CSF and ISF are similar in composition, however, the CSF is mainly present in the cerebral ventricles and subarachnoid space covering the entire brain, whereas the ISF is extracellular fluid and surrounds the cells in the brain parenchyma. Regulation of ionic composition (such as Na^+, Cl^-, K^+, Ca^{2+}, Mg^{2+}, etc.) and volumes of these fluids is essential for the brain cells to function effectively and is supported by barriers such as the BBB and blood-CSF barrier [43]. The BBB separates blood in the vasculature from ISF and cells within the brain parenchyma and helps in maintaining the ionic composition of ISF. The BBB restricts the movement of many substances to/from the brain parenchyma while delivering substrates (glucose, amino acids, O_2, etc.) for brain cell metabolism and helps in CWC [14, 43].

Unlike the cerebral capillary endothelial cells that form the BBB, the endothelial cells of capillaries that supply the choroid plexuses and the circumventricular organs are fenestrated/leaky and have no tight junctions that is an essential property of the BBB [52]. The ependymal cells are a layer of cuboidal neuroepithelial cells along the ventricles facing the ventricular CSF and the ependymal cilia mediate the CSF movement [52]. The choroidal epithelial cells are connected by tight junctions and constitute the blood-CSF barrier [14, 43, 53]. The blood-CSF barrier separates blood in the capillaries from the CSF, regulating the passage of molecules between them.

2.3 Waste clearance within the brain parenchyma

Some neurodegenerative diseases are related to the improper accumulation of cellular waste by-products [54]. Among them, misfolded proteins are the most difficult to clear from the brain, and their build-up leads to diseases such as AD [54]. Although

chaperone proteins in brain cells help proteins fold correctly and limit their aggregation, folding and aggregation errors do occur, and some proteins are more vulnerable than others. If misfolded proteins are not identified and removed from the brain parenchyma, then these interstitial waste products can cause or exacerbate neurological diseases [55-57]. Aβ and tau proteins are the two most concerning neurotoxic waste proteins due to their accumulation in the brain and association with neurological diseases such as AD and TBI [1-12, 21, 58]. Aβ is a small protein fragment that is cleaved from a larger amyloid precursor protein, which extends from the inside to the outside of brain cells. Aβ eventually forms amyloid-plaques in the extracellular spaces of the brain parenchyma, found in AD patients [59, 60]. These Aβ aggregates impair communication between neuronal cells, cause nerve inflammation, and are a common cause of dementia in the elderly. In transgenic mouse models of AD, Aβ has been associated with cognitive deficits, tau-phosphorylation, synaptic dysfunction, and neuronal death [61].

Tau protein is an intracellular protein that mainly exists in neurons and helps stabilize microtubules. They are released to the extracellular space after a rapid increase in neuronal activity [62]. When misfolded and hyperphosphorylated, tau proteins create neurofibrillary tangles which disrupt neuronal signal transmission, cause microtubules to disassemble, and promote mitochondrial dysfunction. In addition to Aβ protein, tau protein is also one of the main features of AD [63, 64]. In a recent study, it has been suggested that both extracellular Aβ plaques and intracellular tau neurofibrillary tangles work together in synergy in generating AD [65]. The accumulation and movement of tau protein in the extracellular space have been related to many neurodegenerative diseases, such as chronic traumatic encephalopathy, Parkinson's disease, prion disease, etc. [10,

66-69]. Since the Aβ and tau accumulation impairs neurons, they need constant maintenance and repair, which are essential for learning, memory, and neurological function.

The brain parenchyma (which consists of the neurons and glial cells) is infiltrated by the brain stroma (which contains the blood vessels and perivascular spaces) and lacks lymphatic vessels. CWC at this level consists of the interaction of the brain parenchyma with the blood vessels and perivascular spaces, which eventually help transport the waste products outside the cranium. Therefore, waste products can only be removed from the brain parenchyma by: a) CSF pathways via the perivascular (as indicated in **Fig- 2.1B(i)**) and periaxonal/perineural routes; b) the vascular pathway via the BBB as indicated in **Fig- 2.1B(ii)**. Waste products which are small in size (such as CO_2, K^+, lactate, etc.) exit via the BBB. Whereas waste products which are larger in size, polar in nature (such as sucrose, inulin, albumin, dextran, etc.), and lack specific transporters to cross the BBB, exit via perivascular or periaxonal/perineural routes. However, special solutes which are larger in size, such as Aβ [70-72], insulin [73], and transferrin [74], also exit via the BBB with the help of transcytosis. Yet other substances are first metabolized to other products (such as glucose metabolizing to CO_2 and water) before exiting. However, Na^+, Cl^-, and water are transported by both vascular and CSF pathways [75].

2.3.1 CSF pathways via the perivascular and periaxonal/perineural spaces

The idea that CSF infiltrates the brain parenchyma and is involved in CWC has been around for a long time. There is an agreement in the field regarding the utility of the perivascular spaces in CSF-related CWC. However, the exact pathway undertaken by CSF-related CWC inside the brain parenchyma, as pertaining to the perivascular spaces,

is under debate. Thus far, two pathways have been strongly put forward: the intramural periarterial drainage (IPAD) and the glymphatic system. There appears to be consensus in the field regarding the utility of the periaxonal/perineural spaces in CSF-related CWC (which span CWC within and external to the brain parenchyma).

2.3.1.1 Intramural periarterial drainage (IPAD)

A study in 2008, in which various soluble tracers were injected into the corpus striatum of mice, demonstrated diffusion of tracers through the extracellular spaces of the brain parenchyma and then convective bulk flow drainage along the basement membrane of capillaries and arterial walls [76]. This indicated that ISF and waste products drain via the same pathway, termed IPAD [76]; joining the CSF in the subarachnoid space or dissipation at the base of the skull for further drainage into the cervical lymph nodes (CLNs) and/or blood. A recent study in mice demonstrated that following injection of fluorescent Aβ into the cisterna magna, the CSF tracer enters the brain parenchyma along pial-glial basement membranes [77]. It then mixes with ISF and interstitial waste products and exits along the basement membranes in the walls of capillaries and the basement membranes between smooth muscle cells in the walls of the cortical arteries (IPAD pathway) [77], as indicated in **Fig- 2.1B(i)**. Other studies using mathematical and computational models suggest that arterial pulsations, which were initially considered as a motive force for IPAD, cannot be the only driving force for the IPAD pathway to efficiently account for the experimental observations [78]; however, vasomotion induced by contraction and relaxation of cerebrovascular smooth muscle cells is suggested to be a more plausible driver for IPAD [79].

2.3.1.2 The glymphatic system

In 2012, Nedergaard and colleagues performed a series of fluorescence microscopy experiments that demonstrated the path of CSF circulation within the brain parenchyma via a network of perivascular spaces, termed the glymphatic system [17]. The glymphatic system hypothesis describes subarachnoid CSF entry into the brain parenchyma through the periarterial spaces, mixing with parenchymal ISF and interstitial waste products facilitated by AQP4 water channels embedded in astrocytic end-feet, and drainage through perivenous spaces surrounding the veins [11, 17, 18, 54, 80-83] as indicated in **Fig- 2.1B(i)**. So whereas the IPAD pathway demonstrated CSF brain parenchymal circulation through the separate periarterial basement membranes (convective influx along pial-glial basement membranes as suggested in the glymphatic pathway and the efflux along basement membranes between smooth muscle cells in the walls of arteries [77]), the glymphatic system pathway demonstrated CSF circulation via the perivascular spaces surrounding the arteries and veins.

Specifically, Nedergaard and colleagues injected tracers into the cisterna magna of mice and two-photon imaging studies of these mice indicated that the tracer size matters when determining brain parenchymal tracer distribution [17]. Small molecular weight CSF fluorescent tracer (Texas Red–dextran-3 (TR-d3): molecular size, 3 kD) injected into mouse cisterna magna was observed within periarterial spaces and within brain parenchyma within 30 minutes; indicating unrestricted movement of small molecular weight tracers into the interstitium. However, large molecular weight CSF fluorescent tracer (fluorescein isothiocyanate-dextran-2000 (FITC-d2000): molecular size, 2000 kD) predominantly remained confined in the periarterial spaces; highlighting

the role of the 20 nm-wide astrocytic end-feet gap junctions [17]. The observation that both small and large molecular weight tracers entered perivascular spaces alongside arteries indicate that the transport is facilitated by CSF convective bulk flow via perivascular spaces.

Transport by AQP4 water channels is thought to play a dominant role in mediating brain parenchymal entry of CSF tracer from the periarterial spaces [17, 84], which is driven by the hydrostatic pressure generated by arterial pulsations as proposed in the glymphatic system [85]. Cerebral arterial pulsations are said to drive the CSF convective bulk flow in the perivascular spaces and are the key contributors of CSF entry into the brain parenchyma allowing CSF-ISF fluid exchange in the glymphatic system [19, 85]. Additionally, astroglial AQP4 supports the convective bulk flow of ISF through the brain parenchyma to drive the interstitial waste products (e.g., Aβ) to the perivenous spaces; in AQP4-null mice, the interstitial waste products clearance is reduced by nearly 70% (demonstrated using intraparenchymal injections in mice) [17].

The CSF mixed with ISF and interstitial waste products such as Aβ are drained primarily through the perivenous spaces, which may then reenter associated CSF compartments, either within the ventricles (for internal cerebral veins), or in the subarachnoid space (for caudal rhinal veins) [17], or may drain to the blood across the vasculature via specific transport mechanisms at the BBB [17, 75, 86-88]. The waste products, which reach the CSF in subarachnoid space may then exit the cranium either via arachnoid granulations or mLVs or along cranial and spinal nerves [75, 86, 89] as indicated in **Fig- 2.1A**. However, and as an attempt to reconcile the IPAD and the glymphatic system pathways, some speculate that the CSF-ISF mixture may recirculate in

the brain parenchyma via periarterial spaces and accumulate within the basement membranes of smooth muscle cells, triggering neurological conditions [17]. There are still some controversial aspects related to the glymphatic system hypothesis primarily based on convective bulk flow within the brain parenchyma and AQP4 dependent solute transport within the brain parenchyma.

The glymphatic system impacts the physiology of the body, such as sleep [81, 83], body posture [90], heart rate [4], aging [4, 22, 58, 85, 91-95], anesthesia [96], etc. Slight changes in normal physiology can affect the clearance rate of interstitial waste products from the brain. The glymphatic system in mice is most dynamic during sleep and removes beta-amyloid with exceptional efficiency, with a more than two-fold increase in clearance rate [83]. Anesthetics also affect the glymphatic system, and a nearly 30% increase in solute transport can be seen in rats anesthetized with dexmedetomidine plus low-dose isoflurane as compared to high-dose isoflurane only [96]. Results from contrast-enhanced MRI (CE-MRI) in rats validated by quantitative optical imaging in mice demonstrated the role of body posture/positioning on the glymphatic system; indicating that the right lateral position is the most efficient for waste clearance as compared to supine and prone positions [90]. During aging, ventricular shrinkage and significant reductions in CSF production and pressure, along with decreased arterial pulsatility (due to arterial stiffening) lead to significant reductions in glymphatic system function (~80-90% reduction in old mice compared to young mice), leading to a critical increment in beta-amyloid deposition within the brain parenchyma [4, 22, 85, 91-94].

The glymphatic system helps in the removal of Aβ, a protein which is a trademark of AD, from the brain [7, 17, 97]. Decreased glymphatic clearance and increased Aβ accumulation have been seen in the aged brain [93], sleep deprivation [81], depression [8], and obstructive sleep apnea [98], whereas voluntary exercise [99] and Omega-3 polyunsaturated fatty acids [100] promote the glymphatic clearance of Aβ. Dysfunction/impairment of the glymphatic system has been associated with several neurological diseases including AD [5, 6, 101], TBI [10-12, 22, 102-104], small vessel disease (SVD) [105, 106], stroke [107-109], diabetes [20], microinfarcts [110, 111], migraines [112], glaucoma [113], etc. In most of the studies relating glymphatic system impairments to neurological diseases, it is not clear if the impairments are the cause or the result of these diseases. Further investigation of neurological diseases and their interactions with the glymphatic system may lead to new approaches to reduce neurological deficits and to sustain healthy aging. Moreover, by investigating these neurological diseases using various imaging techniques, particularly prior to clinical symptom onset, we can potentially identify a therapeutic window for treatment.

2.3.1.3 Periaxonal/perineural spaces

Various studies have indicated that there is a fast efflux of ISF and waste products along white matter/axon tracts, in addition to the perivascular spaces discussed above [38, 51, 114-116]. As a gross extension of this, perineural spaces along all twelve pairs of cranial nerves are also involved in CSF-related CWC; particularly the olfactory (CNI) and optic (CNII) cranial nerves, as they are anatomically and histologically considered as white matter tract extensions [117]. All the cranial nerves' nuclei/cell bodies lie within the brain parenchyma. CNI and CNII emerge/originate from the cerebrum (CNI from the

olfactory bulb and CNII from the lateral geniculate nuclei), and the rest of the cranial nerves (III-XII) have their cell bodies in the brainstem. After emerging, cranial nerves travel within the skull and then exit via foramina in the skull to reach their final destinations [117, 118]. Therefore, perineural spaces accompanying the cranial nerves start within the brain parenchyma and make their way outside the brain parenchyma, along the cranial nerves as indicated in **Fig- 2.1A**.

2.3.2 Vascular pathway via the blood-brain barrier (BBB)

The vascular CWC involves the BBB. The BBB has long been studied, particularly for its structure and role in pharmaceutical drug entry. However, its role in CWC has been understudied.

The BBB consists of continuous endothelial cells joined together with tight junctions which are further supported by pericytes, the basement membrane, and the astrocytic end-feet. The microvascular network in the brain is composed of arterioles, venules, and capillaries. They all display the BBB properties; however, capillaries represent the largest microvasculature with the tightest junctions at the BBB as compared to arterioles and venules [119, 120]. The BBB makes the vascular pathway highly selective, as compared to the CSF pathways, due to the presence of tight junctions in the gaps between endothelial cells as indicated in **Fig- 2.1B(ii)**. The effective exchange of products between the brain parenchyma and blood is very important for the influx of various nutrients and the efflux of metabolic waste products-critical for proper neuronal functioning. Glucose, CO_2, O_2, water, and amino acids are some of the major substances that must be rapidly transported in and out of the brain parenchyma in large quantities to maintain brain homeostasis. Mechanisms of BBB transfer [14, 75] include:

2.3.2.1 Passive, non-specific transport

A passive, non-specific transfer can occur via a paracellular or transcellular pathway. Due to the presence of tight junctions at the BBB, the paracellular pathway is highly restricted compared to the transcellular pathway; however, this pathway is still permeable to small solutes. Most of the passive, non-specific transfer occurs via a transcellular pathway in which waste products such as water, ethanol, methanol, glycerol, urea, isopropanol, ethylene glycol, etc. must pass/diffuse through the endothelial cell, crossing both the luminal and abluminal membranes [75]. Yet other non-specific substances such as 'BBB-impermeable' MRI tracers which classically cannot cross the BBB from the blood to the brain parenchyma, may be able to cross the BBB from the brain parenchyma to the blood; suggesting BBB directionality to non-specific substances, as an important area of research requiring further investigation [87, 88].

2.3.2.2 Efflux transporters

Various efflux transporters are present at the BBB such as monocarboxylate transporter 1 (MCT1) for the efflux of lactic acid and small monocarboxylic acids, glucose transporter 1 (GLUT1) for the transport of glucose, etc. [75]. Various ATP-Binding Cassette (ABC) transporters (such as P-glycoprotein, MRP2, and BCRP) [121-123] and solute carrier (SLC) transporters are also present at the BBB. The influx of chemotherapeutic neurotoxic agents (such as vincristine and doxorubicin) from blood to the brain parenchyma are prevented by the presence of P-glycoprotein (ABC transporter) at the luminal membrane of the BBB [75, 124-127]. The absence of P-glycoprotein showed elevated drug levels (such as neurotoxic pesticide ivermectin, and carcinostatic drug vinblastine) in knockout mice brain [128, 129]. SLC transporters move the waste

products from the brain parenchyma to the endothelial cells, and then, either ABC or SLC transporters may drain these products further from the endothelial cells to the blood [75].

2.3.2.3 Transcytosis

Efflux by transcytosis includes adsorptive-mediated transcytosis (AMT) and receptor-mediated transcytosis (RMT) for the transport of large substrates across the BBB. However, there is little evidence for transcytosis in the direction of the brain parenchyma to the blood, although this parenchymal-blood transcytosis has been reported in studies involving the transport of Aβ peptides [70-72], IgG molecules [130, 131], insulin [73], and transferrin [74] via the interaction with various receptor proteins. Other non-specific substances such as albumin, inulin, sucrose, and dextran mainly exit the brain parenchyma via convective bulk flow through the perivascular spaces.

2.4 Waste clearance external to the brain parenchyma

If waste products within the brain parenchyma are eligible to directly cross the BBB from the brain parenchyma to the blood, then they straightforwardly enter the highly specialized regional parenchymal venous circulation, which eventually drains into the dural venous sinuses [132]. However, if waste products enter the CSF compartments, several efflux routes participate in CWC. Waste products that reach CSF from the brain parenchyma can be further taken out of the cranium via the proposed CSF outflow pathways: the arachnoid villi/granulations pathway and lymphatic pathways (which include peripheral lymphatic pathways via perineural spaces and meningeal lymphatic pathways) as indicated in **Fig- 2.1C**.

2.4.1 Arachnoid villi/granulations pathway

Our classic textbook understanding of the role of the arachnoid villi/granulations in CSF transport comes from a study conducted over 100 years ago [133]. Our understanding is that the CSF drains into the venous sinuses via the arachnoid villi/granulations which are located in the dura mater, providing an open unidirectional pathway connecting the meninges with the venous system [134, 135] and this is a major route of exit for the CSF as indicated in **Fig- 2.1C(i)**. However, recent studies have cast doubt on this understanding, inviting scientists to rethink the exact role and magnitude of the arachnoid villi/granulation route. Using high-resolution stereomicroscope and lymphatic-reporter mice, Ma *et al.* demonstrated that the lymphatic pathway, rather than the arachnoid villi/granulations, was the major outflow pathway for small and large molecular weight CSF tracers [136]. Moreover, an MRI study conducted on normal and hydrocephalic rats, indicated that the superior sagittal sinus was not a significant draining channel for ventricular CSF tracers compared to the azygos internal cerebral vein, suggesting direct exit of the CSF tracer via the parenchymal venous circulation as opposed to exiting via the arachnoid villi/granulations [137]. To address the role of arachnoid granulations in the outflow of CSF, a recent study investigated the morphology of the arachnoid granulations in pigs utilizing electron microscopy and immunohistochemistry. They identified the cranial arachnoid granulation-like dural gap (CAG-LDG) in the meninges adjacent to the superior sagittal sinus, however they did not find CAG-LDG in the dura mater adjacent to the transverse sinus. They also demonstrated the lymphatic endothelial cell marker, Lyve-1 in the CAG-LDG in pigs, revealing characteristics similar to the lymphatic endothelium. This study provides a

basis for further research of CSF drainage via these pathways and its relation to CWC-associated diseases in humans [138].

2.4.2 Peripheral lymphatic pathways

It has been known for a long time that CSF drains via the perineural spaces of the cranial nerves, especially the CNI in the nasal mucosa pathway for CWC into the peripheral lymphatics outside the cranium; the nasal mucosa pathway acts as a major clearance route after intracisternal or intraventricular injections [136]. However, several researchers have found drainage of CSF tracers along the perineural spaces of the other cranial nerves, complementary to the nasal mucosa pathway.

2.4.2.1 Nasal mucosa pathway

Many studies provide evidence for the nasal lymphatic pathway as the major pathway for CSF drainage, via channels in the cribriform plate of the ethmoid bone draining into the CLNs [139, 140] as indicated in **Fig- 2.1C(ii)**. Macromolecular waste solutes such as India ink, Albumin, Evans blue dye, etc. [140, 141], and immune cells such as Green fluorescent protein (GFP)-expressing CD4 T lymphocytes, GFP monocytes, etc. [142, 143], have all been shown to exit the CNS through the nasal mucosa into the CLNs. Mollanji *et al.* also demonstrated the significance of the olfactory-lymphatic route over the arachnoid villi/granulations route, and represented it as a major drainage site for CSF transport by blocking the cribriform plate in sheep, indicating an increase in the resting intracranial pressure and a significant reduction in CSF clearance [144, 145]. Moreover, studies performed in sheep, pigs, rabbits, rats, mice, monkeys, and humans using injections of yellow Microfil into the CSF compartment identified the nasal lymphatic pathway as distinctive for CSF absorption in all mammals, showing the similar

distribution of Microfil across all species [139]. More recent animal studies have also demonstrated similar findings and reached similar conclusions [136, 137, 146]. However, despite the crucial role of the nasal lymphatic pathway in the evacuation of molecular waste solutes from the CSF in various animal species, a recent *in vivo* MRI study in humans showed that, although CSF tracer (Gadobutrol) was found near/below the cribriform plate, no significant amount of tracer reached the nasal mucosa itself, which questions the presence of this pathway in , and warrants further research [147].

2.4.2.2 Other perineural spaces

CSF drainage from the subarachnoid space to the lymphatics outside the CNS is associated with the transport along cranial and spinal nerves [137, 148, 149]. Various studies have investigated the perineural routes along CNI (as discussed in the previous section) for CSF drainage into the CLNs, as the major CSF-lymphatic pathway [139, 140, 150]. Complementary to this nasal mucosa pathway, other studies have suggested the drainage of CSF tracer into extracranial peripheral lymphatics via perineural spaces of other cranial nerves. Arnold *et al.* showed the presence of contrast agent, radioisotopes in the perineural spaces of CNI, and the vestibulocochlear nerve (CNVIII) in guinea pigs a few minutes following CSF tracer injection, with most of the tracer ending up in dCLNs [151]. Kida *et al.* observed the distribution of carbon particles along the perineural spaces of CNI, CNII, and the oculomotor nerve (CNIII) following the injection of India Ink into the cisterna magna of rats [140]. Injection of radiolabeled albumin in the lateral ventricles of sheep also identified the perineural spaces along the CNI, CNII, and CNVIII [152]. Moreover, Microfil infusion in the cisterna magna of neonatal sheep showed distribution along various cranial and spinal nerves, identifying the perineural routes along the

trigeminal (CNV), the facial (CNVII), glossopharyngeal (CNIX), vagal (CNX), and hypoglossal (CNXII) nerves, with ultimate drainage into the extracranial lymphatics [149]. Lee *et al.* demonstrated MRI CSF tracer (Gd-DTPA) distribution around/inside the cochlea (CNVIII) and pronounced efflux along CNX [90]. Recently, Ma *et al.* found evidence of tracer exiting the perineural routes along the CNI, CNII, CNV, CNVII, CNIX, CNX, and accessory (CNXI) in mice after intraventricular infusion, which ultimately drained to the dCLNs [136]. Recently, Krishnamurthy *et al.* showed the distribution of MRI-labeled dextran along the spinal nerves, suggesting these nerves as the CSF outflow pathways from the spinal subarachnoid space to the lymphatics via perineural routes; as well as exit along the perineural spaces of cranial nerves (CNI, CNII, and CNV) [137]. All 12 pairs of cranial nerves and all 31 pairs of spinal nerves are surrounded with CSF in humans, which drain to regional peripheral lymphatics [153].

Although the utility of perineural spaces, peripheral lymphatic vessels, and CLNs in CWC have been extensively studied, especially after intraventricular or intracisternal injections, it remains unclear if perineural routes are the major routes for CWC after the intraparenchymal injections [136]. Moreover, it is not known if the waste solutes drain along the cranial nerves or enter the epineurium and then drain within the nerves along fascicles and/or axons [154]. Therefore, further research is warranted to investigate the exact mechanism and role of the CSF-lymphatic pathway in CWC.

2.4.3 Meningeal lymphatic pathway

The presence of the mLVs was first introduced by Paolo Mascagni, an Italian physician at the end of the 18th century [30-32]. He was an excellent anatomist, famous for his anatomical wax models with his scientific concern in lymphatic vessels in

meninges. His work presented 28 wax models on the lymphatic system including 3 body-size models. However, his ideas on lymphatic vessels were not assessed for their value by contemporary researchers and forgotten [30-32]. Mascagni's observations were finally confirmed and presented in detail in 2015 when Louveau *et al.* identified the mLVs in mice lining the dural venous sinuses and demonstrated their ability to carry fluid and immune cells (such as T cells, $MHCII^+$, $CD11c^+$, and $B220^+$, etc.) to the dCLNs [29]. They also suggested that the mLVs were the primary route for the CSF-lymphatic, as compared to the nasal mucosa pathway. Also, the mLVs seemed to form a more complex and larger network along the transverse sinus, as compared to the superior sagittal sinus. They indicated that the transverse sinus mLVs may help in ISF and interstitial waste products clearance from the brain parenchyma, following their entry into the CSF compartment through the recently discovered glymphatic system pathway. At approximately the same time in 2015, Aspelund *et al.* demonstrated the presence of the mLVs in the dura mater of the CNS in mice and their exit via foramina at the base of the skull alongside the blood vasculature (arteries, veins) and cranial nerves [28] as indicated in **Fig- 2.1C(iii)**. Their data also suggested the clearance of ISF/CSF and interstitial waste products from the brain parenchyma to the dCLNs via mLVs after they traversed the glymphatic pathway. Another study on mice showed the mLVs as the drainage channel for macromolecules and immune cells in the CSF. They also revealed certain spots called 'hot spots' along some mLVs which take up the tracer from CSF quickly after the injection as compared to other areas of the lymphatic vessels [155]. A recent study in mice showed the distinct morphological features of mLVs in the dorsal and basal dura along with their anatomical locations. They also demonstrated the basal mLVs as the

hotspot for CSF macromolecular clearance and showed the impairment of mLVs and delayed CSF clearance with aging [156].

Subsequently, the existence of the mLVs was reported using non-invasive, high-resolution clinical MRI in humans [157, 158] and non-human primates [158]. Studies using confocal microscopy confirmed the presence of these mLVs in humans and indicated that, although these vessels served as potential efflux pathways for Aβ clearance from the brain, Aβ did not deposit in or around the mLVs [2]. Moreover, experiments in mice demonstrated that impairments to the mLVs were associated with decreased macromolecular efflux through the perivascular spaces, which resulted in the accumulation of Aβ in the brain parenchyma [58]. This study also demonstrated a decrease in the diameter of mLVs in old mice and suggested the role of these vessels in AD pathology as well as in cognitive decline with aging. A recent human study identified the clearance of MRI contrast agent (Gadodiamide) in putative mLVs, and the glymphatic system and suggested the impairment of both pathways with aging [159]. Another recent study in mice demonstrated that dorsal mLVs are critical for generating an effective immune response against brain tumors [160]. Thus, the mLVs provide a route for draining macromolecules and immune cells from the CNS and therefore constitute a possible therapeutic target for the treatment of various neurodegenerative disorders.

2.5 Magnetic resonance imaging and modeling of the glymphatic system

The utility of MRI in investigating the glymphatic system has recently gained momentum. Although optical imaging techniques such as two-photon microscopy have classically dominated the field, due to its excellent spatial resolution needed to capture

small perivascular spaces, its limitations have pushed investigators towards MRI; MRI overcomes the low-penetration depth of two-photon microscopy and allows for whole-brain imaging unlike two-photon microscopy, which is only favorable in imaging small areas of the brain cortex. Beyond the use of contrast agents, image contrast in MRI can be easily altered by the elements of the imaging sequences and parameters, unlike two-photon microscopy. Moreover, different MRI methodologies can evaluate different elements of the glymphatic system. MRI is also minimally invasive and therefore can be used to study the glymphatic system *in-vivo* with minimum disruption in both animals and humans. Recent examinations of human brain utilizing MRI provided evidence suggesting that the presence of the glymphatic system in the human brain is analogous to that found in the rodent brain [161-167].

Modeling the glymphatic system using data from MRI can provide insight into the glymphatic flow pathways. Iliff *et al.* [80] demonstrated that MRI is an effective tool to study the glymphatic pathways, providing good spatial and temporal resolution of the whole rat brain. MRI modeling has been used to capture the association between glymphatic system impairments and neurological conditions. Dynamic CE-MRI, along with multiphoton imaging in mice, showed that stroke profoundly impacts the functioning of the glymphatic system. During acute focal ischemia, a rapid increase in CSF influx driven by ischemic spreading depolarizations and vasoconstriction contributes to brain edema [109]. This study is fundamentally important in changing the mechanism of stroke-induced edema from the vascular to the glymphatic system [109]. Slow waste clearance from the brain after subarachnoid hemorrhage (SAH) and ischemic stroke was demonstrated in whole brain scans using MRI [107, 108]. MRI was utilized to investigate

the impairment of the glymphatic system functioning in four stroke models in mice (SAH, embolic ischemic stroke, intracerebral hemorrhage, and carotid ligature). Severe glymphatic system impairments were demonstrated with SAH and acute embolic ischemic stroke, but not with intracerebral hemorrhage and carotid ligature [107]. We have demonstrated reduction in tracer clearance in rat models of DM compared to age matched controls using MRI [20]. *In-vivo* MRI analysis of contrast agent gadolinium-diethylenetriamine pentaacetic acid (Gd-DTPA) clearance from interstitial space, also validated by *ex-vivo* fluorescence microscopic images, showed that the clearance rate constant is decreased by three times in the hippocampus of DM rats as compared to non-DM rats [20]. MRI provided the evidence of presence of mLVs in human and non-human primates for CWC [158]. MRI study in humans also reported decreased glymphatic system and meningeal lymphatic CSF tracer clearance with increased age [95].

2.5.1 Quantitative bio-physical modeling

Mathematical modeling utilizing MRI data has been performed by various groups to better understand the dynamics of the glymphatic system flow. In these studies, mathematical models were developed expressing the dynamics of the nuclear magnetic resonance (NMR) tracer in a CE-MRI of rodents. The measured MRI signal was assumed to be proportional to the tracer concentration in the imaging voxels. Therefore, the dynamic changes of the tracer concentration could be measured by the consecutive MRI scans. The aim was to develop a mathematical model based on the tracer behavior in the tissues and underlying tissue characteristics to mimic the measured dynamic changes by MRI. Thus, solving these models could provide quantitative maps of the glymphatic dynamics and structure.

2.5.1.1 Modeling using multi-compartment kinetic framework

Lee *et al.* [90] introduced a two-compartment kinetic model based on CE-MRI data to analyze the movement of Gd-DTPA tracer (infused into the cisterna magna) for three distinct body postures in rats. The brain was divided into two sections for this experiment (infusion site and all other brain tissues). Comparing the kinetic parameters (retention and loss) for all the three postures, it was concluded that the glymphatic transport is most effective while sleeping in the lateral position and less proficient in prone and supine positions [90]. The limitation of this model is that the parameters were derived using a global input function from the infusion site instead of using local input functions separately for each region, which therefore could produce errors for the study of the glymphatic system [90]. In cerebral permeability and perfusion measurements, a global input function has long been a major source of inaccuracy [168, 169].

Our recent study presented the local input functions to visualize the more reliable glymphatic flow pathways of the Gd-DTPA tracer in rats using the two-compartment model [170]. This model: 1) utilized cluster analysis to group brain voxels into different regions with similar time signal curves of the contrast-enhanced MRI measurements, 2) computed the local input functions based on the response to the contrast agent infusion, and 3) solved the two-compartment kinetic equations for each region [170]. The limitation of this model is the absence of a diffusion term in the equations used for modeling, which may induce errors for waste clearance in the extracellular spaces of the brain.

2.5.1.2 Modeling using optimal mass transport framework

Ratner *et al.* [171, 172] fitted a mathematical model to the dynamic MRI images of rodent brain injected with Gd-DTPA tracer into the cisterna magna and utilized a 3D visualization computational tool to visualize the glymphatic flow vector fields. Here, the tracer flow was estimated between each pair of consecutive MRI images using the theory of optimal mass transport (OMT) [171, 172]. Some assumptions of this model include the injected tracer moves along the glymphatic pathway, total injected mass is conserved, and the image brightness corresponds to the tracer concentration. Glymphatic pathways were presented as color-coded maps of streamlines per voxel. The OMT algorithm demonstrated the directionality of the glymphatic system bulk flow qualitatively; but the measurements do not provide the quantitative values for directionality as well as the efflux pathways out of the brain [171, 172].

Elkin *et al.* analyzed the glymphatic pathways using the OMT algorithm with a Lagrangian framework instead of using the Eulerian framework [173, 174]. The Lagrangian approach was advantageous in envisioning the time-varying glymphatic fluid pathways in over 30 minutes in a single image [173]. Modeling based on dynamic CE-MRI data showed different responses in rats under two different anesthetics. In this model, the continuity equation for the contrast agent was modified by augmenting the diffusion term to regularize the fluid flow for continuous pathways in the glymphatic system [173].

In another study by Elkin *et al.* [174], they again used the Lagrangian approach with a modified continuity equation to more precisely model the fluid flow behavior. Regularized optimal transport procedure and flow pattern analysis (FPA) were used to

find the directional information of tracer between the time points of the initial and final observed density images from CE-MRI of normal rat brains. The major advantage of this model is that it reduces the errors by five times when compared to the customary OMT model. However, it still provides qualitative fluid flow information instead of the quantitative information [174].

In the most recent paper of vascular investigation by Elkin *et al.*, fluid motion was described by applying OMT regularized model to the human MRI data of ten patients with head and neck squamous cell carcinoma [175]. The advantages of this model are that it provides quantitative information for the fluid flow and provides a clear signal between the neighboring voxels instead of ignoring intervoxel contrast agent movements [175]. This model can be further used to track the glymphatic pathways showing both bulk flow and diffusion values which are critical for the complete understanding of the glymphatic system.

2.5.1.3 Modeling efflux using DTI

Kim *et al.* [176] used a voxelized model including a diffusion term for convective-enhanced delivery (CED) of therapeutics for the treatment of various CNS diseases. This model is of special interest, since it can be utilized to model the efflux pathways of the glymphatic system. In this model, data from DTI was used to create 3D computational CED transport models and a semi-automatic segmentation scheme was used to assign the transport properties on a voxel-by-voxel basis [176]. The voxelized model approach is advantageous because of being quicker, in contrast with the tedious slice-by-slice segmentation [176].

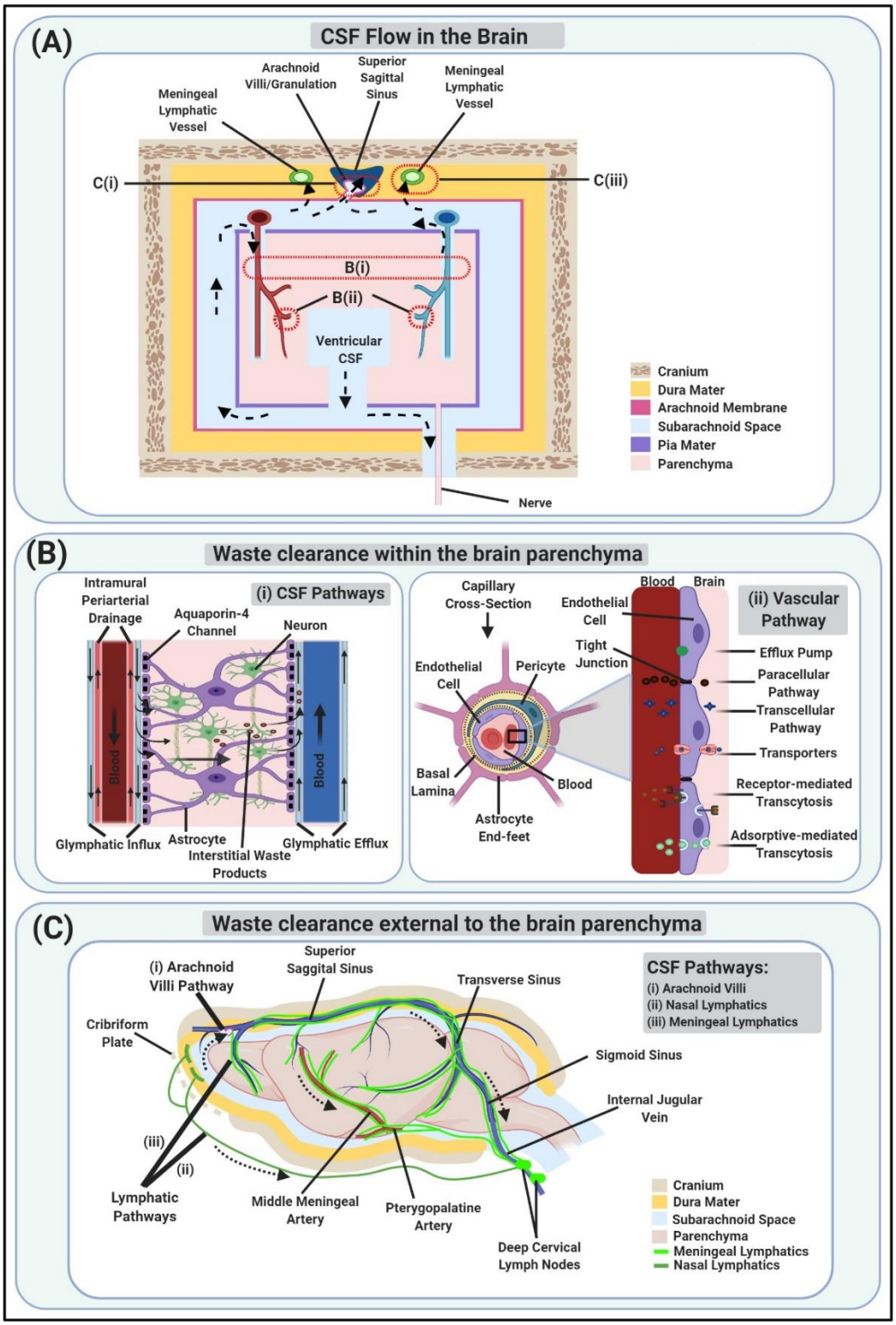
(A)
CSF Flow in the Brain
Arachnoid Villi/Granulation
Superior Sagittal Sinus
Meningeal Lymphatic Vessel
Meningeal Lymphatic Vessel
C(i)
C(iii)
B(i)
B(ii)
Ventricular CSF
Nerve
Cranium
Dura Mater
Arachnoid Membrane
Subarachnoid Space
Pia Mater
Parenchyma
(B)
Waste clearance within the brain parenchyma
(i) CSF Pathways
Intramural Periarterial Drainage
Aquaporin-4 Channel
Neuron
Blood
Blood
Glymphatic Influx
Astrocyte
Interstitial Waste Products
Glymphatic Efflux
Capillary Cross-Section
Endothelial Cell
Pericyte
Basal Lamina
Blood
Astrocyte End-feet
Blood
Brain
(ii) Vascular Pathway
Endothelial Cell
Tight Junction
Efflux Pump
Paracellular Pathway
Transcellular Pathway
Transporters
Receptor-mediated Transcytosis
Adsorptive-mediated Transcytosis
(C)
Waste clearance external to the brain parenchyma
(i) Arachnoid Villi Pathway
Superior Saggital Sinus
Transverse Sinus
Cribriform Plate
Sigmoid Sinus
Internal Jugular Vein
(iii)
(ii)
Lymphatic Pathways
Middle Meningeal Artery
Pterygopalatine Artery
Deep Cervical Lymph Nodes
CSF Pathways:
(i) Arachnoid Villi
(ii) Nasal Lymphatics
(iii) Meningeal Lymphatics
Cranium
Dura Mater
Subarachnoid Space
Parenchyma
Meningeal Lymphatics
Nasal Lymphatics

Figure 2.1- Schematic illustration of Cerebral Waste Clearance (CWC). (A) Schematic model of cerebrospinal fluid (CSF) flow, which is involved in CWC, both within **(B)** and external to the brain parenchyma **(C)**. Dotted arrows show the movement of CSF from the ventricular compartments to the subarachnoid space, entering the brain parenchyma via periarterial spaces, getting mixed with interstitial waste products as well as interstitial fluid (ISF), entering the perivenous space, and then draining via perineural spaces and lymphatics. The waste products also reach the vascular compartments directly via the blood-brain barrier (BBB) and indirectly via CSF exiting through the arachnoid villi/granulations. **B(i)** A magnified schematic image of the glymphatic system, and intramural periarterial drainage (IPAD) pathways involved in CWC within the brain parenchyma. **B(ii)** A magnified schematic image of the vascular pathway via the BBB at the capillary level. **(C)** A schematic image of the CSF pathways involved in CWC via the arachnoid villi **C(i)** and, lymphatic pathways (including the nasal lymphatics **C(ii)** and, the meningeal lymphatics **C(iii)**). This figure is reproduced from [177] licensed under the terms of the Creative Commons Attribution License.

CHAPTER THREE

THE ASSOCIATION BETWEEN GLYMPHATIC SYSTEM AND PERIVASCULAR MACROPHAGES IN BRAIN WASTE CLEARANCE

3.1 Introduction

The glymphatic system is a newly discovered waste clearance pathway in the brain [11, 17, 18, 54, 80-83] and is facilitated by aquaporin-4 (AQP4) protein water channels to promote the convective bulk flow of CSF in the interstitial spaces between the periarterial and perivenous routes [17, 84]. Cerebral arterial pulsations are thought to provide hydrostatic pressure, which also contribute to CSF convective bulk flow and promote CSF-ISF exchange in the glymphatic system [19, 85]. Vasomotions are also considered a driving force for glymphatic CSF flow [178]. Additionally, parenchymal border macrophages (PBMs) (including the perivascular macrophages (PVMs) and leptomeningeal macrophages) regulate the CSF flow via extracellular matrix (ECM) remodeling, which influences arterial stiffness and pulsations [179]. Also, the dynamic changes in arterial diameter due to functional hyperemia/neurovascular coupling and arterial vasomotions accelerate the glymphatic CSF influx and clearance [180].

Similar to the glymphatic hypothesis, some experiments in the past demonstrated the convective bulk flow of solutes, but it was limited to the perivascular spaces rather than the whole interstitial space [115, 181-184]. The convective bulk flow of tracers was also observed along the white matter fiber tracts [38, 51, 114-116]. More recent research [27] and modeling techniques demonstrate a size-dependent diffusive transport of solutes throughout the brain parenchyma instead of convective bulk flow [24, 185]. Similarly,

multiple previous investigations using various molecular-weight tracers have established that diffusion gradients drive solute transport from the brain parenchyma to nearby CSF spaces [186-192]. However, it is questionable if the convective bulk flow is limited to the perivascular spaces or occurs within the brain interstitial space alongside diffusion.

The glymphatic system utilizes the perivascular spaces for CSF-ISF exchange and clearance of interstitial waste solutes from the brain parenchyma. PVMs are a specific subpopulation of myeloid cells which are located in the perivascular spaces between the vascular basement membrane and glial limitations of blood vessels. They are constantly in direct contact with the CSF and play a significant role in brain homeostasis [193-198]. PVMs were long thought to be produced from bone marrow precursor cells that enter the brain via the bloodstream and are continually replaced by blood monocytes [199]. Recent research, however, indicates that PVMs are formed early during development by embryonic precursors derived from the yolk sac and are not replaced by blood monocytes [198, 200]. It is important to keep in mind that, despite substantial studies on the glymphatic system, the investigation of PVMs in mediating the glymphatic system is just emerging.

Both the glymphatic system and the PVMs play important functions in a variety of neurological conditions. The dysfunction of the glymphatic system has been associated with numerous neurological conditions such as Alzheimer's disease (AD) [5, 6, 101], traumatic brain injury (TBI) [10-12, 22, 102-104], microinfarcts [110, 111], small vessel disease (SVD) [105, 106], migraine [112], stroke [107-109], diabetes [20], and glaucoma [113]. Moreover, aging [93, 201], sleep [22, 81], anesthesia [96], body posture [90], etc. influence the glymphatic system function. PVMs are scavenger/immune cells that help

preserve blood-brain barrier (BBB) integrity [202], participate in macromolecule/pathogens/cellular debris uptake (phagocytosis) [203-206], and antigen presentation to lymphocytes [199, 207, 208]. They constitute a vital component of the brain's immune system [193, 209-211] and play a role in a range of neurological conditions such as AD [212-214], ischemic stroke [215, 216], multiple sclerosis [217-219], brain infections [220-224], hypertension [225, 226], etc. Recent promising research has demonstrated the critical function of PVMs in AD and aging; PVMs depletion in mice leads to a considerable buildup of amyloid-beta (Aβ) plaque (an AD-related protein); in aged-mice macrophage colony-stimulating factor (M-CSF) treatment significantly increases Matrix metalloproteinase (MMP) activity and reduces the deposition of extracellular matrix (ECM) protein [179].

Utilizing in-vivo T1WI with Gd-albumin contrast, DTI, and confocal microscopy imaging, the purposes of this study are to determine 1) if diffusion is sufficient to account for the intra-striatally administered tracer dynamics within the brain interstitial spaces, particularly, the striatum, and the corpus callosum of the rat brain, 2) the role of the glymphatic system in intra-parenchymal tracer transport, 3) tracer uptake by PVMs along both the arteries and veins, and4) the association between the glymphatic system and the PVMs.

3.2 Materials and Methods

3.2.1 Animals and Surgical Procedures

All experimental procedures were conducted and performed in accordance with guidelines of the National Institutes of Health (NIH) for animal research under a protocol approved by the Institutional Animal Care and Use Committee of Henry Ford Hospital,

and experimental guidelines of Animal Research: Reporting of In Vivo Experiments (ARRIVE) (items 8, 10 to 13).

3.2.1.1 Rats

Wistar Rats (3 months, male, Charles River, Wilmington, MA, USA) were subjected to MRI measurements and ex-vivo fluorescent tracer distribution study using confocal microscopy after intra-striatal tracer infusion (n=10) and intra-cisternal tracer infusion (n=4).

3.2.1.2 Intra-striatal surgical procedure

Anesthesia was induced with 3.0% Isoflurane in a gas mixture of N_2O (70%) and O_2 (30%) and maintained with 1.0% - 1.5% Isoflurane throughout the procedure. For intra-striatal fluorescent tracer (FITC-Dextran, 70 kD) and MRI contrast agent (Gd-albumin, 70 kD) infusion, anesthetized rats were placed in a stereotaxic frame (Stoelting Co., Wood Dale, IL, USA) and the skin was opened to expose the skull. A small burr hole was made over the right parietal cortex with a hand-held drill (Foredom Electric Co., Bethel, CT, USA). A 27-gauge needle was introduced into the right striatum at the following coordinates based on the rat brain atlas [227]: anterior-posterior (AP) = 0 mm; midline (ML) = 3.5 mm; vertical depth (VD) = 5 mm from bregma. FITC-Dextran (3µl constituted in artificial CSF at a concentration of 1%) and MRI contrast agent, Gd-albumin (3µl) were loaded together into a PE-10 catheter (Becton Dickinson, Cockeysville, MD, USA) and part of the catheter was introduced through the needle track into the striatum. The skull burr hole was then sealed with bone wax. Rats were taken to the 7 Tesla (T) magnet for MR imaging immediately after the surgical procedure. The remaining part of the indwelling catheter was connected to another PE-10 catheter filled

with saline and attached to a glass Hamilton syringe as an extension out of the MRI machine.

3.2.1.3 Intra-cisternal surgical procedure and tracer infusion

Anesthetized rats were placed in a stereotaxic frame (Stoelting Co.) and the atlanto-occipital regions covering the cisterna magna were exposed by tilting the head downward at ~ 90° angle. The occipital bone was exposed via a midline incision. A small burr hole was made over the occipital bone 1 mm above the cisterna magna and 1mm lateral to the midline. The dura mater was carefully exposed and punctured with a 27-gauge needle. A polyethylene catheter (PE-10 tubing; Becton Dickinson, Cockeysville, MD, USA) filled with 30 µl of fluorescent tracer (FITC-dextran, 70 kD) was introduced into the cisterna magna through the puncture to a depth of 1-2 mm with its tip positioned at the midline of cisterna magna. The indwelling catheter was secured, and the perforation site was sealed with surgical glue. The skin incision was then stitched. Using the indwelling catheter connected to a Hamilton syringe, FITC-dextran was administered at a rate of 1 µl/min for 30 minutes using an infusion pump (Harvard Apparatus, Holliston, MA, USA). To avoid possible backflow, the indwelling catheter and Hamilton syringe were left in place after infusion. Rats were sacrificed 2 hours after infusion to study the dynamics of FITC-dextran in the coronal brain sections using confocal microscopy imaging.

3.2.2 MRI measurements

A 7 Tesla MRI system (Bruker-Biospin, Billerica, MA, USA) was employed to perform MRI measurements. The receiver was a quadrature 2×2 surface array coil, while the transmitter was a body volume birdcage-type coil. Rats were safely placed on an MR-

compatible holder equipped with stereotaxic ear bars to control head motions and an adjustable nose cone for anesthetic gas distribution. At the start of the MRI scan, the holder was inserted into the magnet and placed in the middle. Isoflurane (1.0-1.5%) and a gas mixture of N_2O (70%) and O_2 (30%) was utilized as anesthesia during the MRI measurements, and respiration (50-65 breaths/minute) was carefully observed throughout the MRI scanning (Biopac Systems Inc., Goleta, CA, USA). The rectal temperatures of the rats were maintained at 36°C with an air heating blower (Rapid Electric, Brewster, NY, US).

To measure the dynamics of the Gd-albumin after intra-striatal infusion, 3D T1WI (TE = 4 ms, TR = 18 ms, flip angle = 12º, FOV = 32×32×16 mm^3, matrix = 256×192×96 (resolution of 0.125×0.167×0.167 mm) later interpolated to 256×256×96 voxels (resolution of 0.125×0.125×0.167 mm)) were acquired using a spin-echo sequence. Two baseline scans using 3D T1WI sequences were employed prior to infusion, followed by intra-striatal administration of Gd-albumin + FITC-dextran (6 µl, 70 kD) at an infusion rate of 0.3 µl/min for 20 min using the indwelling catheter connected to a 100 µl glass syringe (Hamilton Robotics, Reno, NV, USA) mounted on an infusion pump (Harvard Apparatus, Holliston, MA, USA). After the end of an infusion, three 3D T1WI sequences were employed to track the movement of Gd-albumin. Diffusion-weighted (DW) spin-echo sequence to estimate ADC of water molecules was also employed after the end of intra-striatal infusion with parameters TE = 40 ms, TR = 1500 ms, b-value = 900 s/mm^2, directions = 6, slice thickness = 0.8 mm, number of slices = 15, FOV = 32×32 mm^2, matrix = 128×128. To avoid possible backflow, the Hamilton syringe was left in place

after infusion. At the end of the experiment, animals were immediately taken for sacrifice, and tissues were prepared for ex-vivo confocal microscopy imaging.

3.2.3 Histology

3.2.3.1 Tissue preparation for vibratome sections and immunohistochemistry

Rats were transcardially perfused with saline, followed by 4% paraformaldehyde. The brains were immersed in 4% paraformaldehyde at 4°C for 48h. Coronal vibratome sections (100 μm, AP = 0.20 to -0.4 mm from bregma) for rats with intra-striatal infusion and intra-cisternal infusion were processed for single immunofluorescence labeling for CD206 and alpha-smooth muscle actin (αSMA). Briefly, vibratome coronal brain sections were incubated with the primary antibody including CD206 (PVMs marker, Abcam, AB64693, 1:2,000) or αSMA (smooth muscle cells marker, DAKO, M0851, 1:400) for 4 days at 4°C, and then with the secondary antibody conjugated to Cy3.

3.2.3.2 Ex-vivo confocal microscopy imaging

Coronal brain sections were assessed using an Olympus FLUOVIEW FV1200 Biological Confocal Laser Scanning Microscope (Olympus America Inc., Center Valley, PA). The FV10-ASW software was used to operate the motorized stage, focus, and XYZ image acquisition. The distribution of FITC-dextran was imaged with FITC (green) emission channel and CD206 or αSMA staining samples were imaged using cy3 (red) emission channel. We used Olympus UPlanSApo 10x/0.40 and 40x/0.95 objectives and laser lines at the excitation wavelength of 473 nm and emission wavelength of 519 nm for FITC-dextran, excitation wavelength of 559 nm and emission wavelength of 567 nm for αSMA and CD206. Image scale bars were applied using ImageJ while keeping the image integrity intact.

3.2.4 Data Analysis

3.2.4.1 Pseudo-ADC (ADC*) calculation from T1WI

To estimate the diffusion parameter from the contrast-enhanced T1WI, we tracked the distribution of the Gd-albumin over time. We analyzed three T1WI volumes that were scanned about 4.5, 24, and 28.5 minutes after the end of the tracer infusion. For each volume, a rough segmentation covering the hyperintensity regions caused by the tracer near the infusion site and along the corpus callosum was drawn manually using MRIcro software. The ROIs were then processed in MATLAB to identify the regional boundaries more precisely. To do this, the tissue inside the manually segmented ROIs was further segmented into two regions using Otsu's threshold approach [228]. The region with higher intensities includes the tissue with tracer. The boundaries (surface) of the regions were identified, as shown in **Fig- 3.1A**. For each T1 volume, a set of voxels, *P(x,y,z)*, on the surface of the distributing tracers was calculated, $S_1=\{P_i^1|i=1,\ldots, N_1\}$, $S_2=\{P_i^2|i=1,\ldots, N_2\}$, $S_3=\{P_i^3|i=1,\ldots, N_3\}$. Here, *N* is the number of voxels on each surface and since the regions were growing as the tracer distributed to the tissues, it is reasonable to assume $N_1< N_2< N_3$. Next, the distance traveled by the tracer from each point on a surface to the closest point on the next surface was calculated. Knowing the dimensionality, *d* as 3, distance, *Dist*, and the traveled time, *t*, by the tracer, the pseudo apparent diffusion coefficient can be estimated as:

$$ADC^* = \frac{Dist^2}{2dt} \tag{3.1}$$

The estimated diffusion values over the surface points were averaged to achieve an approximate measure of the ADC* of Gd-albumin in the striatum and along the corpus callosum.

3.2.4.2 ADC estimation from DTI

The DW MRI data were processed and analyzed using in-house codes in MATLAB (The MathWorks, Inc., Natick, MA, USA). First, the DW volumes were motion corrected by a coarse registration using SPM8. Then, similar to the method used by [229], the DTI tensor was estimated from the DW images. Then, DTI scalar maps such as fractional anisotropy (FA), apparent diffusion coefficient (ADC), axial (parallel) diffusion coefficient (D_{axi}), and radial (perpendicular) diffusion coefficient (D_{rad}) were calculated as follows:

$$FA = \sqrt{\frac{1}{2} \times \frac{(\lambda_1 - \lambda_2)^2 + (\lambda_1 - \lambda_3)^2 + (\lambda_2 - \lambda_3)^2}{\lambda_1^2 + \lambda_2^2 + \lambda_3^2}} \tag{3.2}$$

$$ADC = \frac{\lambda_1 + \lambda_2 + \lambda_3}{3} \tag{3.3}$$

$$D_{axi} = \lambda_1 \tag{3.4}$$

$$D_{rad} = \frac{\lambda_2 + \lambda_3}{2} \tag{3.5}$$

in which $\lambda_1 > \lambda_2 > \lambda_3$ are the sorted eigenvalues of the diffusion tensor in each voxel. FA is a measure of restricted diffusion, and it is high in white matter fiber bundles. We used ADC and FA maps to manually segment the infusion site and corpus callosum, respectively, as shown in **Fig- 3.1B**.

Based on the structure of extracellular spaces, the macroscopic diffusion in the brain tissues is hindered and defined by ADC. ADC is related to the free diffusion coefficient by a restriction parameter called tortuosity, λ.

$$\lambda^2 = \frac{D}{D_{ADC}} \tag{3.6}$$

Our ADC maps provided the ADC values for water molecules. Using the reported free diffusion coefficient of water (18 D) as 3×10^{-6} mm^2/ms [230] and eqn-3.6, we first calculated tortuosity for water molecules in the striatum and along the corpus callosum. Then, assuming the tortuosity for Gd-albumin to be the same as water molecules and using the reported value 8.29×10^{-8} mm^2/ms [188] for the free diffusion coefficient of bovine serum albumin (66 kD) as a substitute for Gd-albumin (70 kD) and eqn-3.6 again, we finally estimated the ADC for Gd-albumin in the striatum and along the corpus callosum.

The assumption of using the tortuosity for Gd-albumin to be the same as water molecules despite a huge difference in their molecular weight is reasonable because the ADC in eqn-3.6 is inversely proportional to tortuosity squared. Using true (bigger) tortuosity values for Gd-albumin would give an even smaller ADC value estimated from DTI, which would even support more in favor of our results that convective bulk flow is present in addition to diffusion in the brain.

3.2.5 Data quantification and statistical analysis

To evaluate the convective bulk flow in the interstitial spaces of the brain parenchyma, ROIs were generated near the intra-striatal infusion site and the corpus callosum. ADC* of Gd-albumin was calculated from T1WIs using the dynamics of

contrast agent within those ROIs. Similarly, ROIs were used to estimate the ADC of Gd-albumin from DTI-generated ADC maps. Results of calculated ADC* (from T1WIs) and estimated ADC (from DTI) using both ROIs are shown as mean ± standard error in bar plots as shown in **Fig- 3.1C, D**. A two-sample t-test was performed between two groups with a $p < 0.05$ statistical significance level in order to determine the convective bulk flow within the brain parenchyma.

3.3 Results

3.3.1 Convective bulk flow in the interstitial spaces of the brain parenchyma

Gd-albumin (70 kD) was employed as a high molecular weight (MW) tracer to determine the size-independent convective bulk flow transport within the brain parenchyma. Due to the very small size of perivascular spaces, convective bulk flow cannot be directly evaluated using MRI, so we indirectly calculated ADC* values of Gd-albumin from T1WI. To estimate the diffusion parameter from the contrast-enhanced T1WI, we analyzed the distribution of the Gd-albumin over time. ADC* values of Gd-albumin were calculated from the in-vivo T1WIs. **Fig- 3.1A** shows the ROIs enclosing the boundary of Gd-albumin movement near the intra-striatal infusion site and along the corpus callosum 4.5, 24, and 28.5 minutes after the end of infusion, respectively. As seen in these images, the boundaries kept on expanding, indicating the movement of Gd-albumin with time. ADC* values calculated from T1WIs using the dynamics of the contrast agent were affected by both the convective bulk flow and diffusion.

ADC of Gd-albumin was estimated from DTI. The ADC and FA maps derived from DTI and the ROIs near the infusion site and corpus callosum are shown in **Fig-3.1B**. The FA maps were used to draw the ROIs near the infusion site and the corpus

callosum, since these maps can show the restricted diffusion clearly, especially along the corpus callosum.

Fig- 3.1C, D show the quantitative comparison of the calculated ADC* (from T1WIs) and estimated ADC (from DTI) values (Mean ± SE) and demonstrates the significantly higher value of calculated ADC* (**Fig- 3.1C**, $(3.64 \pm 0.8) \times 10^{-8}$ vs $(1.75 \pm 0.1) \times 10^{-8}$, $p = 0.038$, % difference- 70) in the striatum and higher value of calculated ADC* (**Fig- 3.1D**, $(2.67 \pm 0.7) \times 10^{-8}$ vs $(1.97 \pm 0.08) \times 10^{-8}$, $p = 0.34$, % difference- 30) along the corpus callosum compared to the estimated value of ADC from DTI. Our data demonstrates that calculated ADC* values from T1WIs are higher than estimated ADC values from DTI, indicating that tracer movement within the brain parenchyma, particularly in the striatum and the corpus callosum, is supported not only by diffusion but also involves bulk flow independent of molecular weight of solutes.

3.3.2 Glymphatic system-mediated transport within the brain parenchyma

The tracer movement in the rat brain was examined using confocal microscopy imaging on coronal brain sections after intra-striatal and intra-cisternal administration of FITC-dextran, separately. The tracer movement in the striatum and the corpus callosum was detected 50 minutes after intra-striatal infusion of high MW FITC-dextran (70 kD), as shown in **Fig- 3.2A**. The tracer was observed in the perivascular spaces near the infusion site **(Fig- 3.2(A2-A4))**, distal from the infusion site (**Fig- 3.2(A1, A5))**, and in the perivascular spaces of the contralateral hemisphere of the brain **(Fig- 3.2(A6))**. Using an αSMA as a marker to determine arterial vessels, we found that the tracer entered both the periarterial and perivenous spaces as shown in **Fig- 3.4A-I.** These images demonstrate that 50 minutes after intra-striatal infusion, the tracer not only moved far

from the infusion site but also entered the perivascular spaces of both the veins and the arteries, indicating the important role of the glymphatic system and convective bulk flow in the propagation of tracer/interstitial waste solutes within the brain parenchyma. To minimize the effect of intra-striatal injection on the glymphatic system [84], we investigated the tracer distribution via the glymphatic system following intra-cisternal administration of FITC-dextran. The tracer was seen in both the hemispheres **(Fig- 3.6)** and was present mostly in the cortical periarterial and perivenous spaces 2 hours post intra-cisternal infusion, demonstrating the functioning of the glymphatic system and convective bulk flow in CSF tracer transport, as was previously reported in glymphatic system studies [17, 80].

3.3.3 PVMs and their association with the glymphatic system

PVMs are a distinct population of resident brain macrophages localized in close proximity to cerebral blood vessels and express the mannose receptor CD206. We hypothesized that PVMs, due to their specific location in the CSF-filled perivascular spaces, may play an important role in interstitial waster clearance. Using confocal imaging analysis, we found that after intra-striatal infusion of FITC-dextran, the tracer was accumulated in cells located within the perivascular spaces of the vasculature **(Fig-3.2)**. Three-dimensional (3D) XZ and YZ cross-sectional confocal imaging showed that these cells were present outside the vascular lumen, **(Fig- 3.5A)**. **Fig- 3.3A-F** are the confocal images further showing the tracer uptake predominantly by cells within the perivascular spaces surrounding the medium to large-sized vessels (25-50 μm in diameter) and the co-localization of CD206 immunoreactive cells, a specific marker for PVMs, indicating that the tracer is primarily taken up by PVMs. The co-localization of

the tracer and CD206-positive PVMs using 3D cross-sections of XZ (bottom) and YZ (right) planes obtained from z-stacked confocal microscopy images is shown in **Fig-3.5B**. Interestingly, after the intra-striatal infusion of FITC-dextran in the right hemisphere, the tracer was accumulated in PVMs on the contralateral hemisphere of the brain as well **(Fig- 3.2(A6))**. This tracer accumulation by brain-wide PVMs suggests that PVMs play an essential role in sampling the components of the CSF and the removal of interstitial waste solutes from the brain.

Next, we performed intra-striatal tracer infusion, to determine if tracer accumulated PVMs were located in the perivascular spaces of both the arterioles and venules in which αSMA-immuno positive and negative vessels were used to determine arterioles and venules, respectively. We detected that CD206 positive PVMs localized to the perivascular spaces of αSMA^{+} arterioles and αSMA^{-} venules (**Fig- 3.4A-I**). This result suggests that the PVMs filter CSF components during the glymphatic influx along arteries and glymphatic efflux along veins. We also detected the tracer accumulated PVMs specifically in the pial-glial periarterial spaces of the glymphatic system instead of the periarterial spaces along the basement membranes between smooth muscle cells (SMCs) in the walls of the arteries for intramural periarterial drainage pathway (IPAD) **(Fig- 3.5C)**. **Fig- 3.5C** shows the 3D cross-sections of XZ (bottom) and YZ (right) planes clearly exhibiting the PVMs external to the SMCs in arterioles. This evidence is critical in confirming that the PVMs and the glymphatic system share the same perivascular spaces and work hand-in-hand for the removal of interstitial waste solutes from within the brain parenchyma.

Again, to minimize the effect of intra-striatal injection on the glymphatic system [84], we repeated the experiments using the intra-cisternal infusion of FITC-dextran and further analyzed the tracer uptake by PVMs and their association with the glymphatic system. **Fig- 3.6A** is the coronal brain section image showing tracer transport by the glymphatic system. Again, the tracer and tracer accumulated cells were prevalent in the perivascular spaces of both the cerebral hemispheres (**Fig- 3.6 (A1-A6))**. To further confirm the tracer accumulated cells to be PVMs, we used CD206 staining. **Fig- 3.7A-F** show the cells present in perivascular spaces and confirm them to be $CD206^+$ PVMs. αSMA staining was then conducted to establish that PVMs in both peri-arterioles and peri-venules had taken up the tracer. **Fig- 3.8A-I** show the tracer and tracer accumulated PVMs in perivascular spaces of the vasculature and distinguished the αSMA^+ arterioles from αSMA^- veins. Collectively, confocal microscopy images after the intra-striatal and intra-cisternal infusions of tracers, separately, in the rat brain indicate the crucial function of PVMs in the uptake of tracer/interstitial waste solutes during glymphatic CSF influx (along arteries) and efflux (along veins).

3.4 Discussion

The glymphatic system proposes a brain-wide waste clearance through a specialized network of perivascular spaces and convective bulk flow of CSF, ISF, and interstitial waste solutes through the interstitial spaces of the brain parenchyma. However, the glymphatic system hypothesis of convective bulk flow in the interstitial spaces is not widely accepted and many studies argue in favor of diffusion as a microscopic mechanism of waste transport in the brain interstitial spaces [24, 27, 185]. Moreover, the association of the PVMs (a specific type of immune cells present in the

perivascular spaces) with the glymphatic system for interstitial waste clearance has not been thoroughly investigated.

In this study, to evaluate the transport mechanism in the striatum, we utilized a high-molecular-weight tracer (Gd-albumin, 70 kD) that is ideally suited to analyze the size-independent convective bulk flow. The ADC* value calculated from T1WI accounted for the transport of the contrast agent via both convective bulk flow and diffusion processes. The ADC value estimated from DTI solely accounted for the diffusion of the contrast agent. In the striatum, the ADC* calculated from T1WI was 70% larger than the ADC estimated from DTI as shown in the bar plots of **Fig- 3.1C**. In the corpus callosum, the ADC* calculated from T1WI was 30% larger than the ADC estimated from DTI as shown in the bar plots of **Fig- 3.1D**. These results demonstrate the presence of both the convective bulk flow and diffusion in the interstitial spaces of the brain, consistent with the initially proposed glymphatic system [17]. These findings are also consistent with a recent study that used a model based on the Lagrangian approach for optimal mass transport and found that convective bulk flow is the predominant mode of transport in perivascular spaces, while both convective bulk flow and diffusion are significant modes of transport within the brain parenchyma [231]. Using a mathematical model, different research [232] verified the existence of convective bulk flow and diffusion in the cortex of the human brain. However, both studies utilized small MW tracers, such as Gd-DOTA (MW-557.6 D) and Gadobutrol (MW-604 D), respectively, to establish their findings, which are not suited for studying the convective bulk flow in the brain tissue. Therefore, we attempted to address this controversy by employing Gd-albumin (70 kD), a high MW tracer that is suitable for this purpose.

In this study, the DTI-estimated ADC values in the corpus callosum **(Fig- 3.1D)** are bigger than ADC values in the striatum **(Fig- 3.1C)**, which is expected given that the corpus callosum is composed of white matter containing millions of myelinated axons, and diffusion of solutes is faster along the direction of the fiber tracts. On the other hand, the T1WI-calculated ADC* values in the corpus callosum **(Fig- 3.1D)**, are lower than the ADC* values in the striatum **(Fig- 3.1C)**, which may be attributed to the larger bulk flow near the intra-striatal infusion site due to its proximity to the needle track and the presence of more vasculature and perivascular spaces in the striatum compared to the corpus callosum.

In order to assess the role of the glymphatic system and convective bulk flow, we also employed ex-vivo confocal microscopy imaging and determined if the intra-striatal infused tracer (FITC-dextran, 70 kD) could be detected along the perivascular spaces of arteries/arterioles and veins/venules distant from the infusion site. Our findings revealed the presence of the tracer in the perivascular spaces and brain tissue distant from the intra-striatal infusion site **(Fig- 3.2)** indicating the role of convective bulk flow in tracer transport within the brain parenchyma. The presence of tracer in the periarterial and perivenous spaces, demonstrating the functioning of the glymphatic system following intra-striatal infusion, was verified using αSMA labeling to differentiate between arterioles and venules **(Fig- 3.4)**. Although after intra-striatal infusion, we did not expect the tracer to enter the periarterial spaces, but this may be due to the re-circulation of the tracer via the glymphatic system after draining through the perivenous spaces into the CSF compartments (subarachnoid space or ventricles) [17]. Another plausible reason for the tracer being present in the periarterial spaces is through the glymphatic system after a

little amount of tracer leakage into the subarachnoid space via the needle track during the infusion. The function of the glymphatic system was also verified after the intra-cisternal infusion of the tracer; the presence of the tracer in both hemispheres of the brain **(Fig-3.6)** and in the peri-arteriole and peri-venule spaces **(Fig- 3.8)** indicate the tracer transport by the glymphatic system.

The findings of this study using confocal microscopy imaging on coronal brain sections revealed the presence of PVMs in the perivascular spaces of arterioles external to the SMCs, the same pathway used by CSF during the glymphatic system influx. The $LYVE1^{+}/CD163^{+}$ (scavenger receptor cells) PVMs located external to the vascular SMCs along arteries and separated by basal lamina have been recently demonstrated using electron microscopy [179]. After the intra-striatal **(Fig- 3.2-3.4)** and intra-cisternal **(Fig-3.6-3.8)** infusions, independently, we further showed the tracer uptake by the PVMs located in the perivascular spaces of both the arterioles and venules. These findings indicate that PVMs interact with CSF during both glymphatic influx (along arteries) and glymphatic efflux (along veins). In fact, PVMs not only interact with CSF but also filter its components to eliminate potentially toxic interstitial waste solutes and other foreign solutes/pathogens. This result is consistent with a recently published study in mice showing that PVMs examine CSF contents as CSF moves into and out of the brain (following intra-cisternal and intra-striatal injections, respectively) and that PVM deletion inhibits CSF influx and efflux [179]. They also observed double positive PVMs after co-injecting the tracers intra-striatally and intra-cisternally, which support the findings of our study. Following the impairment of CSF flow dynamics in PVM-depleted mice, further analysis of the CSF protein content revealed an accumulation of synapse-related proteins

(such as NRXN1, CDH2, and NRCAM, etc.) and AD-related proteins (such as clusterin, apolipoprotein, and amyloid precursor protein, etc.). Furthermore, they found $LYVE1^+$ (scavenger receptor cells) PVMs along αSMA^+ arteries/arterioles and $MHCll^+$ (antigen-presenting cells) PVMs along αSMA^- veins/venules, showing the distinct functions of PVMs identified in perivascular spaces of arteries and veins. They also found increased fibroblast activity, decreased MMP activity, impaired arterial vasodilatory responses, and an accumulation of extracellular matrix (ECM) proteins (such as laminin, collagen IV, etc.) along αSMA^+ vessels in PVM-depleted mice, indicating that $LYVE1^+$ $MHCII^{lo/neg}$ PVMs regulate the CSF flow dynamics through their capacity to regulate ECM remodeling, which in turn affects the arterial stiffness and pulsation [179]. A very recent study has shown that dynamic variations in vascular diameter/vasomotion due to neurovascular coupling encourage CSF to flow through the perivascular spaces, hence driving perivascular glymphatic CSF influx and clearance [180]. Collectively, these findings imply that PVMs not only interact with CSF during glymphatic influx and efflux, but also regulate CSF flow dynamics by modulating arterial stiffness/pulsations, which is the key contributor to CSF-ISF exchange in the glymphatic system. As a result, the PVMs are closely related to the glymphatic system, and the two systems collaborate to clear toxic interstitial waste solutes from the brain and maintain homeostasis.

Furthermore, PVMs have been demonstrated to be the critical players in regulating the CSF flow dynamics in aging and AD [179]. Also, with aging, the functioning of the glymphatic system decreases [93, 201], probably due to a decrease in vascular elasticity and neurovascular coupling [180, 233, 234]. The glymphatic system

and PVMs should be further investigated as potential novel treatment targets for patients with AD and age-related disorders.

A drawback of this work is that the intra-striatal infusion is traumatic, severely suppresses the functioning of the glymphatic system, and disturbs fine pressure gradients [84] . However, to minimize these effects, we carefully introduced a PE-10 catheter into the striatum to examine the convective bulk flow within the brain parenchyma. Additionally, during the intra-striatal infusion in MRI scans, a tiny amount of tracer may have leaked into the subarachnoid space via the needle track and re-entered the brain parenchyma via the glymphatic pathways which is another limitation of this study. However, we employed a low infusion rate of 0.3 μl/min to minimize this kind of tracer leakage. Another drawback of this study is that the evaluation of ADC values of Gd-albumin from T1WIs and DTI could have some flaws. First, we used a regional growing scheme to assess the distance that the Gd-albumin particles traveled between two MRI scans. In this process, the segmentation of tissues containing the tracer is not very precise due to limited contrast to noise ratio (CNR). Second, we had to assume the tortuosity for Gd-albumin to be the same as water molecules. Although this could impose an overestimation bias for the DTI-estimated ADC values, our conclusion that diffusion alone is not sufficient for the tracer movement within the brain parenchyma remains valid, as we discussed in section 3.2.4.2.

3.5 Conclusion

To examine the solute transport mechanism in the brain interstitial spaces, we utilized high MW Gd-albumin for intra-striatal administration. In the striatum and along the corpus callosum, the ADC* calculated from T1WI was 70% and 30% higher,

respectively, than the ADC estimated from DTI, suggesting the existence of both the convective bulk flow and diffusion in the interstitial spaces of the brain. Confocal microscopy imaging revealed tracer in the peri-arteriole and peri-venule spaces, as well as in brain tissue distant from the intra-striatal infusion site, indicating the contribution of the glymphatic system and convective bulk flow to parenchymal tracer transport, which was also confirmed after intra-cisternal tracer infusion. PVMs were observed in the pial-glial perivascular spaces utilized by the glymphatic CSF influx and efflux for interstitial waste clearance. This study additionally showed tracer uptake by PVMs in both the peri-arteriole and peri-venule spaces following intra-striatal and intra-cisternal administration of the tracers, separately. PVMs regulate the CSF flow dynamics, hence indirectly supporting the functioning of the glymphatic system. Collectively, the findings of this study suggest a significant role of PVMs in interstitial waste clearance during glymphatic CSF influx along arteries and glymphatic CSF efflux along veins. A better understanding of the association between these pathways may lead to new therapeutic strategies for numerous neurological conditions.

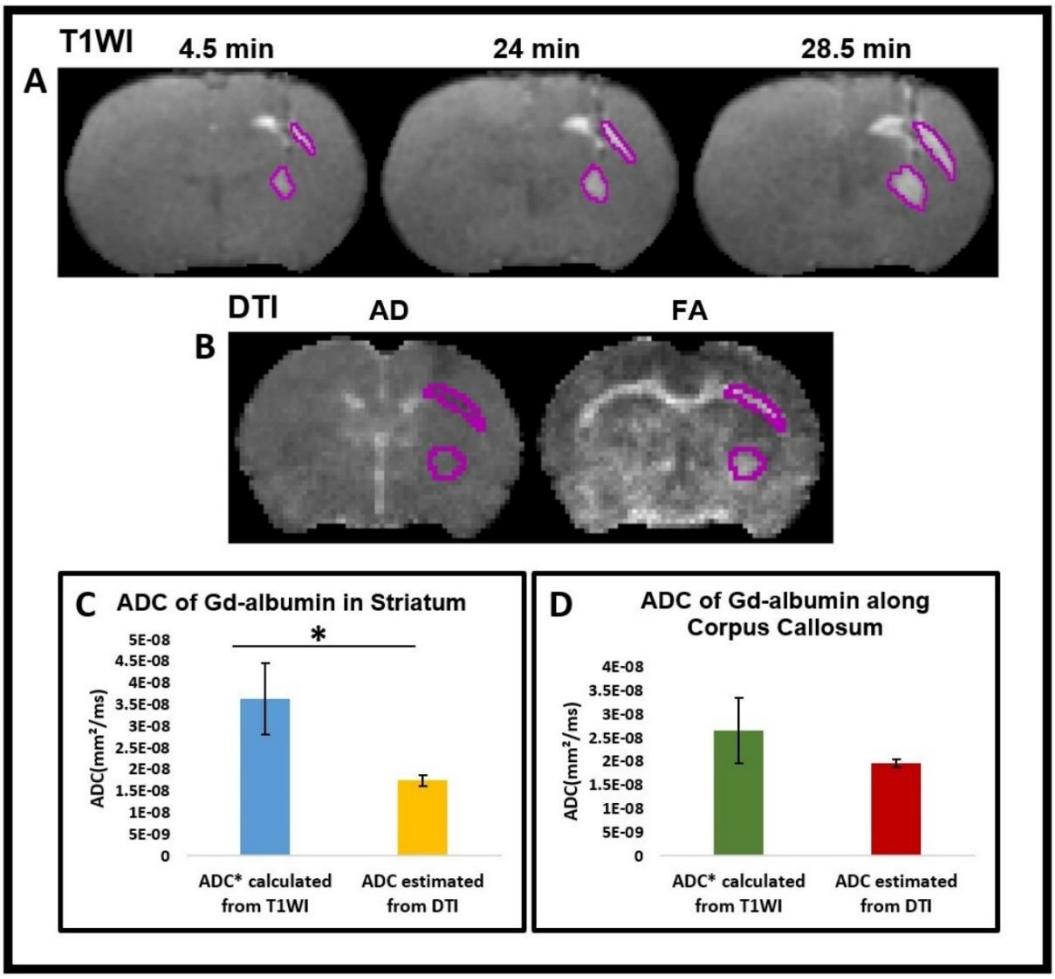

Figure 3.1- (A) T1-weighted images 4.5, 24, and 28.5 minutes after the end of tracer infusion, shown in the coronal view, for illustration. The boundaries of the tracer were calculated using MATLAB from the initial manual segmentation. **(B)** Images of ADC, and FA maps resulted from DTI. **(C, D)** Bar plots showing the average ADC* of Gd-albumin calculated from T1WI and ADC estimated from DTI in the striatum **(C),** and along the corpus callosum **(D)** of rat brain after the intra-striatal administration of Gd-albumin with * $p<0.05$. Error bars indicate the standard errors.

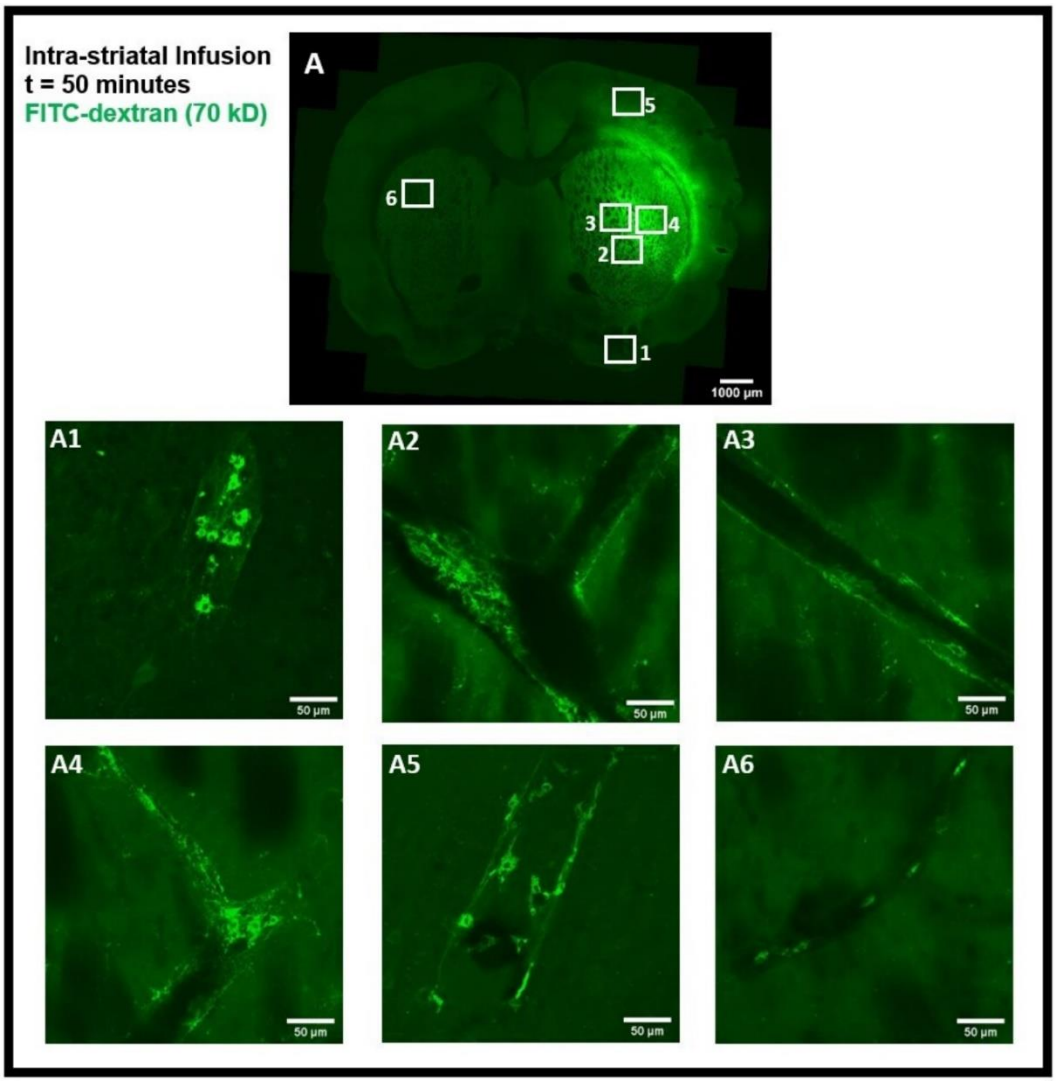

Figure 3.2- Intra-striatal administration of FITC-dextran (70 kD) in the rat brain. **(A)** shows the movement of the tracer in the striatum and the corpus callosum 50 minutes after infusion in coronal brain section. The presence of a tracer (green) in the perivascular spaces near the infusion site **(A2-A4)**, far from the infusion site **(A1, A5)**, and on the contralateral hemisphere **(A6)**, can be seen using confocal microscopy imaging.

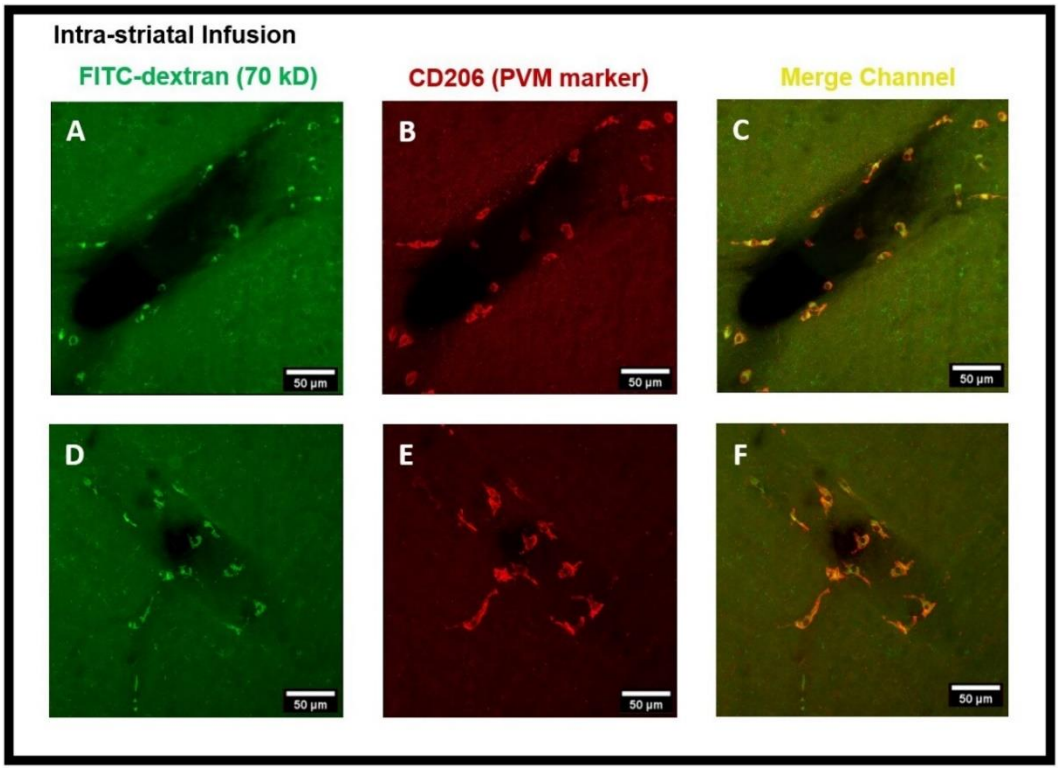

Figure 3.3- FITC-dextran tracer uptake by the perivascular macrophages (PVMs) present in the perivascular spaces after intra-striatal administration. **(A, D)** show the tracer (green) accumulated cells using the FITC channel, **(B, E)** show the CD206 staining (red) which is a specific marker for PVM using the cy3 channel, **(C, F)** are the images from the merged channel showing the co-localization (yellow) of CD206 antibody with tracer accumulated cells, confirming them to be PVM.

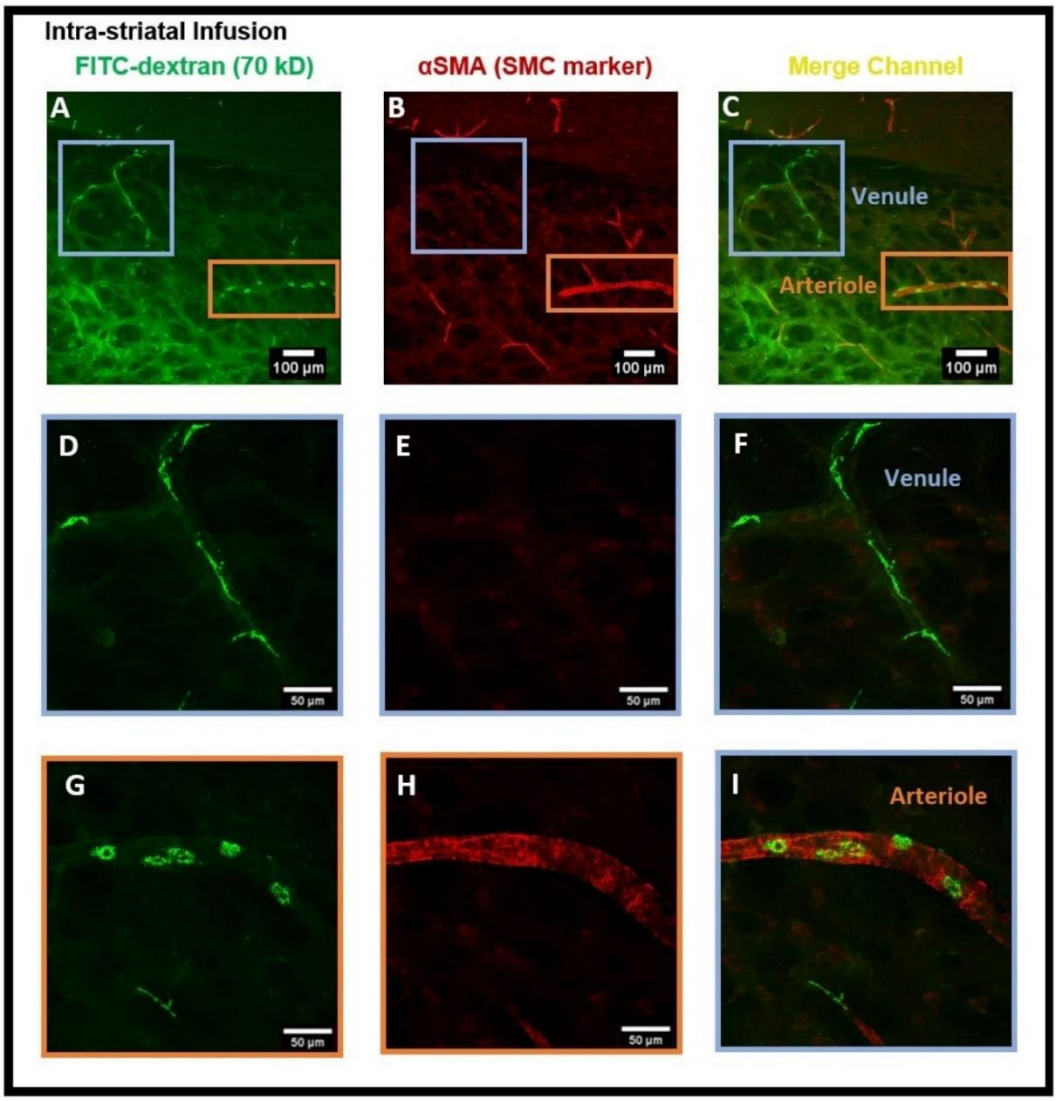

Figure 3.4- Presence of FITC-dextran and PVMs in the peri-arteriole and peri-venule spaces after intra-striatal administration of FITC-dextran. **(A)** shows the tracer and tracer accumulated cells (green) in the perivascular spaces of vasculature, **(B)** shows the αSMA staining (red) specific for smooth muscle cells (SMCs), **(C)** merged channel shows the presence of αSMA for SMC in arteriole and absence of αSMA in venules. **(D, G)** are the sub-images of **(A)** showing the magnified view of vessels, **(E, H)** are the sub-images of **(B)** showing the magnified view of αSMA staining, **(F, I)** are the sub-images of **(C)** showing the magnified view of αSMA^{+} arteriole **(I)** and αSMA^{-} venule **(F)**. **(I, F)** distinguished the arterioles from veins and confirm the presence of tracer accumulated PVM in the peri-venule and peri-arteriole spaces.

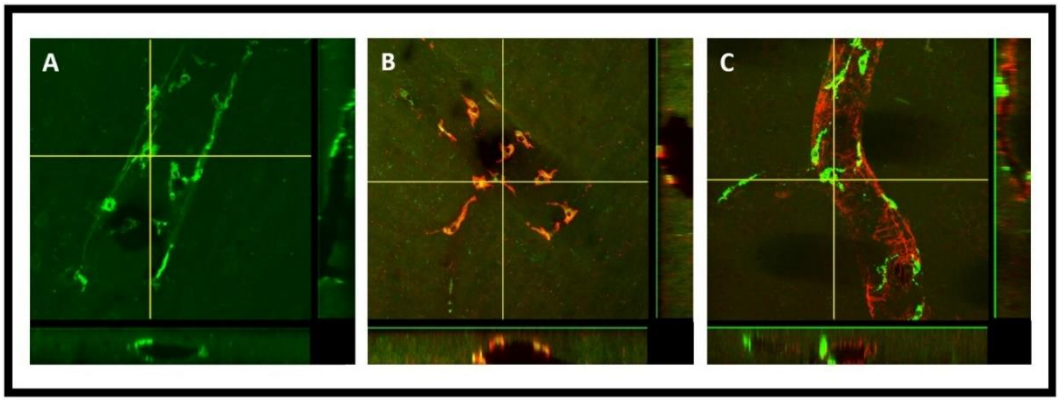

Figure 3.5- 3D cross sections of XZ and YZ planes obtained using z-stacked confocal microscopy imaging. The horizontal and vertical crosslines shown in the projection image represent the XZ and YZ planes shown at the bottom and right sides, respectively. **(A)** shows the presence of tracer and tracer accumulated PVM (green) external to the lumen, preferably in the perivascular space of the vasculature, **(B)** shows the co-localization (yellow) of PVM with the CD206 antibody (red), **(C)** shows the PVM external to the SMCs (red) in the perivascular spaces utilized by the glymphatic system.\

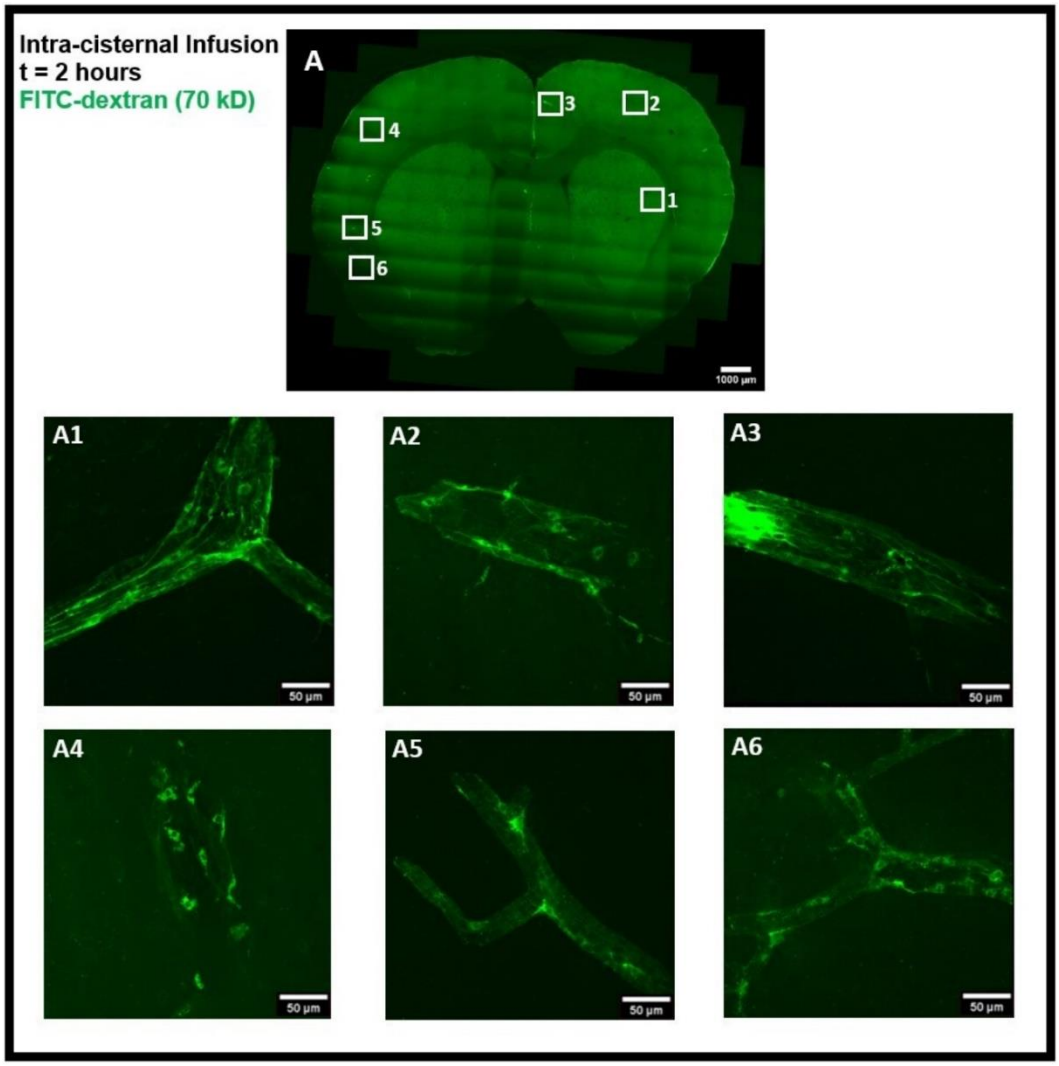

Figure 3.6- Intra-cisternal administration of FITC-dextran in the rat brain. **(A)** coronal brain section image 2 hours after infusion. **(A1-A6)** sub-images of **(A)** showing the magnified view of the presence of tracer and tracer accumulated cells (green) in the perivascular spaces in both the hemispheres of the brain.

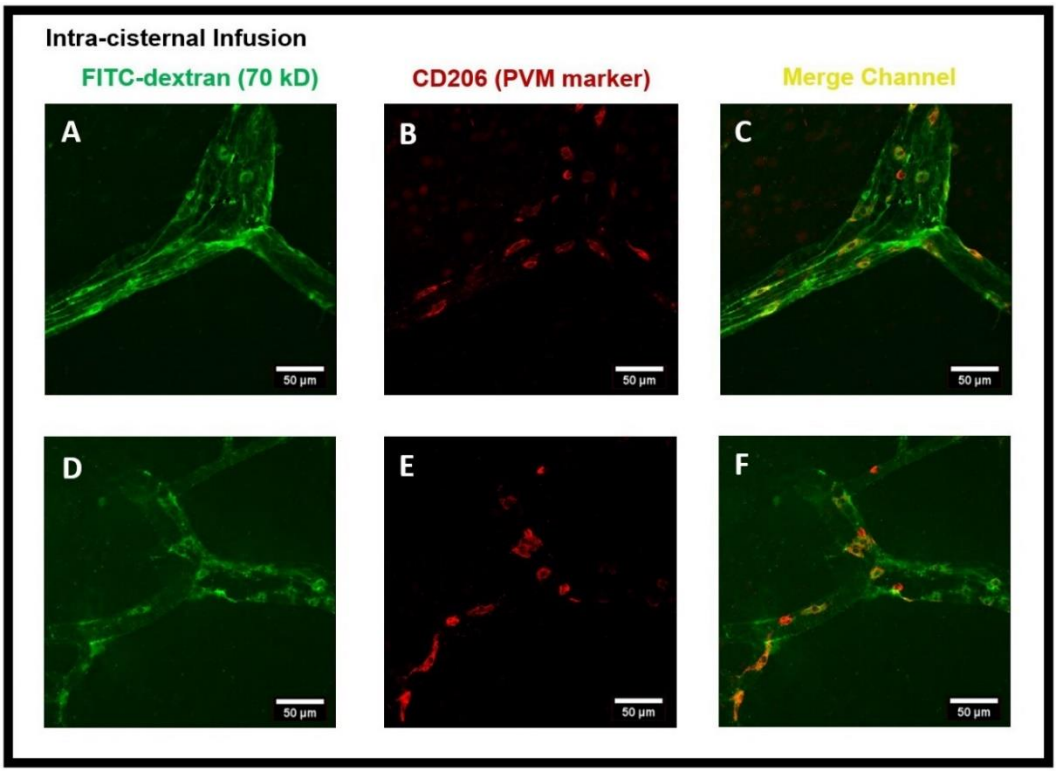

Figure 3.7- FITC-dextran tracer uptake by the perivascular macrophages (PVMs) present in the perivascular spaces after intra-cisternal administration of FITC-dextran. **(A, D)** show the tracer uptake by cells (green) in the perivascular spaces using the FITC channel of confocal imaging, **(B, E)** show the CD206 staining (red) which is a specific marker for PVM using the cy3 channel, **(C, F)** are the images from the merged channel (yellow) showing the co-localization of PVM with CD206 staining, confirming the tracer uptake by PVM.

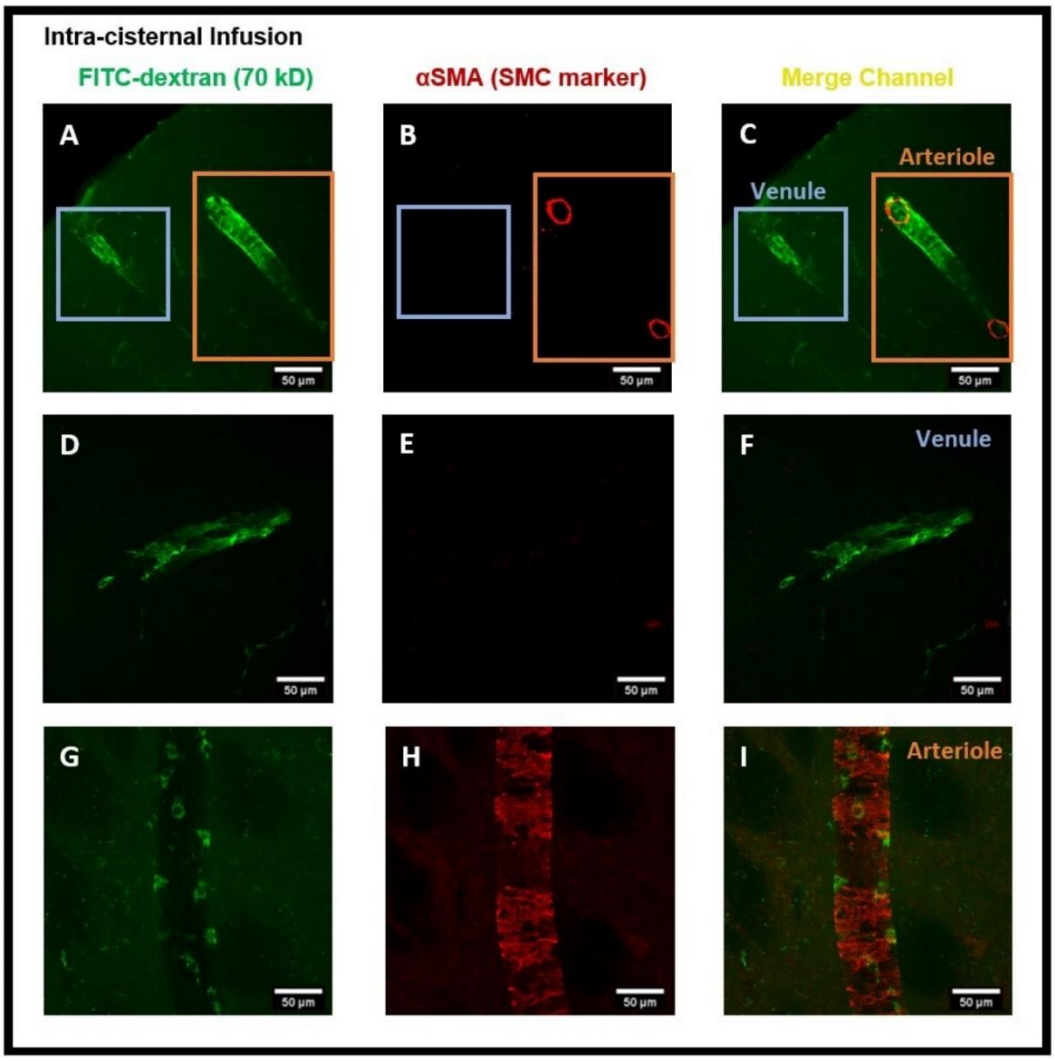

Figure 3.8- Presence of FITC-dextran and PVMs in the peri-arteriole and peri-venule spaces after intra-cisternal administration of FITC-dextran. **(A)** shows the tracer and tracer accumulated PVM (green) in the perivascular spaces of vessels, **(B)** shows the αSMA staining (red), **(C)** merged channel showing the αSMA^{+} penetrating arteriole and αSMA^{-} venule. **(D, G)** independent images of venule and arteriole, **(E, H)** αSMA staining, **(F, I)** merged channels identifying the tracer accumulated PVMs in the perivascular spaces of arterioles **(I)** and venules **(F)**.

CHAPTER FOUR

IMAGING GLYMPHATIC RESPONSE TO GLIOBLASTOMA

4.1 Introduction

Glioblastoma multiforme (GBM) is a type of glioma that arises from astrocytes and is the most aggressive form of brain tumor, classified as grade 4 in malignancy by the World Health Organization [235]. In the United States, roughly 14,000 new instances of GBM are diagnosed each year. The average survival rate for people with GBM is about 14-16 months after diagnosis. Treatments after diagnosis include surgery followed by radiation therapy and chemotherapy with temozolomide [236]. With this form of tumor, fewer than 5% of patients survive for five years or more [237]. The microenvironment in GBM facilitates the invasion of tumor cells into the surrounding healthy brain tissue [238].

The glymphatic system, discovered in 2012 [17], provides a pathway for cerebrospinal fluid (CSF) to circulate within the brain parenchyma and interact with interstitial fluid (ISF) and interstitial waste solutes, using the perivascular spaces surrounding the blood vessels for cerebral waste clearance (CWC). Dysfunction of the glymphatic system and reduced waste clearance from the brain have been reported in various neurological disorders including Alzheimer's disease (AD) [5-7, 17, 101], small vessel disease (SVD) [105, 106], traumatic brain injury (TBI) [10-12, 22, 102-104], stroke [107-109], diabetes [20], migraine [112], microinfarcts [110, 111], glaucoma [113], etc.

Recently, the dorsal mLVs have been demonstrated to be crucial for producing an effective immune response against brain tumors and draining glioma cells into cervical lymph nodes (CLNs), thereby playing a role in extracranial metastasis [239]. Since the mLVs are the potential efflux pathway for the glymphatic system and further drain the interstitial waste solutes to the CLNs [28, 29, 58, 155], we speculate that within the brain parenchyma, the glymphatic pathway may facilitate tumor invasion by providing a perivascular route for GBM cells to migrate away from the primary tumor location and invade healthy brain tissue. The highly invasive nature of GBM cells is a primary reason for the failure of conventional treatment methods [240]. Exploring tumor cell infiltration techniques and devising anti-invasive therapies are thus of great importance. Since the glymphatic system allows CSF to circulate within the brain parenchyma, it may also facilitate efficient drug delivery for GBM via intra-cisterna magna (ICM) injection. Thus, a better understanding of the functioning of the glymphatic system with GBM may have important implications for both the progression and treatment of GBM.

Using dynamic contrast-enhanced magnetic resonance imaging (CE-MRI) and our kinetic modeling, the aim of the present study is to investigate the response of the glymphatic system in rats to GBM. Our data suggest that GBM rats have an impaired glymphatic system as well as reduced CSF tracer outflow along optic nerves. The glymphatic response to GBM may impact tumor cell migration, infiltration, and drug delivery administration via the ICM pathway.

4.2 Materials and Methods

4.2.1 Animal Tumor Model and Experimental Methods

All experimental procedures were approved by the Institutional Animal Care and Use Committee of Henry Ford Health, and experimental guidelines of ARRIVE (items 8, 10 to 13). All procedures were carried out under the National Institutes of Health (NIH) Guidelines for the Care and Use of Laboratory Animals.

4.2.1.1 Rats

GBM-induced rats (3 months, male, Charles River's immunodeficient Rowett Nude (RNU), n=6) and age-matched control rats without tumor implantation (male, n=8, Charles River's Wistar, Wilmington, MA, US) were subjected to the same experimental procedures, including the ICM surgery for infusion of contrast agent and MRI measurements.

4.2.1.2 Cell Culture

Primary human glioblastoma cells HF2354 were isolated from resected GBM tissue at Henry Ford Hospital and maintained in DMEM/F-12 medium (11330032, Thermo Fisher Scientific, Waltham, MA, USA) containing 25 µg/ml Gentamicin (G1272, Sigma-Aldrich, Burlington, MA, USA), Pen/Strep (1x, 15640-055, Gibco, MA, USA), 1×N2 supplement (17502048, ThermoFisher Scientific, Waltham, MA, USA), 50µg/ml BSA (A4919-5G, Sigma-Aldrich, Burlington, MA, USA), 20 ng/ml EFG (AF-100-15, Peprotech, Cranbury, NJ, USA) and 20 ng/ml FGFb (100-18B, Peprotech, Cranbury, NJ, USA).

4.2.1.3 Intracranial Tumor Implantation

Nude rats were anesthetized with ketamine (80 mg/kg) and xylazine (13mg/kg) administered intraperitoneally (IP). After being secured in a stereotaxic device, a 3-4 mm incision was made directly down the midline, the scalp was retracted, and the cranium was exposed. Using a drill, a 2 mm craniotomy was made on the right hemisphere anterior to the coronal suture. Tumor cells were injected intra-parenchymally into the right hemisphere using a 10 µl Hamilton syringe at 2.5 mm depth, 1.5 mm to the right, and 1.0 mm anterior to the bregma. A volume of 5 µl of HF2354 glioblastoma cells (5×10^5) was injected intracerebrally. The craniotomy was sealed with bone wax and the incision was closed with a 4-0 silk suture.

4.2.1.4 Catheter Implantation into the cisterna magna

Prior to the MRI investigations, all rats were surgically prepped for catheter implantation into the cisterna magna for infusion. Isoflurane (3.0%) and a gas combination of N_2O (70%) and O_2 (30%) were used to anesthetize the rats, and once the rats were stable, the isoflurane was maintained in the range of 1.0% - 1.5%. After fixing the head in a stereotactic frame, the dorsal skin and muscle at the midline of the neck were incised, exposing the occipital bone. A 1 mm diameter hole was drilled through the skull using a Micromotor (Foredom Electric Co., Bethel, CT, USA), lateral to the midline of the skull and about 1 mm above the cisterna magna to expose the dura mater. A 27-gauge needle was used to puncture the dura mater. A part (approximately 2 mm long segment) of the polyethylene catheter (PE-10 tubing; Becton Dickinson, Cockeysville, MD, USA), approximately 10 µl in a volume filled with saline, was inserted into the cisterna magna. After that, the dura mater opening was sealed with glue, and a section of

outer tubing was superglued to the occipital bone. Finally, the skin and muscle incisions were sutured. In order to prepare for infusion, Gd-DTPA (21.7 mM) was loaded into a PE-10 catheter tube and linked to the indwelling catheter as an extension out of the MRI machine.

4.2.2 MRI measurements

A 7 Tesla MRI scanner (Bruker-Biospin, Billerica, MA, USA) was used to acquire images. A 2×2 surface array coil was utilized as the receiver, while a body volume birdcage-type coil was employed as the transmitter. The catheterized animal was securely fastened to an MR-compatible holder outfitted with an adjustable nose cone for anesthetic gas delivery and stereotaxic ear bars to restrain the head movement. The holder was pushed into the magnet and positioned at the center at the beginning of the MRI scan. A fast gradient echo imaging sequence was employed to assure the accurate positioning of the animal in the magnet. The animal's respiration (50-65 breaths/minute) was monitored (Biopac Systems Inc., Goleta, CA, USA), and their anesthesia was maintained throughout MRI measurements using Isoflurane (1.0–1.5%) and a gas combination of N_2O (70%) and O_2 (30%) (Piramal Inc., Bethlehem, PA, US). An air heating blower (Rapid Electric, Brewster, NY, US) with feedback control was employed to keep the animal's rectal temperatures at 36±1°C.

To detect the tumor volume, coronal T2-weighted imaging (T2WI) with TE = 15, 30, 45, 60, 75, and 90 ms, TR = 3 s, FOV = 32x32 mm^2, matrix = 256×256, thickness = 0.8 mm, slices = 15 was performed. The volume of the GBM was estimated as the sum of the tumor area in each slice multiplied by the slice thickness. Upon the attainment of the tumor volumes in the range of 22-77 mm^3, all rats were investigated using a dynamic CE-

MRI technique as in previous investigations [20, 80]. **Fig- 4.1A** shows the T2WI of the tumor enclosed in a red dashed line on the coronal section of the rat's brain. To measure the dynamics of the CSF tracer through the glymphatic system, 3D T1WI (TE = 4 ms, TR = 18 ms, flip angle = 12º, FOV = 32×32×16 mm^3, matrix = 256×192×96 (resolution of 0.125×0.167×0.167 mm) later interpolated to 256×256×96 voxels (resolution of 0.125×0.125×0.167 mm)) with paramagnetic contrast agent infusion of Gd-DTPA was performed. The 3D T1WI sequences continued for 5 hours, beginning with three baseline scans prior to infusion, followed by ICM administration of Gd-DTPA (85 µl, 21 mM) as a CSF tracer at an infusion rate of 1.67 µl/min for 50 min, using the indwelling catheter connected to a 100 µl glass syringe (Hamilton Robotics, Reno, NV, US) mounted on an infusion pump (Harvard Apparatus, Holliston, MA, US).

4.2.3 Data Analysis

Imaging was performed for up to 5 hours after ICM infusion to track the CSF tracer distribution in the brain over time. Motion correction for the brain was accomplished using algorithms in MATLAB and by co-registering all the volumes to the first-time point volume [241]. Furthermore, the average of all co-registered and brain-extracted T1WIs for each animal was aligned to the reference animal to create a common spatial space for all the animals. The intensity value at each time, $I_x(t)$, was used to figure out the time signal curve (TSC), which shows how the density of the tracer changes over time in each voxel x.

$$TSC_x(t) = \frac{I_x(t) - I_x(t_0)}{I_x(t_0)} \tag{4.1}$$

where t_0 is the time before infusion began.

Voxels of each brain were then clustered into comparable areas based on the tracer's propagation profile during the experiment. Following clustering, the average TSC of the voxels within each cluster was allocated to that cluster. Benefiting from clustering the tissues, we identified a local input function for any formed cluster among the TSCs of its neighboring clusters. Compared to the previous modeling with the global input function obtained from the TSC of the whole brain [90], our local input function selected for each cluster reduces errors for the modeling of CSF tracer dynamics and provides a more accurate estimation of the parameters of the glymphatic system.

To better determine the kinetics of tracer influx and clearance following Gd-DTPA infusion, four parameters were extracted from the TSC for each tissue cluster. Arrival time (t_a) is defined as the time at which the tracer enters each cluster location following infusion. Each cluster's arrival time was calculated from its TSC by identifying the time at which the signal begins to increase and remains elevated for at least three subsequent time points. The infusion rate (IR) is defined as the slope of TSC between the time of arrival (t_a) and the time at which TSC reaches its highest value (t_{max}) throughout the accumulation phase for each cluster.

$$IR = \frac{TSC(t_{max}) - TSC(t_a)}{t_{max} - t_a} \tag{4.2}$$

The clearance rate is defined as the slope of TSC for each cluster between the time at which TSC achieves its highest value and the time at which TSC relaxes at the end of the experiment. Residual (Res) is the quantity of tracer that stays in the brain tissues at the end of an experiment.

$$Res\% = \frac{TSC(t_{end}) - TSC(t_a)}{TSC(t_{max})} \times 100 \quad (4.3)$$

where TSC(t_a) is equal to zero.

After calculating the kinetic parameters in each cluster from its average TSC, parametric scalar maps of these parameters were generated as previously described [170].

4.2.4 Data quantification and statistical analysis

To evaluate the dynamics of CSF tracer distribution throughout the glymphatic system, regions of interest (ROIs) for the olfactory bulb and whole brain were manually identified on 3D T1WIs **(Fig- 4.1B, C)**. TSCs were extracted from these particular areas using ROIs, and their kinetic characteristics were then evaluated between control and GBM rats. TSCs for each tissue ROI were normalized using the bone TSC for each animal. Evaluations of the parametric scalar maps and data quantifications were performed based on these ROIs. Results of each ROI for rats with and without GBM are shown as mean ± standard error (SE) **(Fig- 4.1D, E)**. A two-sample t-test was conducted between two groups with a $p < 0.05$ statistical significance level in order to identify the effects of GBM on the glymphatic system.

4.3 Results

4.3.1 Signal intensity plots based on TSCs alterations with glioblastoma

TSCs acquired from the same brain areas (olfactory bulb and whole brain (**Fig- 4.1B, C)**) exhibited different temporal profiles between control and GBM rats as shown in **Fig- 4.1D, E**. TSCs from GBM rats revealed an initial signal rise at later time points, a reduced percentage of signal change from the baseline, and a delayed signal reduction after the peak signal as compared to the control rats. The slower rate of signal

rise before peak values with less percentage of signal change from the baseline and a slower rate of signal drop after peak values seen in these brain areas in GBM rats imply a reduced influx and delayed clearance of CSF tracer via the glymphatic system, respectively.

4.3.2 Impaired glymphatic influx and clearance of CSF tracer with glioblastoma

A comparison of CSF tracer transport through the glymphatic system over time in control and GBM rats is shown in **Fig- 4.2**. We investigated whether GBM has an impact on the glymphatic system influx and clearance mechanisms. During the 5-hour MR imaging session, the 3D dynamic T1WIs in representative control **(Fig- 4.2B)** and GBM **(Fig- 4.2C)** rats demonstrate the influx of Gd-DTPA contrast agent through time-dependent anatomical channels of perivascular spaces and other anatomical locations. The anatomical regions for the glymphatic system are marked in **Fig- 4.2A**. As shown in **Fig- 4.2B**, T1WIs in a control rat show the kinetics of Gd-DTPA as the CSF paramagnetic contrast agent enters the cisterna magna, the contrast agent enters the perivascular space of the basal artery, and the pituitary recess 15 minutes after infusion, the contrast agent movement along the olfactory artery, the olfactory bulb, and pineal recess 30 minutes after infusion, enhancement of contrast agent in the brain 90 min after infusion, clearance of contrast agent from the brain 3 hours after infusion, and clearance of contrast agent from the brain at the end of the experiment (5 hours after infusion). Within 15 minutes of infusion, the Gd-DTPA tracer was seen within the perivascular spaces around the arteries at the surface of the brain. Gd-DTPA entered the perivascular spaces of the penetrating arteries 30 minutes after infusion. Tracer entered the majority of

brain regions and started to clear out 3 hours after infusion, and most of the Gd-DTPA was cleared from the brain and olfactory bulb 5 hours after infusion.

When compared to a control rat, the time-matched T1WIs in a GBM rat as shown in **Fig- 4.2C** show a different contrast agent distribution, including increased tracer intensity in the cerebellum (when a tracer is excessively intense, the signal saturates and appears as black area, as seen in the cerebellum of a GBM rat), decreased tracer intensity in the perivascular spaces around the arteries and the olfactory bulb, and increased tracer intensity at 5 hours after Gd-DTPA infusion. Together, these data show that in GBM rats, more CSF tracer is retained in the cerebellum and less is taken up by the brain with less influx of contrast agent through the periarterial spaces, pituitary recess, and pineal recess than in control non-GBM animals. Additionally, GBM rats exhibit a decline in tracer clearance over time in the olfactory bulb and other brain regions. These dynamic images **(Fig- 4.2)** and their quantitative data **(Fig- 4.1D, E)** suggest an impaired glymphatic influx and clearance of CSF tracer in GBM rats.

4.3.3 Reduced glymphatic flow of CSF tracer with glioblastoma

Scalar maps of kinetic parameters were evaluated using our model of the glymphatic system [170] by calculating the TSCs of each cluster that represent the glymphatic flow of the CSF tracer in the brain. **Fig- 4.3** shows the scalar parametric maps of representative control and GBM rats. When the arrival time maps of control and GBM rats **(Fig- 4.3A, B)** were compared, it was observed that the tracer took longer to reach the perivascular spaces along the arteries in the GBM rat, reflecting a slower bulk speed of CSF in the perivascular spaces. Additionally, it took longer for the tracer to reach the olfactory bulb and the whole brain of the GBM rat as demonstrated in **Fig- 4.3B**. In

comparison to the control rat **(Fig- 4.3C)**, the infusion rate maps in **Fig- 4.3D** demonstrate delayed infusion in the perivascular spaces along the arteries in the GBM rat. Tracer infusion was also slower in the olfactory bulb and other brain regions of the GBM rat. Clearance rate maps indicate that the tracer was cleared more slowly from the olfactory bulb and whole brain of the GBM rat **(Fig- 4.3F)** than the control rat **(Fig- 4.3E)**. Residual maps indicated that the GBM rat **(Fig- 4.3H)** retained more tracer than the control rat **(Fig- 4.3G)** throughout the brain and the olfactory bulb at the end of the experiment.

Fig- 4.4 shows the quantitative comparison of arrival time, infusion rate, clearance rate, and residual of the CSF tracer in GBM and control group rats. Late arrival time of tracer (**Fig- 4.4A**; Olfactory Bulb: 43.15±1.91 vs. 33.21±2.10, $p=0.002$; Whole Brain: 42.79±4.59 vs. 47.95±4.30, $p=0.21$), significantly decreased infusion rate (**Fig- 4.4B**; Olfactory Bulb: 17.56±2.88 vs. 49.23±3.59, $p<0.001$; Whole Brain: 12.23±1.86 vs. 27.25±2.01, $p<0.001$), significantly decreased clearance rate (**Fig- 4.4C**; Olfactory Bulb: 5.51±1.10 vs. 10.54±0.45, $p<0.001$; Whole Brain: 2.63±0.36 vs. 4.17±0.38, $p<0.001$), and more tracer residual (**Fig- 4.4D**; Olfactory Bulb: 58.58±2.80 vs. 47.24±2.67, $p=0.06$; Whole Brain: 72.70±3.81 vs. 57.00±5.76, $p=0.007$) in the evaluated brain areas were found in the GBM rats compared to the control rats. Consistent with signal intensity plots **(Fig- 4.1)** and representative 3D T1WIs **(Fig- 4.2),** the scalar parametric maps **(Fig- 4.3)** and their quantified data **(Fig- 4.4)** with statistical differences between control and GBM rats suggest a compromised glymphatic flow in the GBM rats.

4.3.4 Impaired perineural pathway along optic nerves with glioblastoma

In rodents, macromolecular tracers from the subarachnoid space are drained into the extracranial lymphatics through perineural pathways surrounding the departing cranial nerves, including the optic nerves [136, 137, 140]. We assessed the tracer intensity along the optic nerves in control and GBM rats to see if these perineural outflow channels were active in GBM rats. **Fig- 4.5** shows T1WIs of Gd-DTPA contrast along the optic nerves over time after ICM infusion. As shown in T1WIs, a representative GBM rat **(Fig- 4.5B)** exhibited less tracer along the perineural spaces of the optic nerves than a control rat **(Fig- 4.5A)**, indicating that this outflow pathway is compromised in GBM rats.

4.4 Discussion

GBM is an aggressive type of brain tumor that may have a substantial influence on the glymphatic system, which is responsible for eliminating toxic interstitial waste solutes from the brain parenchyma. The typical path of the CSF through the brain may be compromised by GBM as these tumors grow with an increasing volume within brain tissue devoid of lymphatic vessels.

In this study, we investigated the response of the glymphatic system in rats with GBM using dynamic CE-MRI and advanced kinetic modeling. To the best of our knowledge, this is the first study to assess the glymphatic response to human-derived GBM in a rat model. The MRI data indicate that GBM rats have decreased glymphatic transport in the brain, with evidence of impaired glymphatic influx and clearance in the presence of GBM. Consistent with T1WIs, our parametric scalar maps, and representative quantified data identified a decreased glymphatic flow of CSF tracer in the GBM rats

compared to the control rats. Our data also revealed a compromised CSF tracer outflow via the perineural spaces along the optic nerves in GBM rats.

The olfactory bulb is sensitive to changes in the glymphatic system [80, 171]. In order to evaluate the glymphatic system function in rats with GBM, we designated the olfactory bulb and whole brain as ROIs. The signal intensity plots evaluated using TSCs **(Fig- 4.1D, E)** showed a slower rate of signal increase before peak values with less percentage of signal change from the baseline and a slower rate of signal decline after peak values in GBM rats than in control rats, implying a reduced influx and delayed clearance of CSF tracer via the glymphatic system. Consistently, the dynamic tracer concentration changes in T1WIs over time in GBM rats indicated reduced perivascular CSF flow along basal, olfactory, and other arteries **(Fig- 4.2C),** as well as increased tracer retention at the end of the experiment, indicating an impaired glymphatic influx and clearance in GBM rats. The glymphatic system's performance may be affected by tumor-associated inflammation, angiogenesis, and edema. Also, tumor growth may increase intracranial pressure (ICP), obstructing CSF flow and impairing the glymphatic system. AQP4 water channels are responsible for the periarterial influx of subarachnoid CSF into the brain parenchyma, the CSF-ISF exchange, and the perivenous efflux of CSF-ISF and interstitial waste solutes [80, 85]. Reduced glymphatic influx and clearance suggest alteration of astrocyte function and downregulation of AQP4 expression due to GBM. Reduced AQP4 expression with glioma has been demonstrated in a recent study [242].

Our study demonstrated the presence of Gd-DTPA tracer in the perivascular spaces along arteries and other anatomical routes that participate in the glymphatic system. However, reduced amounts of tracer entered into the brain of the GBM rats

compared to the control rats, and more tracer was retained in the cerebellum **(Fig- 4.2C)**, possibly due to elevated ICP and edema present in GBM rats than in control rats. Elevated ICP has been demonstrated in glioma rats [242]. This outcome is consistent with a recent study in glioma mice which demonstrated that after ICM infusion, less tracer entered the brain and was instead directed into the spinal space. They also demonstrated significant lymphatic outflow of CSF tracer from the sacral region in glioma versus control mice [243]. With cerebral edema and elevated ICP, CSF production also decreases in the brain [244, 245]. Reduced production and decreased outflow of CSF may have a significant impact on the glymphatic system, consistent with reduced glymphatic influx and clearance in the GBM rats observed in our study. In addition, the tumor and its microenvironment may hinder the glymphatic pathway which affects the influx and clearance of CSF tracer.

We employed advanced kinetic modeling to seek a better understanding of the function of the glymphatic system with GBM, and our efforts focused on the parametric scalar maps **(Fig- 4.3)** and quantitative analysis **(Fig- 4.4)**. Scalar maps suggested slower arrival of CSF tracer in the GBM rats **(Fig- 4.3B, 4.4A)** than in the control rats, suggesting a reduced bulk speed of CSF in the perivascular spaces as compared to the control rats. Scalar maps also suggested significantly slower infusion of tracer **(Fig- 4.3D, 4.4B)**, significantly slower clearance of tracer **(Fig- 4.3F, 4.4C)**, and more tracer residual **(Fig- 4.3H, 4.4D)** in the GBM rats than in the control rats. The parametric scalar maps and regional quantifications with statistical differences between control and GBM groups suggest a compromised glymphatic flow in the GBM rats. Reduced glymphatic flow and clearance may cause toxic solutes and pro-inflammatory signaling molecules

such as cytokines and chemokines to accumulate in the brain, causing persistent inflammation and thereby possibly encouraging the growth of GBM.

Our data also demonstrated reduced CSF tracer intensity in the perineural spaces of optic nerves in GBM rats **(Fig- 4.5B),** indicating compromised perineural pathway. These data are also consistent with a prior study demonstrating that glioma mice have impaired perineural outflow channels [243]. Our data show that the Gd-DTPA signal in the olfactory bulb, as well as in the entire brain of control rats, significantly decreased over time after reaching peak intensity; however, in contrast, the signal intensity was relatively steady in GBM rats **(Fig- 4.1D, E)**. This difference between GBM and control rat data is indicative of a reduced tracer outflow in GBM rats through the glymphatic pathways to further drain to the extracranial lymphatic vessels. Our results are consistent with earlier work, which showed that glioma mice exhibited reduced CSF drainage through the extracranial lymphatics and had significantly reduced signal intensity in the deep cervical lymph nodes and mandibular lymph nodes compared with control mice [243]. Reduced CSF outflow would likely result in less tumor-specific antigen being drained to cervical lymph nodes, resulting in reduced anti-tumoral T-cell activation and a weaker immunological response.

The dorsal mLVs have been shown to provide a pathway for tumor cells to drain into deep cervical lymph nodes and potentially contribute to extracranial metastasis [239]. However, within the brain parenchyma, the tumor cells invade the brain tissue diffusely via active cell migration [246, 247] primarily driven by the attachment-detachment mechanism of glioma cells and the dynamic remodeling of extracellular matrix [240]. Tumor cells also invade other brain regions via the perivascular spaces and

white-matter tracts [240]. While the precise association between the glymphatic system and GBM cell infiltration is unknown, the glymphatic system convective flux could play an important role in tumor cell migration. Future studies are required to determine the precise relationship between these processes. Understanding if and how the glymphatic system influences GBM growth may lead to the identification of new treatment strategies for inhibiting GBM cell invasion and increasing the survival rate of patients.

A contributing factor to the essentially ineffective treatment outcomes of GBM is that invading tumor cells are not exposed to the existing standard-of-care therapies. Generally, the therapeutic antibodies are administered by intravenous infusion [248, 249]. However, only a few antibodies enter the brain tissue due to the presence of the BBB [250]. While antibodies have restricted diffusive transport in the brain's extracellular space [25, 251], glymphatic perivascular and intra-parenchymal convective flow may be used to improve their delivery into the brain. Increasing plasma osmolality by injecting hypertonic saline or mannitol intraperitoneally has been shown to lower the ICP while increasing the glymphatic influx of ICM-injected antibodies without disruption of the BBB [252]. This technique overcomes the impaired glymphatic influx seen in the brain of awake mice and has been shown to effectively improve the delivery of an Aβ antibody, achieving a 5-fold increment in antibody binding to Aβ plaques while using significantly fewer antibodies in an AD model [252]. Thus, utilizing the brain-wide system of perivascular spaces and enhancing the glymphatic activity by increasing plasma osmolality and lowering the ICP may augment the delivery of anti-tumor drugs to the patients. Future research on utilizing the glymphatic pathway as a means to enhance drug delivery in GBM patients warrants investigation.

Additional studies measuring the glymphatic system are required due to the heterogeneity of GBM and the impact that age, gender, tumor size, and stage of the disease may have on the CSF flow. The anatomical and physiological (such as brain mass, metabolic rate, vascular pulsatility, AQP4 density, etc.) distinctions between human and rodent brains should be kept in mind when translating animal experimental results to humans.

4.5 Conclusion

To assess the response of the glymphatic system to GBM, we employed GBM-induced RNU rats and CE-MRI to dynamically monitor the Gd-DTPA contrast agent infused into the cisterna magna. 3D T1WI measurements indicate reduced tracer entry into the brain of GBM rats with some of the tracer confined in the cerebellum compared with control rats. Dynamic T1WIs and signal intensity plots reveal a delayed periarterial influx of CSF tracer and a reduced glymphatic clearance in GBM rats compared with control rats. Parametric scalar maps and regional quantitative analysis derived using kinetic modeling demonstrate significantly slower tracer arrival, slower periarterial glymphatic influx, delayed glymphatic clearance, and more retention of tracer in the GBM rats than in control rats. Our study also indicates the compromised perineural pathway along the optic nerves with GBM. Consideration should be given to utilizing the brain-wide perivascular glymphatic pathway along with increasing plasma osmolality to increase drug delivery through ICM for the treatment of GBM.

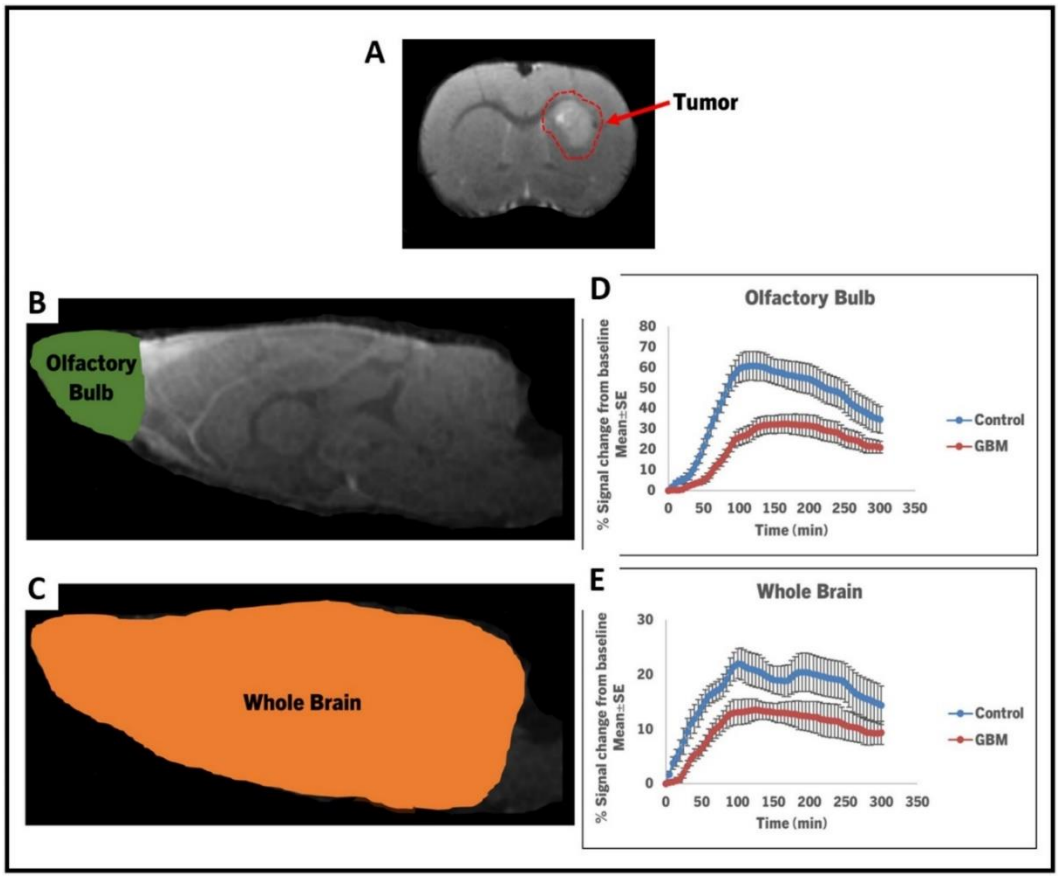

Figure 4.1- (A) T2WI shows the location of the tumor at 2.5 mm depth, 1.5 mm to the right, and 1.0 mm anterior to the bregma on the right hemisphere of the coronal section of the rat brain. The red dashed line encloses the whole tumor. Regions of interest (ROIs) for the olfactory bulb and whole brain are shown as colored anatomical areas in **(B, C)** on the sagittal sections of the rat brain. The time signal curves (TSCs) **(D, E)** are acquired from the related ROIs. Compared to the control rats, the TSCs measured from the GBM rats show an initial signal increase at later time points, a lower percentage of signal change from the baseline, and a slow signal decrease after the peak signal.

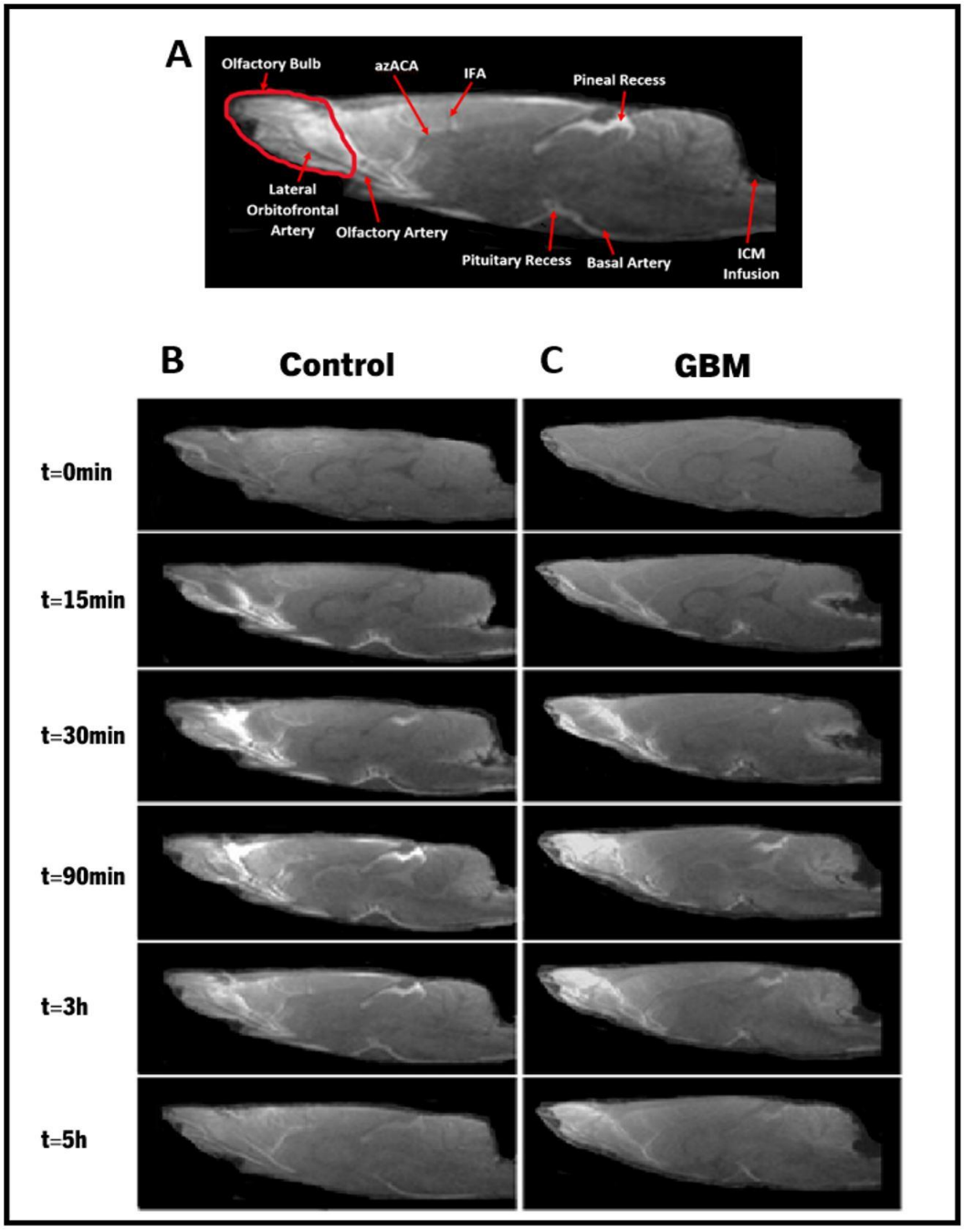

Figure 4.2- Dynamic tracer concentration changes in Control and GBM representative rats. **(A)**Visualization of key anatomical structures in the rat brain including the olfactory bulb, pituitary recess, pineal recess, ICM infusion site, and relevant arterial segments including the olfactory artery, lateral orbitofrontal artery, azygos of the anterior cerebral artery (azACA), and internal frontal artery (IFA). **(B, C)** shows the time evolution of contrast agent in control **(B)** and GBM **(C)** rats using CE-MRI, demonstrating influx (0-30 min) and anatomical glymphatic enhancement 90 min, 3 hours, and 5 hours after ICM infusion of Gd-DTPA.

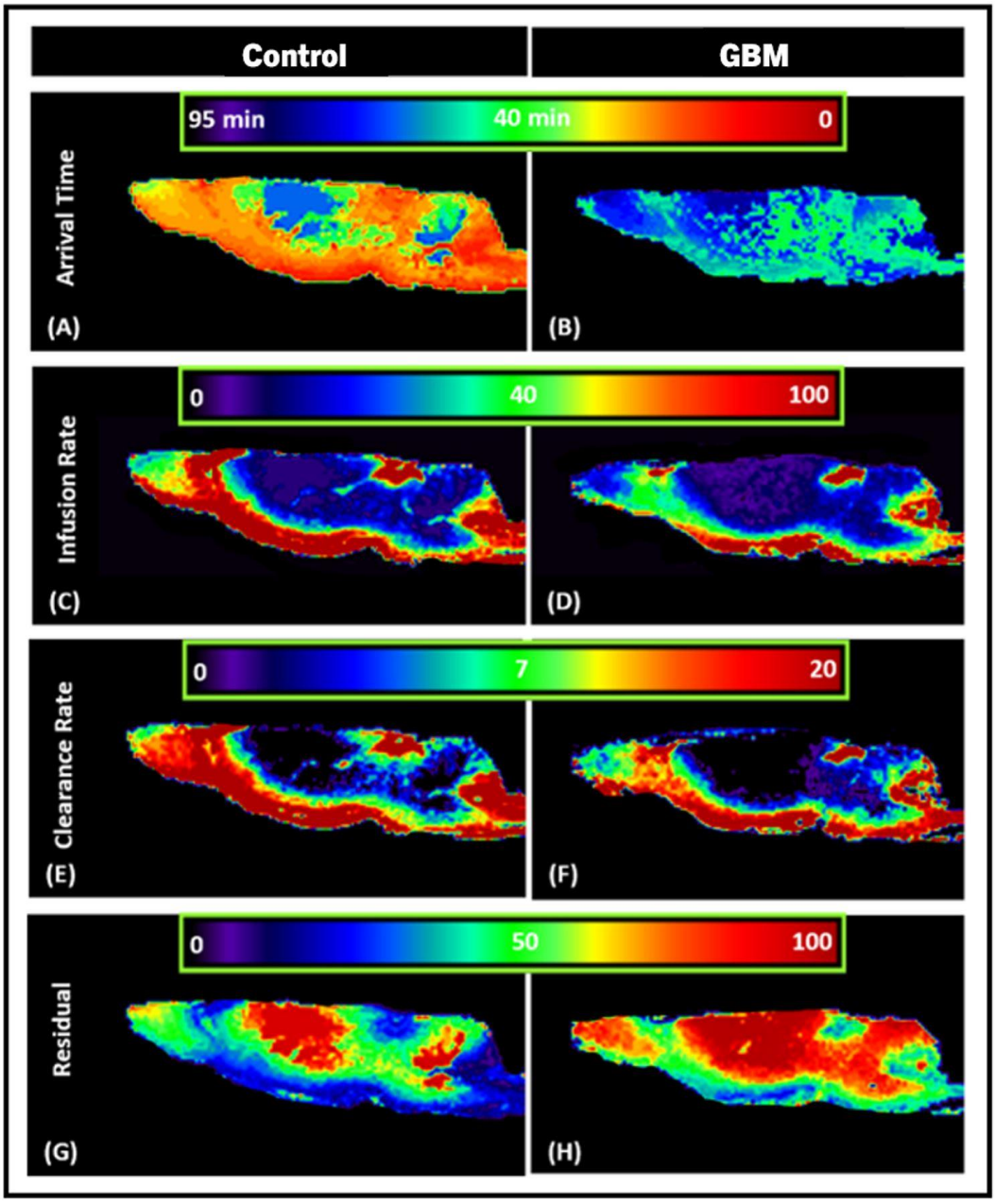

Figure 4.3- Scalar maps in Control and GBM representative rats. Hotter color (towards red) indicates quicker arrival time, faster infusion rate, faster clearance rate, and more residual of CSF tracer. **(A, B)** Arrival time maps suggest a lower bulk speed of CSF tracer in the periarterial spaces and olfactory bulb of GBM rats. **(C, D)** Infusion rate maps suggest a slower infusion of tracer in the periarterial spaces and olfactory bulb of GBM rats. **(E, F)** Clearance rate maps suggest slower clearance of tracer from the olfactory bulb and other brain regions of the GBM rats. **(G, H)** Residual maps suggest more tracer residual in GBM rats at the end of the experiment.

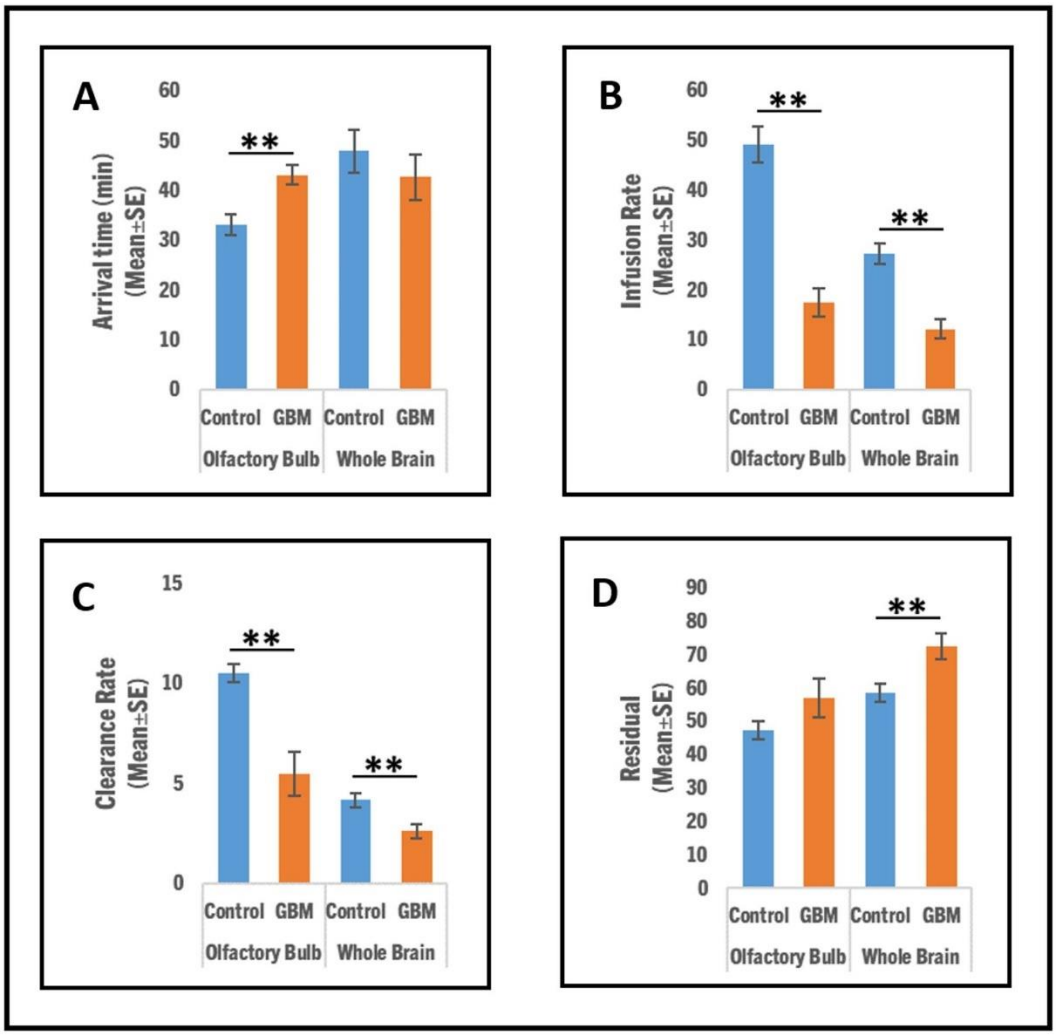

Figure 4.4- Comparison of glymphatic flow in the investigated brain areas (olfactory bulb and whole brain). Slower arrival time **(A)**, significantly reduced infusion rate **(B)**, significantly reduced clearance rate **(C)**, and increased residual of tracer **(D)** in corresponding brain regions were found in the GBM rats compared to the control rats with * $p<0.05$, ** $p<0.01$.

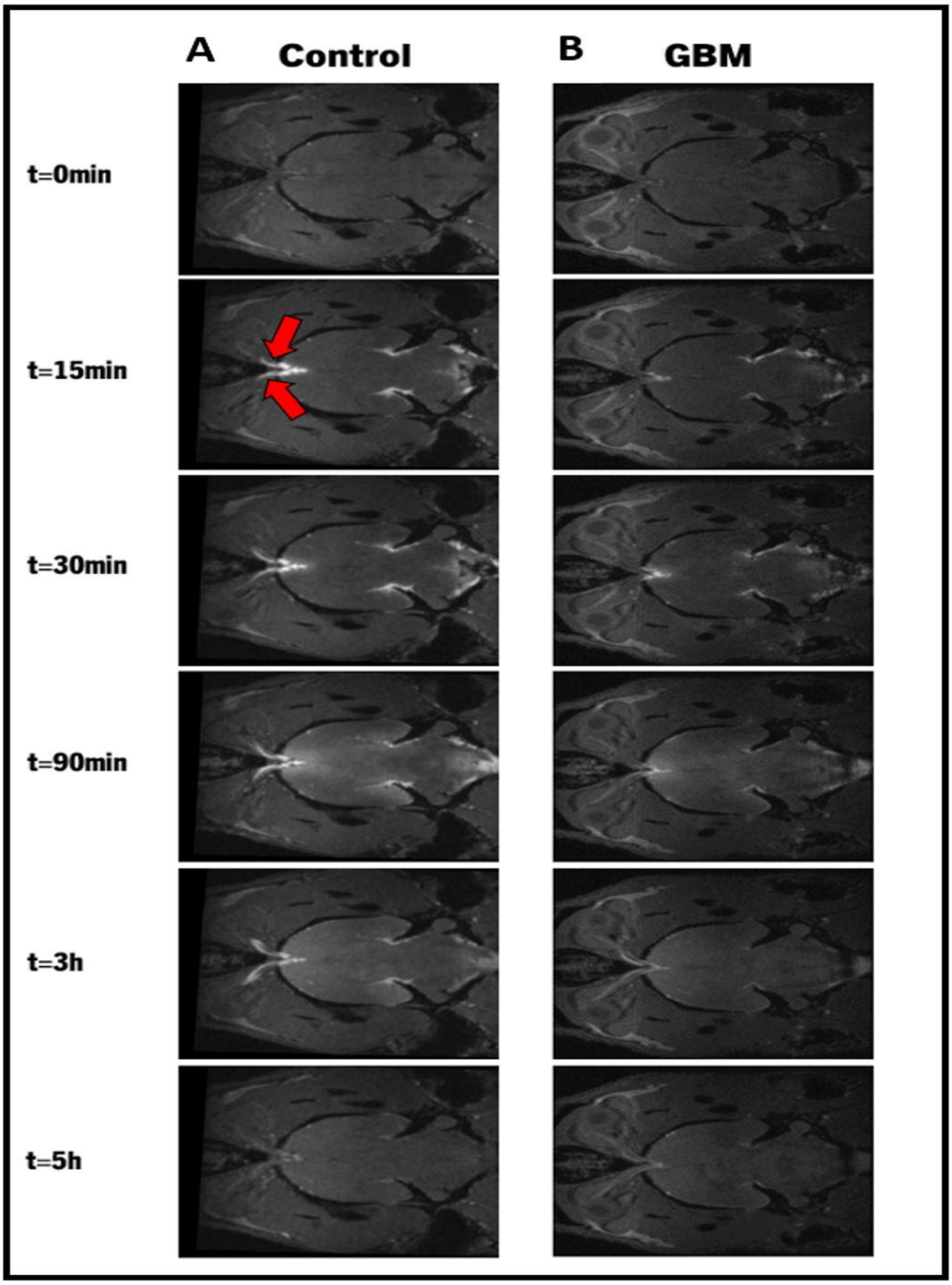

Figure 4.5- The perineural outflow pathway in Control and GBM rats. Red arrows point to the optic nerves. CE-MRI in representative Control **(A)** and GBM **(B)** rats show the dynamics of contrast agent in the perineural spaces along the optic nerves before infusion, 15 min, 30 min, 90 min, 3 hours, and 5 hours after the infusion of Gd-DTPA in the cisterna magna. These images suggest compromised outflow of CSF tracer from the perineural spaces along the optic nerves in GBM rats.

CHAPTER FIVE

MENINGEAL LYMPHATICS AS THE EFFLUX PATHWAY OF THE GLYMPHATIC SYSTEM

5.1 Background and Aim

With an increasing US aging population, it is imperative to gain a better insight into the pathophysiology of neurological diseases such as Alzheimer's disease and stroke; and, into chronic conditions such as type II diabetes mellitus (DM) which lead to neurological impairments. The glymphatic system has been implicated in these neurological conditions, as well as in many others including traumatic brain injury (TBI), multiple sclerosis, and chronic traumatic encephalopathy [5, 11, 17-21, 81, 85, 93, 155]. It is becoming increasingly apparent that this waste removal mechanism is pivotal in neurological diseases. Although significant strides have been made in characterizing the glymphatic system's influx pathways, the efflux pathways external to the brain parenchyma remain largely unclear, mainly due to technical difficulties of performing minimally invasive in vivo, ultra-high detection sensitivity measurements of influx and efflux pathways, and whole brain imaging. The meningeal lymphatic vessels (mLVs) has been recently proposed as a potential efflux pathway of the glymphatic system (the arachnoid granulations, blood-brain-barrier (BBB), and the perineural spaces along the olfactory nerves being the other three potential efflux pathways) [28, 29, 58, 139, 140, 152, 155]. In fact, Louveau *et al.* demonstrated that ablation of the mLVs was associated with a congestion of the glymphatic system and a resultant decrease in waste clearance, serving as an aggravating factor for Alzheimer's disease pathology and age-associated

cognitive decline in mice [58, 155]. The aim of this study was to investigate the mLVs as a potential efflux pathway of the glymphatic system under healthy (non-DM) and diabetic mellitus (DM) conditions in Prox1-EGFP^{+} reporter rats (Prox1, Prospero homeobox protein 1; EGFP, enhanced green fluorescent protein). We hypothesize that DM decreases waste clearance through the meningeal lymphatics.

5.2 Materials and Methods

5.2.1 Surgical procedure and sample preparation

Sprague-Dawley Prox1-EGFP^{+} reporter healthy rats were anesthetized with ketamine/xylazine intraperitoneally (IP). Intra-cisterna magna (ICM) surgery was conducted as previously reported in chapters 3 and 4, and 10 µl of quantum dots 655 (QD655) (ThermoFisher) were infused using an infusion pump at a rate of 1 µl/min. Rats were sacrificed at 15 mins, 30 mins, 40 mins, and 2 hrs after the infusion, and dura mater was perfused with PBS followed by 4% paraformaldehyde. For visualization of mLVs, the dorsal dura was carefully detached from the skull and mounted on a glass slide, which was then covered with a coverslip. The basal dura, on the other hand, was obtained without detachment from the basal cranium and decalcified with 0.5 M EDTA at 4 °C for 2 days making it softer and more amenable before being mounted on the glass slide. The dorsal and basal dura mater were then examined using an Olympus FLUOVIEW FV1200 Biological Confocal Laser Scanning Microscope to investigate mLVs as a possible efflux pathway for the glymphatic system.

5.3 Results and Discussion

5.3.1 Dorsal mLVs are not the major efflux pathway for CSF tracer

To evaluate the dorsal mLVs as a potential efflux pathway for the glymphatic system, we examined the mLVs at different time points following the ICM infusion of QD655, using confocal microscopy imaging. 15 mins after the ICM infusion, QD655 was not observed within the dorsal mLVs **(Fig- 5.1A, B)**. Following that, we monitored the dorsal mLVs at 30 mins **(Fig- 5.2A, B)**, 40 mins **(Fig- 5.3A, B)**, and 2 hrs **(Fig- 5.4A)** after ICM infusions of QD655. The QD655 was detected in the dorsal dura mater **(Fig- 5.1A, B)** and the superior sagittal sinus **(Fig- 5.2A)** of the dural venous sinus, but it was absent within the mLVs. This finding implies that the dorsal mLVs are not the major glymphatic efflux pathway for CSF tracer clearance from the brain. These findings contradict a previous work that showed the presence of QD655 in the dorsal mLVs along the superior sagittal sinus and transverse sinus from 5 to 60 minutes after ICM injection in Prox1-EGFP mice [155]. However, recent research found that dorsal mLVs play a minimal role in the clearance of CSF tracer following ICM injection of QD705 in mice [156], which supports our findings.

5.3.2 Basal mLVs are not the major efflux pathway for CSF tracer

Basal mLVs have been demonstrated as the hotspots for clearance of CSF macromolecules and their impairment with aging in mice [156]. We investigated the clearance of CSF tracer (QD655) through basal mLVs after ICM infusion in rats. We initially scanned the basal dura after detaching it from the skull and mounting on a glass slide with coverslip, however, this resulted in damaged dura mater with few intact mLVs. As a result, we attempted scanning without detaching the basal dura from the skull, but

due to the curvature of the skull, focusing on the basal mLVs was challenging. Therefore, we utilized decalcifying agent 0.5 M EDTA to soften the skull attached to the basal dura, as another research group [156] had done earlier for mice basal mLVs. After soaking for two days, we began scanning basal mLVs by placing the decalcified cranium on a glass slide and covering it with a glass slip. We did not identify QD655 in the basal mLVs of Prox1-EGFP animals at 15 minutes **(Fig- 5.1C, D)**, 30 minutes **(Fig- 5.2C, D)**, 40 minutes **(Fig- 5.3C, D)**, or 2 hours **(Fig- 5.4B, C)** after ICM infusion, but it was found in the surrounding spaces and the vasculature. This finding contradicts previous research that found QD705 was prevalent in basal mLVs 5 minutes after ICM infusion and became abundant at 15 minutes [156].

Our findings show that the dorsal and basal mLVs are not the primary efflux routes for clearance of CSF tracer/interstitial waste solutes from the glymphatic system. This is a negative conclusion, particularly for the dorsal mLVs. There has been some debate (as discussed at the ISMRM conference in 2023 and Lymphatic Forum virtual conference in 2021) recently as to whether mLVs drain cerebrospinal fluid, particularly those vessels located dorsally along the transverse sinuses and some research groups in attempting to replicate the published experiments have reached the same results as we found. Due to the unfavorable results of this work, we did not proceed with the experiments using DM animals and comparing CSF solute efflux through the mLVs in healthy and DM rats. Our study, however, suggests the need of re-evaluation of mLVs pathway as a potential efflux pathway of the glymphatic system.

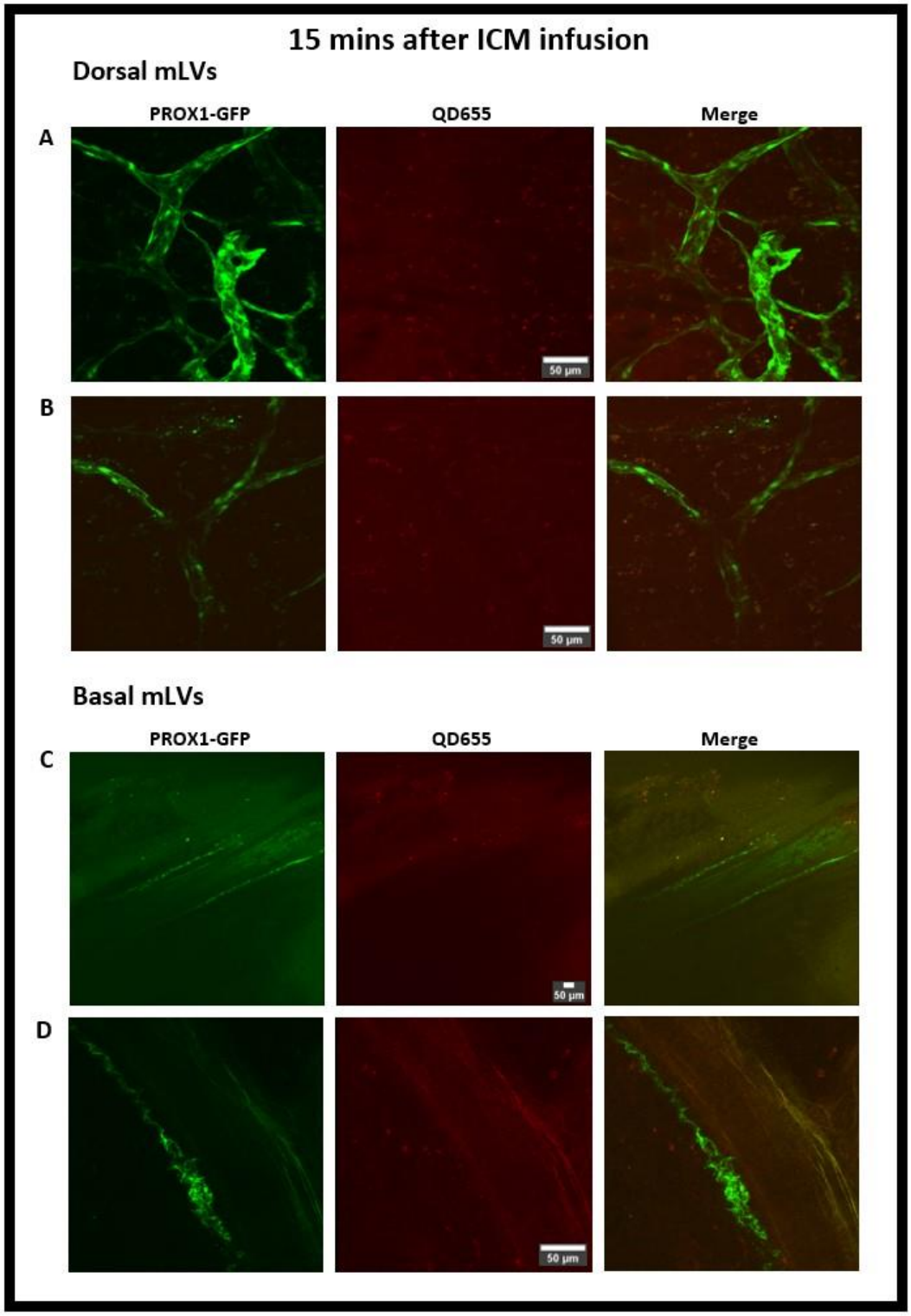

Figure 5.1- Dorsal **(A, B)** and Basal **(C, D)** mLVs 15 minutes after the ICM infusion of CSF tracer (QD655) using Confocal microscopy imaging.

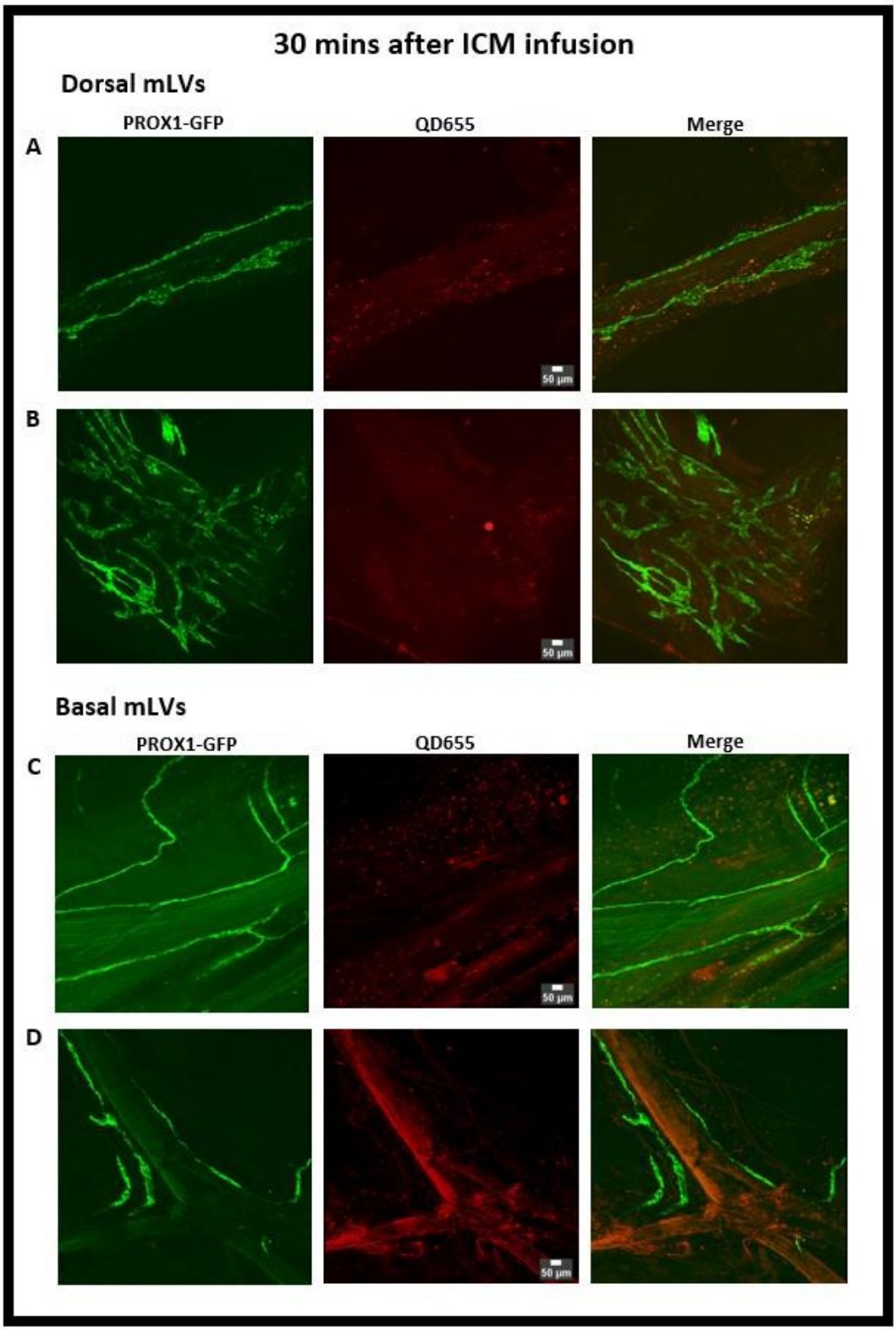

Figure 5.2- Dorsal **(A, B)** and Basal **(C, D)** mLVs 30 minutes after the ICM infusion of CSF tracer (QD655) using Confocal microscopy imaging.

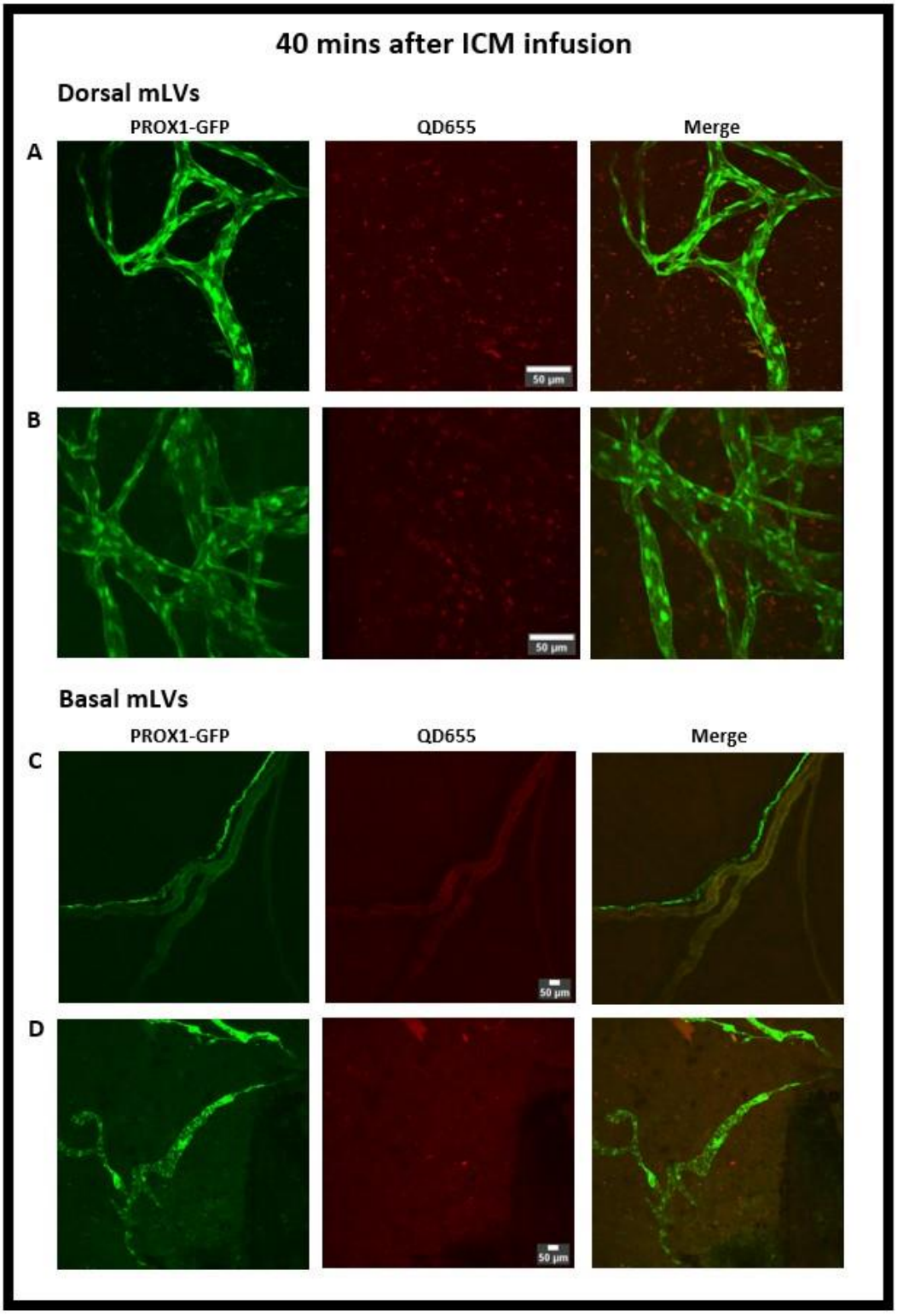

Figure 5.3- Dorsal **(A, B)** and Basal **(C, D)** mLVs 40 minutes after the ICM infusion of CSF tracer (QD655) using Confocal microscopy imaging.

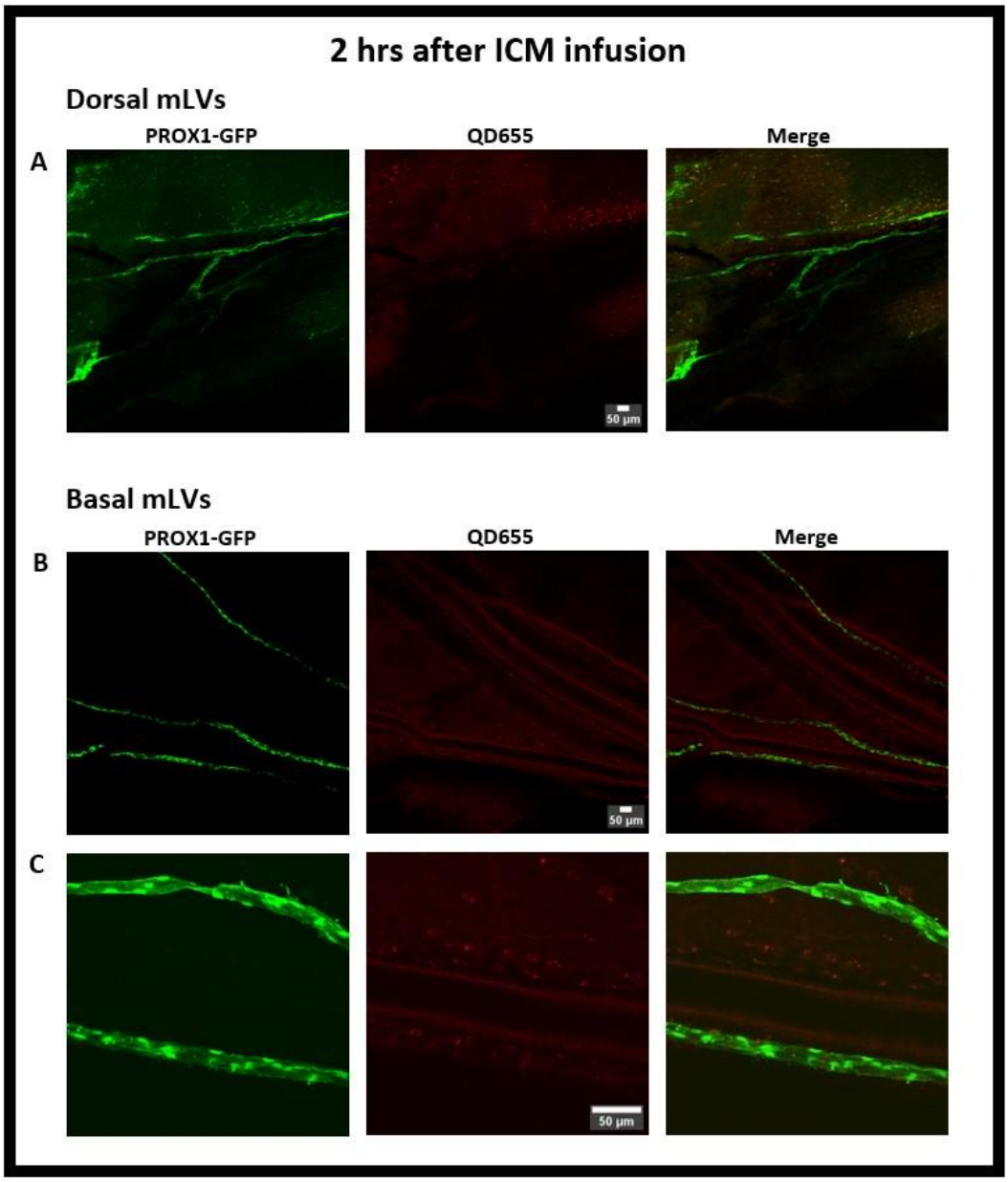

Figure 5.4- Dorsal **(A)** and Basal **(B, C)** mLVs 2 hours after the ICM infusion of CSF tracer (QD655) using Confocal microscopy imaging.

CHAPTER SIX

CLINICAL MRI EVALUATION OF GLYMPHATIC FUNCTION

6.1 Introduction

The relationship between the glymphatic system and a number of neurological conditions, covered in previous chapters, emphasizes the importance of monitoring glymphatic system functioning in humans for the early diagnosis and treatment of neurological disorders. This chapter mainly focuses on translational issues of MRI studies to-date of the glymphatic system in humans, as well as prospective non-invasive techniques to translate the glymphatic system MRI measurements from animals to humans.

6.2 MRI measurements of glymphatic related CSF/ISF flow

In 2012, the glymphatic system was initially investigated in-vivo using CSF fluorescent agents injected into the cisterna magna of the mouse brain [17] . The dynamics of the CSF tracer entering and leaving the brain parenchyma via the perivascular pathway were seen using a two-photon laser scanning microscope [17]. This method allows for in-vivo, real-time observations that can examine molecular-size-based distributions within the brain parenchyma. However, this method is invasive since it necessitates the removal of a section of the animal's cranial bone, and it has a low penetration depth that only allows the cortical regions to be examined. Moreover, this technique cannot be translated to humans to non-invasively investigate the glymphatic transport across the whole human brain. After the initial publication supporting the glymphatic hypothesis, additional research examined the glymphatic system using MRI,

since MRI is non-invasive and provides kinetics of gadolinium-based contrast agents throughout the brain [80]. By measuring the movement of this contrast agent over time, researchers can assess the function of the glymphatic system and identify potential abnormalities.

Some MRI-based research studies later discovered that the animal study findings of a glymphatic system are also present in the human brain [161-167]. Currently, the most reliable MRI glymphatic studies in humans are those that are minimally invasive, requiring an intrathecal administration of a gadolinium-based MRI contrast agent, a method not suitable for long-term clinical measurements. Also, high-dose gadolinium-based contrast agents may result in encephalopathy, a potentially neurotoxic condition [253-255]. This procedure is also time-consuming since patients must return for scanning at various intervals in order to analyze the dynamics of the contrast agent via the glymphatic system.

In addition to the gadolinium-based tracer studies, various non-invasive, diversified MRI techniques, such as phase-contrast and diffusion-weighted imaging have been proposed for clinical-related glymphatic measurements in patients.

6.2.1 Gadolinium-based MRI

6.2.1.1 Intrathecal administration of gadolinium-based contrast agent

The first glymphatic study in humans was carried out using T1-weighted imaging in control and in idiopathic normal pressure hydrocephalus (iNPH) patients after intrathecal administration of Gadobutrol. In contrast to the control group, glymphatic MRI scans performed over 24 hours revealed delayed glymphatic clearance in patients with iNPH [165]. Overnight, the brain parenchyma of both control and iNPH patients

displayed peaked tracer enhancement, presumably highlighting the important role of sleep in the glymphatic system. Later, T1-weighted MRI scans were carried out at specific intervals, such as 24 hours, 48 hours, and 4 weeks in iNPH dementia patients and in reference individuals. This study also demonstrated delayed glymphatic clearance in iNPH dementia patients [164]. Additionally, it has been suggested that dementia in iNPH patients may result from reduced glymphatic clearance and more accumulation of toxic waste solutes in the brain [162]. Using T1-weighted MRI, Eide *et al.* found that the intrathecally injected CSF tracer (Gadobutrol) drains to the cervical lymph nodes and that the tracer enhancement in the lymph nodes coincides with the glymphatic enhancement instead of CSF enhancement [161]. Using T1 maps, the glymphatic flow in a patient was quantified following intrathecal Gadobutrol administration [166]. In line with the findings of animal research, a recent human investigation revealed that both the recently discovered waste clearance pathways (glymphatic pathway and putative meningeal lymphatic pathway) deteriorate with aging and exhibit reduced clearance from the brain [159]. Reduced clearance from the human brain with sleep deprivation [256] and poor quality of sleep [257] have been demonstrated using intrathecal administration of Gadobutrol.

6.2.1.2 Intravenous administration of gadolinium-based contrast agent

The glymphatic system in the human and animal brain has also been studied using intravenous gadolinium-based contrast agent infusion; however because of the presence of BBB, the concentration of tracer that enters from the blood to the CSF is too low to be identified directly by T1-weighted MRI [258-261]. Furthermore, after intravenous injection of a gadolinium-based contrast agent, it was demonstrated that older patients

(above 37 years old) had considerably increased degree of tracer leakage from the cortical veins to the nearby CSF space [262, 263]. Another study found that, when compared to controls, early AD patients had significantly elevated rates of BBB leakage in both the cortex and total gray matter [264]. The intravenous administration of a single dose gadolinium-based contrast agent over 24 hours may be utilized to track the transfer of gadolinium-based contrast agents to the CSF by 3D-real inversion recovery (IR) imaging and to the CSF and brain parenchyma by MR fingerprinting. Signal intensity changes over time in the CSF may serve as a potential biomarker for the glymphatic system functioning in the clinical setting [265, 266].

6.2.1.3 Challenges of gadolinium-based MRI in humans

A main difference between human and rodent studies of the glymphatic system using an intrathecal MRI contrast agent is the time course of the gadolinium-based CSF tracer influx and clearance from the brain. It takes ~30 minutes for the tracer to start to distribute throughout the brain parenchyma and about 6-8 hours for the tracer to clear out from a rat's brain [20, 80]. However, for a human brain, tracer starts to distribute throughout the brain parenchyma 1-2 hours after infusion, and significant clearance may take up to 48 hours or more [164]. Slower CSF tracer uptake and clearance in the human brain than in the rat brain may be linked to physiological factors such as changes in vascular pulsatility, metabolic rate, brain mass, AQP4 density, etc. [154]. Therefore, to estimate the brain-wide concentration profile of the CSF tracer, the subject needs to be scanned at multiple times points (at least 3 times: baseline, at or near the maximum level of tracer enhancement, and when the tracer is almost cleared from the brain). The CSF tracer's concentration profile will be more precisely obtained by additional scanning over

time. This can readily be done for rodents because the animals can be kept in the MRI setting for the whole-time course of ~ 5-6 hours under anesthesia, but not in humans. Furthermore, the need for intrathecal injection of gadolinium-based MRI contrast agent, as well as the association of high-dose contrast agent with encephalopathy, makes this approach challenging. Despite the difficulties and limitations, gadolinium-based MRI studies remain the most accurate and reliable method to evaluate the glymphatic system in humans currently. However, there is a compelling need to develop patient convenient techniques for clinical glymphatic examinations.

6.2.2 Diffusion-weighted MRI

In diffusion-weighted MR imaging, the diffusion parameter is estimated based on the phase shift due to the diffusion of water molecules in response to diffusion-sensitizing gradients during the imaging interval. Recent human studies of the glymphatic system are using DTI based analysis along the perivascular space (DTI-ALPS)-index [267]. However, DTI-ALPS may only measure diffusion contribution but not glymphatic flow. This index is a measure of water diffusivity in the perivascular space, perpendicular to the fiber bundles in the white matter outside of the lateral ventricular body, which is correlated with interstitial fluid dynamics [267]. A high ALPS index is an indication of an effective clearance of waste solutes through the glymphatic system [267]. DTI with a low b-value diffusion gradient (5-10 s/mm^2) can be used to assess bulk flow CSF velocity in ventricles (and possibly in perivascular spaces) and then associate bulk flow CSF velocity with the glymphatic clearance function. Higher order diffusion-weighted imaging along with muti-compartment modeling has also shown promising results to link water diffusion with glymphatic system function [268-276].

6.2.2.1 DTI-ALPS

Recently, many studies have employed DTI-ALPS to associate glymphatic system impairment with neurological diseases such as AD [267, 277-280], Parkinson's disease (PD) [281], iNPH [282-284], diabetes [285], subacute ischemic stroke [286], and cerebral small vessel disease (CSVD) [287, 288]. One of the main advantages of this method is that it does not need a special imaging protocol. A regular clinical DTI protocol is sufficient to calculate the ALPS index. Also, this index can be extracted from available DTI data sets, retrospectively. Moreover, the ALPS index is robust under a fixed imaging method even when different scanners are used [289]. The reproducibility of the ALPS index can be improved by reorienting the DTI maps to a standard atlas [290] and by preserving tensor vector orientation information [291].

In 36 patients with AD, 44 patients with mild cognitive impairment (MCI), and 31 healthy controls, the ALPS index was significantly lower in the AD group compared to the controls [277]. The lower ALPS index suggests lower water diffusivity along the perivascular space and dysfunction of the glymphatic system. In another study on 130 patients with young-onset Alzheimer's disease (YOAD) and 137 age-matched controls (CTLs), the YOAD group had a significantly lower ALPS-index [279]. The effect of aging and cognitive impairment on the glymphatic system was investigated in an elderly cohort of 10 normal, 10 MCI, and 16 AD subjects [280]. DTI-ALPS index was significantly correlated with the cognitive scores and reduced in both MCI and AD groups compared with the control group [280]. In a study of Parkinson's disease (PD) [281], (25 PD patients with normal cognition (PDN), 25 PD patients with mild cognitive impairment (PD-MCI), 38 PD patients with dementia (PDD), and 47 normal controls

(NC)), lower diffusivity along the perivascular space, represented by lower ALPS index, was found in PD-MCI and PDD groups. The DTI-ALPS indexes of three groups (each group consists of 12 subjects) of iNPH, pseudo idiopathic normal pressure hydrocephalus (piNPH), and control were compared [282]. The ALPS index was significantly different among all three groups and lowest in the iNPH group. In another study, the DTI-ALPS index of a group of 16 iNPH was lower than in a control group of 16 subjects [283]. In addition, iNPH patients unresponsive to the treatment had an even lower ALPS index than the iNPH patients with symptomatic relief due to the treatment [283]. A DTI-ALPS study on 20 patients with type 2 diabetes mellitus (T2DM) showed a reduced ALPS index compared to the control group of 10 subjects, and the impaired water diffusivity was associated with the severity of T2DM [285]. In an elegant study on cerebral small vessel disease (CSVD) patients, supported by intrathecal administration of gadolinium, the DTI-APLS approach was found to be a promising non-invasive tool to connect CSVD with glymphatic clearance impairment [287]. This study employed a large population of 2219 community-dwelling people and concluded that reduced ALPS indexes are associated with the severity and typical neuroimaging markers of CSVD in the aging population [288]. One of the limitations of DTI ALPS is that it uses a high b-value (~1000 s/mm^2) which only measures diffusion but not perivascular flow.

6.2.2.2 Low b-value DTI

Some studies have correlated the diffusion coefficient measured by low b-value DTI to the velocity of the spins bulk flow [292-303]. A low b-value diffusion gradient (5-10 s/mm^2) can be used to assess bulk flow velocities [292, 293, 304], perfusion imaging [305], and functional MRI [294]. Apparent diffusion coefficient (ADC) measurements

using low b-values show restricted diffusion of CSF in choroid plexus cysts [295]. By employing low b-value DTI [297], CSF regions in the brain (particularly around the foramen of Monro, the aqueduct, the prepontine cistern, the middle cerebral artery, and the Sylvian fissure) are found to have a large and anisotropic diffusivity, showing an intensive pseudorandom flow of CSF. Low b-value DTI measurements of the Sylvian sinus reveal that the driving force behind CSF flow pulsation is independent of direct artery pulsations and may be connected to cerebral hemisphere pulsations [298]. A comprehensive animal investigation [299] demonstrated that the directional CSF flow has a distinct effect on diffusion signals by examining the influence of CSF flow on the diffusion signals at low b values of the ventricle in live and sacrificed rat brains. Additionally, it was demonstrated that the ADC may be used to evaluate both the pathological condition of the brain and the flow of CSF [299]. By employing phase contrast imaging, the phase shift in MRI diffusion images was used to measure the CSF flow velocity in optic nerve in patients with normal tension glaucoma [300] and in patients with idiopathic intracranial hypertension (IIH) [301]. In both patient groups, CSF flow velocity was lower than that of the healthy controls.

6.2.2.3 Dual-compartment DTI

DTI acquisitions with low and high b-values can be used in dual-compartment modeling for fast and slow diffusion [268-270]. In dual-compartment DTI, at least two sets of DTI with low b-value (50-150 s/mm^2) and high b-value (900-1500 s/mm^2) are acquired. Then, the data are fit to a bi-exponential model with fast and slow diffusion coefficients. Dual compartment analysis of DTI data showed that diffusivity parameters increase from PM to AM and were associated with an increase in the volume fraction of

CSF-like free water [268]. Moreover, during sleep slow-ADC (which is dominated by diffusion) is increased, while fast-ADC (which is dominated by bulk flow) decreases [269]. Another study on healthy adults [270] discovered an increase in water diffusivity (measured by DTI) overnight during sleep. This was positively correlated to the proportion of total sleep time spent in rapid eye movement (REM) sleep (measured by EEG). Moreover, it was found that CSF flow (measured by PC-MRI) increases overnight.

6.2.2.4 Advanced DWI methods

To evaluate the glymphatic system, DTI can only detect micro displacement of the molecules (in the order of μm) which is not suitable to measure bulk movement and velocity of the flow in the perivascular spaces and in the brain parenchyma. Diffusion-weighted MRI sequences with ultra-long echo times (TE) were designed to quantify fluid flow within perivascular channels [271]. In this technique, a diffusion-encoding gradient was employed to quantify the fluid motion within the perivascular space surrounding the middle cerebral artery (MCA) of the rat brain [271]. These methods need a relatively long acquisition time and therefore are not suitable for clinical studies. To solve this issue, Wen *et al.* (2022) proposed a diffusion imaging and analytical framework called dynamic Diffusion-weighted Imaging (dDWI), which uses retrospective cardiac gating data to analyze DW images with a b-value of 150 s/mm^2 to detect CSF dynamics in the surface perivascular space surrounding the arteries throughout a cardiac cycle [292]. dDWI can detect pulsatile CSF waveforms in the perivascular spaces close to both big and small arteries [292]. In [273], the CSF dynamics were assessed using a scoring method by creating Diffusion ANalysis of fluid DYnamics with Incremental Strength of Motion proving gradient (DANDYISM) maps from DWIs, with multiple b values of 0,

50, 100, 200, 300, 500, 700, and 1000 s/mm^2. However, an apparent significant drawback of this method is the lack of quantitative information. It is reliant on qualitative DWI contrast, which is sensitive to acquisition parameters and thus is hard to generalize. Furthermore, its scoring methodology entails a somewhat labor-intensive process, potentially restricting its applicability in both research and in clinical studies.

6.2.2.5 Estimating CSF/ISF diffusion from CE-MRI

It is worth noting that ADC of CSF tracer can also be estimated from T1-weighted images [306]. However, it is totally different from ADC estimated from DTI. ADC estimated from T1-weighted images is affected by both bulk flow and diffusion. In [306], ADC of glymphatic CSF was determined at the macro-level based on the distribution of Gadobutrol in CSF and brain tissue following intrathecal injection using PDE-constrained optimization and employing CSF-tracer concentrations at multiple time-points during 48 hours [306]. The ADC estimated from this approach is higher than the corresponding numbers acquired using DTI.

6.2.3 Phase Contrast MRI

One of the key aspects of studying the glymphatic system is to measure the flow dynamics of CSF within the glymphatic pathway and study its alteration under different neurological conditions. Phase contrast MRI (PC-MRI) has been developed to quantify the cerebral fluid (such as blood or CSF) dynamics from the phase information of the MRI signal [307-309]. This is accomplished by the fact that the phase of the MRI signal shifts due to the movement of the particles (spins) during the imaging intervals. As the main component of the glymphatic system is CSF, any neurological disease affecting the glymphatic system may also alter the CSF dynamics in ventricular/perivascular spaces.

Generally, a dysfunction of the glymphatic system in clearing the waste solutes could be associated with slower CSF velocity in ventricular/perivascular spaces. Therefore, PC-MRI may be a potential tool to detect glymphatic system alteration in neurological diseases by investigating the CSF dynamics.

6.2.3.1 PC-MRI in neurological conditions

PC-MRI has been examined for use in neurological conditions that primarily affect CSF. Quantitative measurements of aqueduct CSF flow, including peak systolic velocity (PSV), peak mean velocity, and aqueduct CSF stroke volume can differentiate normal-pressure hydrocephalus (NPH) from brain atrophy [310]. In fact, NPH patients show significantly elevated PSV, peak mean velocity, and stroke volume values [310]. When a ventricular shunt is suspected of malfunctioning, CSF flow assessed by PC-MRI within the parenchymal section may accurately reveal the shunt's functional condition [311, 312]. In a study, employing PC-MRI [313] to quantify CSF flow dynamics at the aqueduct level, it was found that schizophrenic patients have lower CSF peak velocity and lower average CSF flow than controls. Moreover, the average CSF velocity was significantly reduced in patients with violent behavior compared to non-violent patients. PC-MRI can characterize blood flow pulsatility in cerebral arteries, larger cerebral veins, and CSF [314, 315]. Patients with hypertension have reduced CSF flow dynamics as evaluated by Cine PC-MRI, which is related to their elevated systolic blood pressure [316]. Other applications of using PC-MRI include assessing CSF flow blockage before intraventricular chemotherapy infusions [317], evaluating acute intracranial hydrodynamic changes after subarachnoid hemorrhage [318], a cognitive deficit in elderly patients [319], multiple sclerosis (MS) [320], Chiari type I [321], idiopathic

intracranial hypertension (IIH) patients [322, 323], and idiopathic normal pressure hydrocephalus [324].

6.2.3.2 PC-MRI validation

The reliability of CSF and cerebral blood flow (CBF) flow quantities using PC-MRI was validated in the cerebral aqueduct (CA) and C2-C3 areas [325], which makes it an excellent tool to study flow dynamics in the central nervous system. Many factors such as body posture [326] and the rate and depth of respiration [327, 328] can rapidly modify the CSF flow dynamics in and out of the skull. However, there are no appreciable differences between age and sex in the typical CSF flow characteristics evaluated by PC-MRI at the aqueduct [329]. By assessing net CSF flow and stroke volume in the aqueduct over the cardiac cycle using PC-MRI, it was found that PC-MRI cannot be directly linked to the CSF production in the lateral ventricles because the net CSF flow is confounded by respiration effects [330].

6.2.3.3 PC-MRI limitations

The use of PC-MRI to determine flow velocity has limitations. The PC-MRI slice orientation with regard to the direction of flow should be carefully adjusted. A slice orientation of less than 10° from the vessel's axial plane is required for reliable CBF quantifications [331]. A typical clinical PC-MRI scan may measure speeds as low as 1 to 5 cm/s, which is acceptable for CSF flow [292]. Partial volume effects may also act as a limitation in PC-MRI due to the limited spatial resolution of MRI for small perivascular spaces that provide a challenge to distinguish between blood and CSF flow.

Detecting CSF flow dynamics in the perivascular spaces solely using PC-MRI is problematic. Perivascular CSF is too difficult to map and measure with PC-MRI because

it is slower than blood flow and is hindered by diffusion weighting [292, 332-334]. Furthermore, it is significantly slower in rodents than in human brains, where PC-MRI is hampered by gradient hardware defects that cause phase inaccuracy.

6.3 Other MRI measurements of glymphatic related CSF/ISF flow

Other techniques for visualizing CSF dynamics include MRI tracer studies using stable isotope ^{17}O, radioisotope (RI) cisternography using ^{111}In-DTPA, and computed tomography (CT) cisternography using an iodine-based compound. The direct stable isotope ^{17}O technique, however, has reduced signal-to-noise ratio, limited spatial resolution, and necessitates specialized equipment for ^{17}O detection [335, 336]. RI and CT cisternography investigations, on the other hand, require ionizing radiation. However, there is an indirect stable isotope ^{17}O method using proton MRI to identify ^{17}O-labeled water tracer dynamics in the brain parenchyma and CSF spaces, and the role of AQP4 in water influx into the CSF [335-337]. Unfortunately, ^{17}O-labeled water is expensive, with prices per milliliter reaching several hundred dollars, and an intravenous dose may necessitate more than 100 ml [338].

To evaluate the CSF dynamics, non-invasive inversion pulse techniques without the use of any external tracer administration have been used including Spatial modulation of magnetization (SPAMM) [339, 340], Time-spatial labeling inversion pulse (Time-SLIP) [341, 342], and arterial spin labeling (ASL) [41, 343]. SPAMM has been employed to study intracranial CSF transport in order to detect irregularities in CSF dynamics [339]. This technique, for example, was used in cases with Chiari malformation to assess the CSF flow following cranio-cervical junction decompression [340]. Another approach for visualizing CSF movement is Time-SLIP MRI, which involves delivering a slab of

inversion pulse to CSF in the area of interest. This approach demonstrated that CSF is refluxed from the third to lateral ventricles in the normal brain, implying active exchange through the foramen of Monro. In hydrocephalus patients, however, no CSF reflux was identified [341, 342]. The role of AQP4 in water exchange across the blood-brain interface has been investigated utilizing the ASL approach [343]. By calculating the time it takes for magnetically labeled intravascular water to pass the blood-brain interface, multiple echo time ASL was utilized to assess the blood-brain interface's water permeability. The findings showed that AQP4-deficient animals had slower exchange rates than wild-type mice, highlighting how sensitive the method was to the absence of AQP4 water channels [343]. The Time-SLIP [341, 342] and ASL [41, 343] have shown reduced CSF flow across the choroid plexus in the lateral ventricles except in the area adjacent to the foramen of Monro. Also, rapid brain-wide blood-to-CSF water transport including brain parenchyma and the subarachnoid spaces has been demonstrated. These findings suggest that there may be additional, previously underappreciated mechanisms involved in CSF production and regulation [40, 41]. It has been suggested that in addition to the choroid plexus, capillaries located inside the brain parenchyma also generate CSF [42].

T2 component analysis has the potential to evaluate the glymphatic system in the brain [344]. It is feasible to isolate the decaying signal's individual T2 components from the multi-echo images. The distribution of extracellular water and its T2 values may be seen by altering the color table to produce the color map. It has been observed that CSF in the subarachnoid space and ventricles have long T2, but short T2 components have been observed in the brain surface, dura's surface, blood vessels in the subarachnoid

space, and brain parenchyma (T2 is longer than intracellular components but shorter than CSF). This can be considered similar to the dispersion of waste products in the brain [344]. Low-frequency CSF oscillations have been measured using ultrafast fMRI [345].

6.4 Discussion

MRI based clinical research of the glymphatic system is still in an early stage. Currently, using gadolinium-based MRI contrast agents is the most accurate approach to measure CSF dynamics associated with this system. The limitations of this method are the long-time monitoring period (up to 72 hours) of the patients and the need to inject (intrathecal or intravenous) an MRI contrast agent. Moreover, the tracer enhancement could be low if insufficient dose for tracer is used. Using ^{17}O as a contrast agent is too expensive. Also, it can diffuse in both directions from blood to brain parenchyma and vice versa. Therefore, it is difficult to distinguish the contributions of glymphatic and vascular systems in the clearance of ^{17}O. On the other hand, techniques like Diffusion-weighted MRI and PC-MRI are showing promise to detect CSF dynamics in ventricles, and in perivascular and interstitial spaces without a need for a contrast agent administration.

It should be noted that many clinical studies evaluating the CSF dynamics can be indirectly linked to the glymphatic system. A decrease in CSF velocity measured by PC-MRI at the cerebral aqueduct may indicate insufficient glymphatic flow and inefficient CWC. Similarly, an altered ADC measured by low b-value DTI in the ventricles may imply that CSF flow is altered, and this can be caused by a change in the glymphatic system function or structure of the ventricles. The variation in CSF flow, however, may be caused by mechanisms other than the glymphatic system, such as vascular pulsations.

Another drawback of these methods is that they can only be used on specific areas of the brain, such as the ventricles, where there is sufficient CSF for MRI detection.

As noted above, to study the glymphatic system using MRI, parameters related to both the anatomical structures and the CSF dynamics should be considered. Among the recent MRI techniques, diffusion MRI has the most potential for clinical application. Firstly, it does not require any contrast agent to be administered. By using a low b-value diffusion gradient, the fluid dynamics within the perivascular spaces can be measured. Moreover, by incorporating the phase part of the MRI signal, the vasculature pathways can be mapped, and hence the perivascular routes can be identified. Finally, by using a high b-value diffusion gradient, the dynamics of CSF due to diffusion can be measured. However, several limitations need to be addressed. First, in order to have a reliable estimate of fluid dynamics, the diffusion gradient should be applied in the direction of CSF flow. Due to the intricate network of vasculature in the brain, diffusion gradients in several directions are required to examine the CSF flow in the perivascular spaces of the whole brain. Moreover, for better modeling of fast and slow diffusion along with the convective flow, encoding diffusions with several b-values (from 0 to 1000 s/mm^2) are required. Next, since the perivascular spaces are thin, less than 2 mm [346], a high-resolution MRI system is needed. Therefore, a high-resolution diffusion MRI with multiple b-values is needed which likely necessitates long scanning times. Importantly, prior knowledge of the blood flow velocity and directionality is required in order to map the vasculature utilizing the phase component of the diffusion signal. The DTI-ALPS technique is a very promising tool to detect glymphatic system alterations in neurological diseases, indirectly. Recently, this technique has been widely used due to the ease of

acquiring the DTI data using a clinical MRI setting. However, this technique is limited to the analysis of a specific brain region, i.e., the white matter outside of the lateral ventricular body and it only measures diffusion, not the glymphatic flow.

Overall, the investigation of the glymphatic system in the human brain is in its early stages and warrants further scientific progress. Recent clinical reports incorporating diffusion MRI have shown promising results for measuring glymphatic fluid transport in clinical settings. However, optimization and validation with improved modeling are needed.

CHAPTER SEVEN

SUMMARY AND FUTURE DIRECTIONS

In this dissertation, we have presented important investigations related to the glymphatic system, PVMs, and mLVs. First, we addressed the debate regarding glymphatic convective bulk flow in the interstitial spaces of the brain parenchyma. We further investigated the PVMs for their association with the glymphatic system for CWC in rats. Second, we investigated the response of glymphatic system pathway and perineural pathway along the optic nerves to GBM in rats. Third, we evaluated the mLVs as a possible efflux pathway of the glymphatic system external to the brain parenchyma in transgenic rats.

In the first project (Chapter- 3), we found that in the striatum and the corpus callosum, the pseudo-ADC (ADC*) calculated from T1WI was 70% and 30% larger, respectively, than the ADC estimated from DTI, demonstrating the presence of both convective bulk flow and diffusion in the interstitial spaces of the brain. Confocal imaging revealed the tracer uptake by PVMs, indicating the interaction of PVMs with the glymphatic CSF influx along the arteries and glymphatic CSF efflux along the veins. Our findings solidified the glymphatic system hypothesis for the clearance of interstitial waste solutes from the brain parenchyma. Furthermore, our data suggested that PVMs play an important function in glymphatic system-mediated CWC. The glymphatic system and PVMs could be targeted to enhance CWC in patients with waste-associated neurological conditions and aging. A better understanding of the association between these pathways may lead to new therapeutic strategies for numerous neurological conditions.

In the second project (Chapter- 4), 3D dynamic T1WI data identified reduced glymphatic influx and clearance, indicating an impaired glymphatic system due to GBM. Kinetic modeling and quantitative analyses consistently indicated significantly reduced infusion rate, clearance rate, and increased residual of CSF tracer in GBM rats compared to control rats, suggesting restricted glymphatic flow in the brain with GBM. Our results also demonstrated reduced CSF tracer intensity in the perineural spaces along the optic nerves in GBM rats, indicating compromised CSF tracer efflux via this pathway. Reduced glymphatic clearance may lead to the accumulation of toxic waste solutes and pro-inflammatory signaling molecules which may affect the progression of the GBM. While the precise association between the glymphatic system and GBM cell infiltration is unknown, the glymphatic system convective flux could play an important role in tumor cell migration. The highly invasive nature of GBM cells is a primary reason for the failure of conventional treatment methods. On the other hand, utilizing the brain-wide system of perivascular spaces and enhancing the glymphatic activity by increasing plasma osmolality and lowering the ICP may augment the delivery of anti-tumor drugs to the patients. Thus, a better understanding of the functioning of the glymphatic system with GBM may have important implications for both the progression and treatment of GBM. Future research on utilizing the glymphatic pathway as a means to enhance drug delivery in GBM patients warrants investigation.

Finally, in the third project (Chapter 5), confocal microscopy images revealed the absence of the CSF tracer (QD655) in both the dorsal and basal mLVs of Prox-1 $EGFP^{+}$ rats at 15 mins, 30 mins, 40 mins, and 2 hours after the ICM infusion. Our results suggest that mLVs are not the major efflux pathway for the glymphatic system, which is a

negative result. We did not continue this study as planned in the DM rats to evaluate the effect of this condition on CWC through the mLVs and the glymphatic system. Our study suggests further need of re-evaluation of this pathway as a potential efflux pathway of the glymphatic system.

We also discussed clinical translational issues of the MRI methods for glymphatic related measurements (Chapter 6). MRI based clinical research of the glymphatic system is still in its early stages and warrants further scientific progress. Currently, using gadolinium-based MRI contrast agents is the most accurate approach to measure CSF dynamics associated with this system. The limitations of this method are the multiple measurements at different time points during the monitoring period (up to 72 hours) of the patients and the need to invasively inject (intrathecal) MRI contrast agent. On the other hand, techniques like Diffusion-weighted MRI and PC-MRI are promising to detect CSF dynamics in ventricles, and in perivascular and interstitial spaces without a need for a contrast agent administration in clinical settings. However, optimization and validation of these approaches with improved modeling are needed.

Overall, this dissertation discusses critical pathways for the removal of CSF/ISF and interstitial waste products from within and external to the brain parenchyma. It is a difficult task to classify these pathways by level of importance, as the scientific community remains unsure of the relative contribution of each of these pathways to the overall process of CWC. It may very well be that all these pathways must work in concert to ensure the effective and proper removal of toxic waste products from the brain and ensure healthy neuronal functioning. Maintaining healthy sleep patterns and daily physical exercise may improve the protein waste evacuation, perivascular fluid

circulation, ISF-CSF exchange and cognitive functioning with aging [46, 99]. Further investigations are needed to synchronously assess the full picture of CWC. Specifically, further investigations should include: 1) developing imaging methodologies and sophisticated modeling techniques which can reliably measure and evaluate CWC in patients; 2) investigating other mechanisms related to CWC, such as the function of PVMs; 3) investigating the relationship between CWC and different neurological diseases; 4) discovering therapeutic targets to improve CWC and their clinical translation to patients; 5) systematically investigating the glymphatic system efflux pathways in humans; 6) reexamination of the arachnoid villi/granulations for their possible role in CSF outflow; and 7) in vivo reexamination of the nasal lymphatic pathway via the cribriform plate in the humans.

APPENDIX A

COPYRIGHT LETTERS OF PERMISSION TO REPRODUCE

Permission to reproduce Chapter 2 (Sections 2.1-2.4 and Figure 2.1) in its entirety.

frontiers in Neuroanatomy

Front Neuroanat. 2021; 15: 665803.
Published online 2021 Jul 7. doi: 10.3389/fnana.2021.665803

PMCID: PMC8292771
PMID: 34305538

Waste Clearance in the Brain

Jasleen Kaur,[1,2,†] Lara M. Fahmy,[1,3,†] Esmaeil Davoodi-Bojd,[1,4] Li Zhang,[1] Guangliang Ding,[1] Jiani Hu,[5] Zhenggang Zhang,[1,6] Michael Chopp,[1,2] and Quan Jiang[1,2,6,*]

▸ Author information ▸ Article notes ▾ Copyright and License information PMC Disclaimer

Permission to reproduce Chapter 2 (Section 2.5) in its entirety.

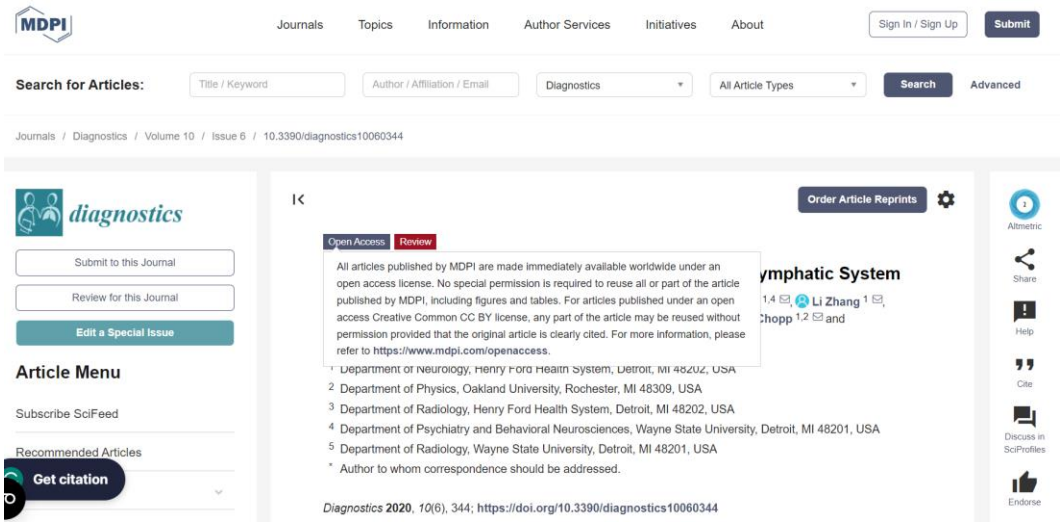

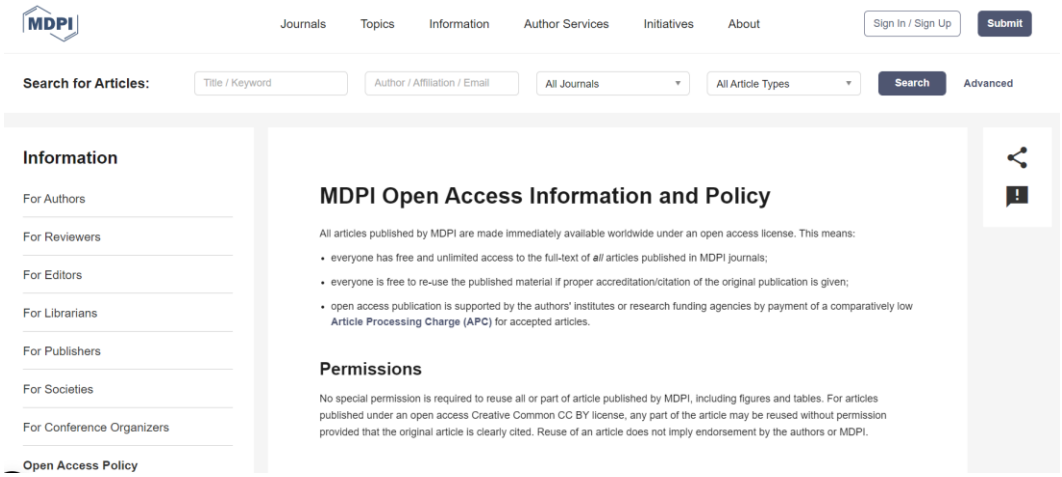

Permission to reproduce Chapter 4 in its entirety.

Research article | Open access | Published: 30 October 2023

Imaging glymphatic response to glioblastoma

Jasleen Kaur, Guangliang Ding, Li Zhang, Yong Lu, Hao Luo, Lian Li, Edward Boyd, Qingjiang Li, Min Wei, Zhenggang Zhang, Michael Chopp & Quan Jiang

Cancer Imaging **23**, Article number: 107 (2023) | Cite this article

Metrics

Abstract

Background

The glymphatic system actively exchanges cerebrospinal fluid (CSF) and interstitial fluid (ISF) to eliminate toxic interstitial waste solutes from the brain parenchyma. Impairment of the glymphatic system has been linked to several neurological conditions. Glioblastoma, also known as Glioblastoma multiforme (GBM) is a highly aggressive form of malignant brain cancer within the glioma category. However, the impact of GBM on the functioning of the glymphatic system has not been investigated. Using dynamic contrast-enhanced magnetic resonance imaging (CE-MRI) and advanced kinetic modeling, we examined the changes in the glymphatic system in rats with GBM.

Imaging glymphatic response to glioblastoma

Rights and permissions

APPENDIX B

RESEARCH ACTIVITY APPROVAL FOR ANIMAL SUBJECTS

Institutional Animal Care and Use Committee
Amendment to Approved Protocol

Please submit one copy containing an original signature to the Research Administration office and email an electronic copy to IACUC@hfhs.org.

PROJECT TITLE: GLYMPHATIC AND COGNITIVE IMPAIRMENT OF AGING AND DIABETES

IACUC No.: 1583

PRINCIPAL INVESTIGATOR: Quan Jiang

DEPT: Neurology **TELEPHONE:** 313-916-8735 **EMAIL:** qjiang1@hfhs.org

HOW SHOULD THE APPROVED AMENDMENT BE RETURNED?:
☐ Interoffice mail – specify location to mail it to:
☒ Email contact person for pick up from IACUC Office
Name of contact person if different from PI:

I am requesting a change regarding the following criteria:

Check all that apply	Complete section(s)
☒ Addition/deletion of research staff[1]	1
☐ Housing requirements[1]	2
☐ Type of caging[1]	3
☐ Cage population density[1]	4
☐ Protocol title[2]	5
☐ Change in funding source[2]	6
☐ Change in Principal Investigator	7
☐ Methodology	8
☐ Restraint system	9
☐ Anesthetic/analgesic regimen	10

Check all that apply	Complete section(s)
☐ Postoperative care	11
☐ Euthanasia and second assurance of death	12
☐ Diet/food, water restriction	13
☐ Increase in animal numbers	14
☐ Location of animal procedures[1]	15
☐ Strain[1]	16
☐ Hazardous agents	17
☐ Non-hazardous agents	18
☐ Other	19

[1]May be administratively approved by the Veterinarian
[2]May be administratively approved by the IACUC Coordinator

Signature is to be handwritten. Signature stamps are not acceptable.
The information provided in this form accurately represents the changes proposed regarding my previously approved IACUC application. I assure that the certifications that I agreed to in the original application in Attachment 1 will remain in effect.

Quan Jiang
Signature of Principal Investigator

5/30/18
Date

IACUC USE ONLY:

Date stamp-received:

IACUC APPROVAL STAMP

Signature of IACUC Chair or Designate

IACUC Amendment Revised 9/25/2015

1. Addition/deletion of research staff
   a. Please explain why the change is necessary.
      One Ph.D. student from Oakland University will join into this study.

   b. Name of new staff person: Jasleen Kaur

   c. Person's responsibility: MRI studies and tail vein injection of MRI contrast agent.

   d. Is the person enrolled in the Occupational Health and Safety Program?
      ☒ Yes Date of last occupational health evaluation (OHE): 05/24/2018
      ☐ No Reason why person is not enrolled:

   e. Is a *User Qualification Form* on file with Bioresources?
      ☐ Yes
      If a *User Qualification Form* is not already on file, one must be completed and submitted with the amendment. The User form is available on the IACUC website: http://henry.hfhs.org/body.cfm?id=7756.

   f. Date of IACUC online in-service completion: 05/24/2018
      The IACUC in-service is available through CITI program. The "Working with the IACUC" course must be completed along with the species specific module for the animal that will be used. Instructions for accessing the course can be found on the IACUC website: http://henry.hfhs.org/body.cfm?id=16038.

2. Change in housing requirements
   a. Please explain why the change is necessary.

   b. Describe the change.

3. Change in type of caging
   a. Please explain why the change is necessary.

4. Change in cage density population greater than Guide requirements
   a. Please explain why the change is necessary and what accommodation(s) will be made for their care.

5. Change in protocol title or additional protocol title:
   a. Explain why the change is necessary.

   b. New title to replace title stated at the top of this amendment:

   c. Additional title requested:

REFERENCES

1. Arbel-Ornath, M., et al., *Interstitial fluid drainage is impaired in ischemic stroke and Alzheimer's disease mouse models.* Acta Neuropathol, 2013. **126**(3): p. 353-64.
2. Goodman, J.R., et al., *Characterization of dural sinus-associated lymphatic vasculature in human Alzheimer's dementia subjects.* Brain Behav Immun, 2018. **73**: p. 34-40.
3. Hinson, H.E., D. Stein, and K.N. Sheth, *Hypertonic saline and mannitol therapy in critical care neurology.* J Intensive Care Med, 2013. **28**(1): p. 3-11.
4. Kyrtsos, C.R. and J.S. Baras, *Modeling the Role of the Glymphatic Pathway and Cerebral Blood Vessel Properties in Alzheimer's Disease Pathogenesis.* PLoS One, 2015. **10**(10): p. e0139574.
5. Peng, W., et al., *Suppression of glymphatic fluid transport in a mouse model of Alzheimer's disease.* Neurobiol Dis, 2016. **93**: p. 215-25.
6. Reeves, B.C., et al., *Glymphatic System Impairment in Alzheimer's Disease and Idiopathic Normal Pressure Hydrocephalus.* Trends Mol Med, 2020. **26**(3): p. 285-295.
7. Tarasoff-Conway, J.M., et al., *Clearance systems in the brain-implications for Alzheimer disease.* Nat Rev Neurol, 2015. **11**(8): p. 457-70.
8. Xia, M., et al., *Mechanism of depression as a risk factor in the development of Alzheimer's disease: the function of AQP4 and the glymphatic system.* Psychopharmacology (Berl), 2017. **234**(3): p. 365-379.
9. Berrouschot, J., et al., *Mortality of space-occupying ('malignant') middle cerebral artery infarction under conservative intensive care.* Intensive Care Med, 1998. **24**(6): p. 620-3.
10. Iliff, J.J., et al., *Impairment of glymphatic pathway function promotes tau pathology after traumatic brain injury.* J Neurosci, 2014. **34**(49): p. 16180-93.
11. Plog, B.A., et al., *Biomarkers of traumatic injury are transported from brain to blood via the glymphatic system.* J Neurosci, 2015. **35**(2): p. 518-26.
12. Tsitsopoulos, P.P. and N. Marklund, *Amyloid-beta Peptides and Tau Protein as Biomarkers in Cerebrospinal and Interstitial Fluid Following Traumatic Brain Injury: A Review of Experimental and Clinical Studies.* Front Neurol, 2013. **4**: p. 79.
13. Zhao, Z., et al., *Establishment and Dysfunction of the Blood-Brain Barrier.* Cell, 2015. **163**(5): p. 1064-1078.
14. Hladky, S.B. and M.A. Barrand, *Fluid and ion transfer across the blood–brain and blood–cerebrospinal fluid barriers; a comparative account of mechanisms and roles.* Fluids and Barriers of the CNS, 2016. **13**(1): p. 19.
15. Harris, K.D., M. Weiss, and A. Zahavi, *Why are neurotransmitters neurotoxic? An evolutionary perspective.* F1000Res, 2014. **3**: p. 179.
16. Cserr, H.F. and L.H. Ostrach, *Bulk flow of interstitial fluid after intracranial injection of blue dextran 2000.* Exp Neurol, 1974. **45**(1): p. 50-60.

17. Iliff, J.J., et al., *A paravascular pathway facilitates CSF flow through the brain parenchyma and the clearance of interstitial solutes, including amyloid beta.* Sci Transl Med, 2012. **4**(147): p. 147ra111.
18. Rangroo Thrane, V., et al., *Paravascular microcirculation facilitates rapid lipid transport and astrocyte signaling in the brain.* Sci Rep, 2013. **3**: p. 2582.
19. Mestre, H., et al., *Flow of cerebrospinal fluid is driven by arterial pulsations and is reduced in hypertension.* Nat Commun, 2018. **9**(1): p. 4878.
20. Jiang, Q., et al., *Impairment of the glymphatic system after diabetes.* J Cereb Blood Flow Metab, 2017. **37**(4): p. 1326-1337.
21. Louveau, A., S. Da Mesquita, and J. Kipnis, *Lymphatics in Neurological Disorders: A Neuro-Lympho-Vascular Component of Multiple Sclerosis and Alzheimer's Disease?* Neuron, 2016. **91**(5): p. 957-73.
22. Jessen, N.A., et al., *The Glymphatic System: A Beginner's Guide.* Neurochem Res, 2015. **40**(12): p. 2583-99.
23. Mestre, H., et al., *Cerebrospinal fluid influx drives acute ischemic tissue swelling.* Science, 2020. **367**(6483).
24. Jin, B.J., A.J. Smith, and A.S. Verkman, *Spatial model of convective solute transport in brain extracellular space does not support a "glymphatic" mechanism.* J Gen Physiol, 2016. **148**(6): p. 489-501.
25. Pizzo, M.E., et al., *Intrathecal antibody distribution in the rat brain: surface diffusion, perivascular transport and osmotic enhancement of delivery.* J Physiol, 2018. **596**(3): p. 445-475.
26. Smith, A.J. and A.S. Verkman, *The "glymphatic" mechanism for solute clearance in Alzheimer's disease: game changer or unproven speculation?* FASEB J, 2018. **32**(2): p. 543-551.
27. Smith, A.J., et al., *Test of the 'glymphatic' hypothesis demonstrates diffusive and aquaporin-4-independent solute transport in rodent brain parenchyma.* Elife, 2017. **6**.
28. Aspelund, A., et al., *A dural lymphatic vascular system that drains brain interstitial fluid and macromolecules.* J Exp Med, 2015. **212**(7): p. 991-9.
29. Louveau, A., et al., *Structural and functional features of central nervous system lymphatic vessels.* Nature, 2015. **523**(7560): p. 337-41.
30. Lukić, I.K., et al., *Virtual dissection: a lesson from the 18th century.* The Lancet, 2003. **362**(9401): p. 2110-2113.
31. Bucchieri, F., et al., *Lymphatic vessels of the dura mater: a new discovery?* J Anat, 2015. **227**(5): p. 702-3.
32. Da Mesquita, S., Z. Fu, and J. Kipnis, *The Meningeal Lymphatic System: A New Player in Neurophysiology.* Neuron, 2018. **100**(2): p. 375-388.
33. Kaur, J., et al., *Waste Clearance in the Brain.* Frontiers in Neuroanatomy, 2021. **15**.
34. Kaur, J., et al., *Magnetic Resonance Imaging and Modeling of the Glymphatic System.* Diagnostics (Basel), 2020. **10**(6).
35. Kaur, J., et al., *Imaging glymphatic response to glioblastoma.* Cancer Imaging, 2023. **23**(1): p. 107.

36. Khasawneh, A.H., R.J. Garling, and C.A. Harris, *Cerebrospinal fluid circulation: What do we know and how do we know it?* Brain Circ, 2018. **4**(1): p. 14-18.
37. Craven, J., *Cerebrospinal fluid and its circulation.* Anaesthesia & Intensive Care Medicine, 2010. **11**(9): p. 355-356.
38. Brinker, T., et al., *A new look at cerebrospinal fluid circulation.* Fluids and Barriers of the CNS, 2014. **11**(1): p. 10.
39. Johanson, C.E., et al., *Multiplicity of cerebrospinal fluid functions: New challenges in health and disease.* Cerebrospinal Fluid Res, 2008. **5**: p. 10.
40. Matsumae, M., et al., *Changing the Currently Held Concept of Cerebrospinal Fluid Dynamics Based on Shared Findings of Cerebrospinal Fluid Motion in the Cranial Cavity Using Various Types of Magnetic Resonance Imaging Techniques.* Neurol Med Chir (Tokyo), 2019. **59**(4): p. 133-146.
41. Petitclerc, L., et al., *Ultra-long-TE arterial spin labeling reveals rapid and brain-wide blood-to-CSF water transport in humans.* Neuroimage, 2021. **245**: p. 118755.
42. Brinker, T., et al., *A new look at cerebrospinal fluid circulation.* Fluids Barriers CNS, 2014. **11**(1): p. 10.
43. Hladky, S.B. and M.A. Barrand, *Mechanisms of fluid movement into, through and out of the brain: evaluation of the evidence.* Fluids Barriers CNS, 2014. **11**(1): p. 26.
44. Lehtinen, M.K., et al., *The choroid plexus and cerebrospinal fluid: emerging roles in development, disease, and therapy.* J Neurosci, 2013. **33**(45): p. 17553-9.
45. Nilsson, C., et al., *Circadian variation in human cerebrospinal fluid production measured by magnetic resonance imaging.* Am J Physiol, 1992. **262**(1 Pt 2): p. R20-4.
46. Abbott, N.J., et al., *The role of brain barriers in fluid movement in the CNS: is there a 'glymphatic' system?* Acta Neuropathol, 2018. **135**(3): p. 387-407.
47. Egnor, M., et al., *A model of pulsations in communicating hydrocephalus.* Pediatr Neurosurg, 2002. **36**(6): p. 281-303.
48. Howell, M.D. and P.E. Gottschall, *Lectican proteoglycans, their cleaving metalloproteinases, and plasticity in the central nervous system extracellular microenvironment.* Neuroscience, 2012. **217**: p. 6-18.
49. Lei, Y., et al., *The brain interstitial system: Anatomy, modeling, in vivo measurement, and applications.* Prog Neurobiol, 2017. **157**: p. 230-246.
50. Shetty, A.K. and G. Zanirati, *The Interstitial System of the Brain in Health and Disease.* Aging Dis, 2020. **11**(1): p. 200-211.
51. Abbott, N.J., *Evidence for bulk flow of brain interstitial fluid: significance for physiology and pathology.* Neurochemistry International, 2004. **45**(4): p. 545-552.
52. Laterra J, K.R., Betz LA, et al. *Basic Neurochemistry: Molecular, Cellular and Medical Aspects.* 1999 05/05/2021]; 6th edition:[Available from: https://www.ncbi.nlm.nih.gov/books/NBK27998/.
53. MJ, C. *The Cerebral Circulation*. 2009 05/03/2021]; Available from: https://www.ncbi.nlm.nih.gov/books/NBK53084/.
54. Nedergaard, M., *Neuroscience. Garbage truck of the brain.* Science, 2013. **340**(6140): p. 1529-30.

55. Wolfe, M.S., *The Role of Tau in Neurodegenerative Diseases and Its Potential as a Therapeutic Target.* Scientifica, 2012. **2012**: p. 796024.
56. Hartl, F.U., A. Bracher, and M. Hayer-Hartl, *Molecular chaperones in protein folding and proteostasis.* Nature, 2011. **475**(7356): p. 324-332.
57. Powers, E.T., et al., *Biological and Chemical Approaches to Diseases of Proteostasis Deficiency.* Annual Review of Biochemistry, 2009. **78**(1): p. 959-991.
58. Da Mesquita, S., et al., *Functional aspects of meningeal lymphatics in ageing and Alzheimer's disease.* Nature, 2018. **560**(7717): p. 185-191.
59. Haass, C., et al., *Trafficking and proteolytic processing of APP.* Cold Spring Harb Perspect Med, 2012. **2**(5): p. a006270.
60. Murphy, M.P. and H. LeVine, 3rd, *Alzheimer's disease and the amyloid-beta peptide.* J Alzheimers Dis, 2010. **19**(1): p. 311-23.
61. LaFerla, F.M., K.N. Green, and S. Oddo, *Intracellular amyloid-β in Alzheimer's disease.* Nature Reviews Neuroscience, 2007. **8**(7): p. 499-509.
62. Yamada, K., et al., *Neuronal activity regulates extracellular tau in vivo.* J Exp Med, 2014. **211**(3): p. 387-93.
63. Mandelkow, E.M. and E. Mandelkow, *Biochemistry and cell biology of tau protein in neurofibrillary degeneration.* Cold Spring Harb Perspect Med, 2012. **2**(7): p. a006247.
64. Gong, C.X. and K. Iqbal, *Hyperphosphorylation of microtubule-associated protein tau: a promising therapeutic target for Alzheimer disease.* Curr Med Chem, 2008. **15**(23): p. 2321-8.
65. Busche, M.A. and B.T. Hyman, *Synergy between amyloid-beta and tau in Alzheimer's disease.* Nat Neurosci, 2020. **23**(10): p. 1183-1193.
66. Pirscoveanu, D.F.V., et al., *Tau protein in neurodegenerative diseases - a review.* Rom J Morphol Embryol, 2017. **58**(4): p. 1141-1150.
67. Edwards, G., 3rd, et al., *Traumatic Brain Injury Induces Tau Aggregation and Spreading.* J Neurotrauma, 2020. **37**(1): p. 80-92.
68. Frost, B. and M.I. Diamond, *Prion-like mechanisms in neurodegenerative diseases.* Nat Rev Neurosci, 2010. **11**(3): p. 155-9.
69. Jucker, M. and L.C. Walker, *Pathogenic protein seeding in Alzheimer disease and other neurodegenerative disorders.* Ann Neurol, 2011. **70**(4): p. 532-40.
70. Bell, R.D., et al., *Transport pathways for clearance of human Alzheimer's amyloid beta-peptide and apolipoproteins E and J in the mouse central nervous system.* J Cereb Blood Flow Metab, 2007. **27**(5): p. 909-18.
71. Qosa, H., et al., *Differences in amyloid-beta clearance across mouse and human blood-brain barrier models: kinetic analysis and mechanistic modeling.* Neuropharmacology, 2014. **79**: p. 668-78.
72. Shibata, M., et al., *Clearance of Alzheimer's amyloid-ss(1-40) peptide from brain by LDL receptor-related protein-1 at the blood-brain barrier.* J Clin Invest, 2000. **106**(12): p. 1489-99.
73. Duffy, K.R. and W.M. Pardridge, *Blood-brain barrier transcytosis of insulin in developing rabbits.* Brain Res, 1987. **420**(1): p. 32-8.

74. Banks, W.A., et al., *Studies of the slow bidirectional transport of iron and transferrin across the blood-brain barrier.* Brain Research Bulletin, 1988. **21**(6): p. 881-885.
75. Hladky, S.B. and M.A. Barrand, *Elimination of substances from the brain parenchyma: efflux via perivascular pathways and via the blood-brain barrier.* Fluids Barriers CNS, 2018. **15**(1): p. 30.
76. Carare, R.O., et al., *Solutes, but not cells, drain from the brain parenchyma along basement membranes of capillaries and arteries: significance for cerebral amyloid angiopathy and neuroimmunology.* Neuropathol Appl Neurobiol, 2008. **34**(2): p. 131-44.
77. Albargothy, N.J., et al., *Convective influx/glymphatic system: tracers injected into the CSF enter and leave the brain along separate periarterial basement membrane pathways.* Acta Neuropathol, 2018. **136**(1): p. 139-152.
78. Diem, A.K., et al., *Arterial Pulsations cannot Drive Intramural Periarterial Drainage: Significance for Aβ Drainage.* 2017. **11**(475).
79. Aldea, R., et al., *Cerebrovascular Smooth Muscle Cells as the Drivers of Intramural Periarterial Drainage of the Brain.* 2019. **11**(1).
80. Iliff, J.J., et al., *Brain-wide pathway for waste clearance captured by contrast-enhanced MRI.* J Clin Invest, 2013. **123**(3): p. 1299-309.
81. Xie, L., et al., *Sleep drives metabolite clearance from the adult brain.* Science, 2013. **342**(6156): p. 373-7.
82. Benveniste, H., H. Lee, and N.D. Volkow, *The Glymphatic Pathway: Waste Removal from the CNS via Cerebrospinal Fluid Transport.* Neuroscientist, 2017. **23**(5): p. 454-465.
83. Nedergaard, M. and S.A. Goldman, *Brain Drain.* Sci Am, 2016. **314**(3): p. 44-9.
84. Mestre, H., et al., *Aquaporin-4-dependent glymphatic solute transport in the rodent brain.* Elife, 2018. **7**.
85. Iliff, J.J., et al., *Cerebral arterial pulsation drives paravascular CSF-interstitial fluid exchange in the murine brain.* J Neurosci, 2013. **33**(46): p. 18190-9.
86. Ueno, M., et al., *Blood-brain barrier and blood-cerebrospinal fluid barrier in normal and pathological conditions.* Brain Tumor Pathol, 2016. **33**(2): p. 89-96.
87. Hu, J., et al. *Does the vascular system complement the glymphatic system?* . in *International Conference on Medical Imaging and Engineering*. 2019. Shenzhen, China.
88. Jiang, Q., et al. *Interaction of vascular and glymphatic systems in brain waste clearance after diabetes.* in *Proceedings of the International Society for Magnetic Resonance in Medicine*. 2018. Paris, France.
89. Louveau, A., et al., *Understanding the functions and relationships of the glymphatic system and meningeal lymphatics.* J Clin Invest, 2017. **127**(9): p. 3210-3219.
90. Lee, H., et al., *The Effect of Body Posture on Brain Glymphatic Transport.* J Neurosci, 2015. **35**(31): p. 11034-44.
91. Chen, R.L., et al., *Age-related changes in choroid plexus and blood-cerebrospinal fluid barrier function in the sheep.* Exp Gerontol, 2009. **44**(4): p. 289-96.

92. Fleischman, D., et al., *Cerebrospinal fluid pressure decreases with older age.* PLoS One, 2012. **7**(12): p. e52664.
93. Kress, B.T., et al., *Impairment of paravascular clearance pathways in the aging brain.* Ann Neurol, 2014. **76**(6): p. 845-61.
94. Zieman, S.J., V. Melenovsky, and D.A. Kass, *Mechanisms, pathophysiology, and therapy of arterial stiffness.* Arterioscler Thromb Vasc Biol, 2005. **25**(5): p. 932-43.
95. Zhou, Y., et al., *Impairment of glymphatic pathway and putative meningeal lymphatic vessels in aging human.* Annals of Neurology, 2020. **87**.
96. Benveniste, H., et al., *Anesthesia with Dexmedetomidine and Low-dose Isoflurane Increases Solute Transport via the Glymphatic Pathway in Rat Brain When Compared with High-dose Isoflurane.* Anesthesiology, 2017. **127**(6): p. 976-988.
97. Simon, M.J. and J.J. Iliff, *Regulation of cerebrospinal fluid (CSF) flow in neurodegenerative, neurovascular and neuroinflammatory disease.* Biochim Biophys Acta, 2016. **1862**(3): p. 442-51.
98. Ju, Y.E., et al., *Obstructive sleep apnea decreases central nervous system-derived proteins in the cerebrospinal fluid.* Ann Neurol, 2016. **80**(1): p. 154-9.
99. He, X.F., et al., *Voluntary Exercise Promotes Glymphatic Clearance of Amyloid Beta and Reduces the Activation of Astrocytes and Microglia in Aged Mice.* Front Mol Neurosci, 2017. **10**: p. 144.
100. Ren, H., et al., *Omega-3 polyunsaturated fatty acids promote amyloid-beta clearance from the brain through mediating the function of the glymphatic system.* FASEB J, 2017. **31**(1): p. 282-293.
101. Zarow, C., et al., *Neuronal loss is greater in the locus coeruleus than nucleus basalis and substantia nigra in Alzheimer and Parkinson diseases.* Arch Neurol, 2003. **60**(3): p. 337-41.
102. Mondello, S., et al., *Blood-based diagnostics of traumatic brain injuries.* Expert Rev Mol Diagn, 2011. **11**(1): p. 65-78.
103. Magnoni, S., et al., *Tau elevations in the brain extracellular space correlate with reduced amyloid-beta levels and predict adverse clinical outcomes after severe traumatic brain injury.* Brain, 2012. **135**(Pt 4): p. 1268-80.
104. Morris, M., et al., *The many faces of tau.* Neuron, 2011. **70**(3): p. 410-26.
105. Mestre, H., et al., *Perivascular spaces, glymphatic dysfunction, and small vessel disease.* Clin Sci (Lond), 2017. **131**(17): p. 2257-2274.
106. Charidimou, A., L. Pantoni, and S. Love, *The concept of sporadic cerebral small vessel disease: A road map on key definitions and current concepts.* Int J Stroke, 2016. **11**(1): p. 6-18.
107. Gaberel, T., et al., *Impaired glymphatic perfusion after strokes revealed by contrast-enhanced MRI: a new target for fibrinolysis?* Stroke, 2014. **45**(10): p. 3092-6.
108. Goulay, R., et al., *Subarachnoid Hemorrhage Severely Impairs Brain Parenchymal Cerebrospinal Fluid Circulation in Nonhuman Primate.* Stroke, 2017. **48**(8): p. 2301-2305.
109. Mestre, H., et al., *Cerebrospinal fluid influx drives acute ischemic tissue swelling.* 2020. **367**(6483): p. eaax7171.

110. Venkat, P., et al., *White matter damage and glymphatic dysfunction in a model of vascular dementia in rats with no prior vascular pathologies.* Neurobiol Aging, 2017. **50**: p. 96-106.
111. Wang, M., et al., *Focal Solute Trapping and Global Glymphatic Pathway Impairment in a Murine Model of Multiple Microinfarcts.* J Neurosci, 2017. **37**(11): p. 2870-2877.
112. Schain, A.J., et al., *Cortical Spreading Depression Closes Paravascular Space and Impairs Glymphatic Flow: Implications for Migraine Headache.* The Journal of Neuroscience, 2017. **37**(11): p. 2904.
113. Wostyn, P., H.E. Killer, and P.P. De Deyn, *Glymphatic stasis at the site of the lamina cribrosa as a potential mechanism underlying open-angle glaucoma.* Clin Exp Ophthalmol, 2017. **45**(5): p. 539-547.
114. Rosenberg, G.A., W.T. Kyner, and E. Estrada, *Bulk flow of brain interstitial fluid under normal and hyperosmolar conditions.* Am J Physiol, 1980. **238**(1): p. F42-9.
115. Cserr, H.F., D.N. Cooper, and T.H. Milhorat, *Flow of cerebral interstitial fluid as indicated by the removal of extracellular markers from rat caudate nucleus.* Exp Eye Res, 1977. **25 Suppl**: p. 461-73.
116. Sykova, E. and C. Nicholson, *Diffusion in brain extracellular space.* Physiol Rev, 2008. **88**(4): p. 1277-340.
117. Mabray, M.C., et al., *Direct Cranial Nerve Involvement by Gliomas: Case Series and Review of the Literature.* AJNR Am J Neuroradiol, 2015. **36**(7): p. 1349-54.
118. Krainik A, C.J., *Imaging Evaluation of Patients with Cranial Nerve Disorders.* Springer, 2020: p. Chapter 12.
119. Sweeney, M.D., et al., *Blood-Brain Barrier: From Physiology to Disease and Back.* Physiol Rev, 2019. **99**(1): p. 21-78.
120. Wilhelm, I., et al., *Heterogeneity of the blood-brain barrier.* Tissue Barriers, 2016. **4**(1): p. e1143544.
121. Cordon-Cardo, C., et al., *Multidrug-resistance gene (P-glycoprotein) is expressed by endothelial cells at blood-brain barrier sites.* Proc Natl Acad Sci U S A, 1989. **86**(2): p. 695-8.
122. Sugawara, I., et al., *Specialized localization of P-glycoprotein recognized by MRK 16 monoclonal antibody in endothelial cells of the brain and the spinal cord.* Jpn J Cancer Res, 1990. **81**(8): p. 727-30.
123. Hartz, A.M. and B. Bauer, *ABC transporters in the CNS - an inventory.* Curr Pharm Biotechnol, 2011. **12**(4): p. 656-73.
124. Chaves, C., et al., *Human ABC transporters at blood-CNS interfaces as determinants of CNS drug penetration.* Curr Pharm Des, 2014. **20**(10): p. 1450-62.
125. Qosa, H., et al., *Regulation of ABC efflux transporters at blood-brain barrier in health and neurological disorders.* Brain Res, 2015. **1628**(Pt B): p. 298-316.
126. Tatsuta, T., et al., *Functional involvement of P-glycoprotein in blood-brain barrier.* J Biol Chem, 1992. **267**(28): p. 20383-91.
127. Virgintino, D., et al., *Expression of P-glycoprotein in human cerebral cortex microvessels.* J Histochem Cytochem, 2002. **50**(12): p. 1671-6.

128. Schinkel, A.H., et al., *Disruption of the mouse mdr1a P-glycoprotein gene leads to a deficiency in the blood-brain barrier and to increased sensitivity to drugs.* Cell, 1994. **77**(4): p. 491-502.
129. Geyer, J., O. Gavrilova, and E. Petzinger, *Brain penetration of ivermectin and selamectin in mdr1a,b P-glycoprotein- and bcrp- deficient knockout mice.* J Vet Pharmacol Ther, 2009. **32**(1): p. 87-96.
130. Deane, R., et al., *IgG-assisted age-dependent clearance of Alzheimer's amyloid beta peptide by the blood-brain barrier neonatal Fc receptor.* J Neurosci, 2005. **25**(50): p. 11495-503.
131. Zhang, Y. and W.M. Pardridge, *Mediated efflux of IgG molecules from brain to blood across the blood-brain barrier.* J Neuroimmunol, 2001. **114**(1-2): p. 168-72.
132. Singh, I., *Textbook of human neuroanatomy : (fundamental and clinical)*. 2009, New Delhi: Jaypee Brothers.
133. Weed, L.H., *Studies on Cerebro-Spinal Fluid. No. III : The pathways of escape from the Subarachnoid Spaces with particular reference to the Arachnoid Villi.* J Med Res, 1914. **31**(1): p. 51-91.
134. Pollay, M., *The function and structure of the cerebrospinal fluid outflow system.* Cerebrospinal Fluid Res, 2010. **7**: p. 9.
135. Welch, K. and M. Pollay, *Perfusion of particles through arachnoid villi of the monkey.* Am J Physiol, 1961. **201**: p. 651-4.
136. Ma, Q., et al., *Outflow of cerebrospinal fluid is predominantly through lymphatic vessels and is reduced in aged mice.* Nat Commun, 2017. **8**(1): p. 1434.
137. Krishnamurthy, S., et al., *Normal macromolecular clearance out of the ventricles is delayed in hydrocephalus.* Brain Res, 2018. **1678**: p. 337-355.
138. Kutomi, O. and S. Takeda, *Identification of lymphatic endothelium in cranial arachnoid granulation-like dural gap.* Microscopy (Oxf), 2020. **69**(6): p. 391-400.
139. Johnston, M., et al., *Evidence of connections between cerebrospinal fluid and nasal lymphatic vessels in humans, non-human primates and other mammalian species.* Cerebrospinal Fluid Res, 2004. **1**(1): p. 2.
140. Kida, S., A. Pantazis, and R.O. Weller, *CSF drains directly from the subarachnoid space into nasal lymphatics in the rat. Anatomy, histology and immunological significance.* Neuropathol Appl Neurobiol, 1993. **19**(6): p. 480-8.
141. Nagra, G., et al., *Quantification of cerebrospinal fluid transport across the cribriform plate into lymphatics in rats.* Am J Physiol Regul Integr Comp Physiol, 2006. **291**(5): p. R1383-9.
142. Goldmann, J., et al., *T cells traffic from brain to cervical lymph nodes via the cribroid plate and the nasal mucosa.* J Leukoc Biol, 2006. **80**(4): p. 797-801.
143. Kaminski, M., et al., *Migration of monocytes after intracerebral injection.* Cell Adh Migr, 2012. **6**(3): p. 164-7.
144. Mollanji, R., et al., *Intracranial pressure accommodation is impaired by blocking pathways leading to extracranial lymphatics.* Am J Physiol Regul Integr Comp Physiol, 2001. **280**(5): p. R1573-81.

145. Mollanji, R., et al., *Blocking cerebrospinal fluid absorption through the cribriform plate increases resting intracranial pressure.* Am J Physiol Regul Integr Comp Physiol, 2002. **282**(6): p. R1593-9.
146. Liu, H., et al., *Olfactory route for cerebrospinal fluid drainage into the cervical lymphatic system in a rabbit experimental model.* Neural Regen Res, 2012. **7**(10): p. 766-71.
147. Melin, E., P.K. Eide, and G. Ringstad, *In vivo assessment of cerebrospinal fluid efflux to nasal mucosa in humans.* Scientific Reports, 2020. **10**(1): p. 14974.
148. Brierley, J.B. and E.J. Field, *The connexions of the spinal sub-arachnoid space with the lymphatic system.* J Anat, 1948. **82**(Pt 3): p. 153-66.
149. Zakharov, A., et al., *Lymphatic cerebrospinal fluid absorption pathways in neonatal sheep revealed by subarachnoid injection of Microfil.* Neuropathol Appl Neurobiol, 2003. **29**(6): p. 563-73.
150. Koh, L., A. Zakharov, and M. Johnston, *Integration of the subarachnoid space and lymphatics: is it time to embrace a new concept of cerebrospinal fluid absorption?* Cerebrospinal Fluid Res, 2005. **2**: p. 6.
151. Arnold, W., et al., *Qualitative Untersuchungen der Verbindungswege des Subarachnoidalraumes mit dem Lymphatischen System des Kopfes und des Halses.* Acta Oto-Laryngologica, 1972. **74**(1-6): p. 411-424.
152. Boulton, M., et al., *Drainage of CSF through lymphatic pathways and arachnoid villi in sheep: measurement of 125I-albumin clearance.* Neuropathol Appl Neurobiol, 1996. **22**(4): p. 325-33.
153. Fahmy, L.M., et al., *All Central Nervous System Neuro- and Vascular-Communication Channels Are Surrounded With Cerebrospinal Fluid.* Front Neurol, 2021. **12**: p. 614636.
154. Benveniste, H., et al., *The Glymphatic System and Waste Clearance with Brain Aging: A Review.* Gerontology, 2019. **65**(2): p. 106-119.
155. Louveau, A., et al., *CNS lymphatic drainage and neuroinflammation are regulated by meningeal lymphatic vasculature.* Nat Neurosci, 2018. **21**(10): p. 1380-1391.
156. Ahn, J.H., et al., *Meningeal lymphatic vessels at the skull base drain cerebrospinal fluid.* Nature, 2019. **572**(7767): p. 62-66.
157. Naganawa, S., et al., *The Space between the Pial Sheath and the Cortical Venous Wall May Connect to the Meningeal Lymphatics.* Magn Reson Med Sci, 2020. **19**(1): p. 1-4.
158. Absinta, M., et al., *Human and nonhuman primate meninges harbor lymphatic vessels that can be visualized noninvasively by MRI.* Elife, 2017. **6**.
159. Zhou, Y., et al., *Impairment of the Glymphatic Pathway and Putative Meningeal Lymphatic Vessels in the Aging Human.* Ann Neurol, 2020. **87**(3): p. 357-369.
160. Hu, X., et al., *Meningeal lymphatic vessels regulate brain tumor drainage and immunity.* Cell Research, 2020. **30**(3): p. 229-243.
161. Eide, P.K., et al., *Magnetic resonance imaging provides evidence of glymphatic drainage from human brain to cervical lymph nodes.* Sci Rep, 2018. **8**(1): p. 7194.

162. Eide, P.K. and G. Ringstad, *Delayed clearance of cerebrospinal fluid tracer from entorhinal cortex in idiopathic normal pressure hydrocephalus: A glymphatic magnetic resonance imaging study.* J Cereb Blood Flow Metab, 2019. **39**(7): p. 1355-1368.
163. Eide, P.K. and G. Ringstad, *In Vivo Imaging of Molecular Clearance From Human Entorhinal Cortex: A Possible Method for Preclinical Testing of Dementia.* Gerontol Geriatr Med, 2019. **5**: p. 2333721419889739.
164. Ringstad, G., et al., *Brain-wide glymphatic enhancement and clearance in humans assessed with MRI.* JCI Insight, 2018. **3**(13).
165. Ringstad, G., S.A.S. Vatnehol, and P.K. Eide, *Glymphatic MRI in idiopathic normal pressure hydrocephalus.* Brain, 2017. **140**(10): p. 2691-2705.
166. Watts, R., et al., *Measuring Glymphatic Flow in Man Using Quantitative Contrast-Enhanced MRI.* AJNR Am J Neuroradiol, 2019. **40**(4): p. 648-651.
167. Eidsvaag, V.A., et al., *Human and mouse cortical astrocytes differ in aquaporin-4 polarization toward microvessels.* Glia, 2017. **65**(6): p. 964-973.
168. Nejad-Davarani, S.P., et al., *An extended vascular model for less biased estimation of permeability parameters in DCE-T1 images.* NMR Biomed, 2017. **30**(6).
169. Nejad-Davarani, S.P., et al., *A parametric model of the brain vascular system for estimation of the arterial input function (AIF) at the tissue level.* NMR Biomed, 2017. **30**(5).
170. Davoodi-Bojd, E., et al., *Modeling glymphatic system of the brain using MRI.* Neuroimage, 2019. **188**: p. 616-627.
171. Ratner, V., et al., *Cerebrospinal and interstitial fluid transport via the glymphatic pathway modeled by optimal mass transport.* Neuroimage, 2017. **152**: p. 530-537.
172. Ratner, V., et al., *Optimal-mass-transfer-based estimation of glymphatic transport in living brain.* Proc SPIE Int Soc Opt Eng, 2015. **9413**.
173. Elkin, R., et al. *Lagrangian Optimal Mass Transport with Applications to the Glymphatic System*. arXiv e-prints, 2019. arXiv:1902.07310.
174. Elkin, R., et al., *GlymphVIS: Visualizing Glymphatic Transport Pathways Using Regularized Optimal Transport.* Med Image Comput Comput Assist Interv, 2018. **11070**: p. 844-852.
175. Elkin, R., et al., *Optimal mass transport kinetic modeling for head and neck DCE-MRI: Initial analysis.* Magn Reson Med, 2019. **82**(6): p. 2314-2325.
176. Kim, J.H., et al., *Voxelized computational model for convection-enhanced delivery in the rat ventral hippocampus: comparison with in vivo MR experimental studies.* Ann Biomed Eng, 2012. **40**(9): p. 2043-58.
177. Kaur, J., et al., *Waste Clearance in the Brain.* Frontiers in Neuroanatomy, 2021. **15**: p. 53.
178. van Veluw, S.J., et al., *Vasomotion as a Driving Force for Paravascular Clearance in the Awake Mouse Brain.* Neuron, 2020. **105**(3): p. 549-561.e5.
179. Drieu, A., et al., *Parenchymal border macrophages regulate the flow dynamics of the cerebrospinal fluid.* Nature, 2022. **611**(7936): p. 585-593.
180. Holstein-Rønsbo, S., et al., *Glymphatic influx and clearance are accelerated by neurovascular coupling.* Nat Neurosci, 2023. **26**(6): p. 1042-1053.

181. Cserr, H.F., et al., *Efflux of radiolabeled polyethylene glycols and albumin from rat brain.* Am J Physiol, 1981. **240**(4): p. F319-28.
182. Rennels, M.L., O.R. Blaumanis, and P.A. Grady, *Rapid solute transport throughout the brain via paravascular fluid pathways.* Adv Neurol, 1990. **52**: p. 431-9.
183. Rennels, M.L., et al., *Evidence for a 'paravascular' fluid circulation in the mammalian central nervous system, provided by the rapid distribution of tracer protein throughout the brain from the subarachnoid space.* Brain Res, 1985. **326**(1): p. 47-63.
184. Ichimura, T., P.A. Fraser, and H.F. Cserr, *Distribution of extracellular tracers in perivascular spaces of the rat brain.* Brain Res, 1991. **545**(1-2): p. 103-13.
185. Holter, K.E., et al., *Interstitial solute transport in 3D reconstructed neuropil occurs by diffusion rather than bulk flow.* Proc Natl Acad Sci U S A, 2017. **114**(37): p. 9894-9899.
186. Levin, V.A., J.D. Fenstermacher, and C.S. Patlak, *Sucrose and inulin space measurements of cerebral cortex in four mammalian species.* Am J Physiol, 1970. **219**(5): p. 1528-33.
187. Rall, D.P., W.W. Oppelt, and C.S. Patlak, *Extracellular space of brain as determined by diffusion of inulin from the ventricular system.* Life Sciences, 1962. **1**(2): p. 43-48.
188. Tao, L. and C. Nicholson, *Diffusion of albumins in rat cortical slices and relevance to volume transmission.* Neuroscience, 1996. **75**(3): p. 839-47.
189. Brightman, M.W., *The brain's interstitial clefts and their glial walls.* J Neurocytol, 2002. **31**(8-9): p. 595-603.
190. Syková, E. and C. Nicholson, *Diffusion in brain extracellular space.* Physiol Rev, 2008. **88**(4): p. 1277-340.
191. Ohata, K. and A. Marmarou, *Clearance of brain edema and macromolecules through the cortical extracellular space.* J Neurosurg, 1992. **77**(3): p. 387-96.
192. Nicholson, C. and E. Syková, *Extracellular space structure revealed by diffusion analysis.* Trends Neurosci, 1998. **21**(5): p. 207-15.
193. Faraco, G., et al., *Brain perivascular macrophages: characterization and functional roles in health and disease.* J Mol Med (Berl), 2017. **95**(11): p. 1143-1152.
194. Herz, J., et al., *Myeloid Cells in the Central Nervous System.* Immunity, 2017. **46**(6): p. 943-956.
195. Prinz, M., D. Erny, and N. Hagemeyer, *Ontogeny and homeostasis of CNS myeloid cells.* Nat Immunol, 2017. **18**(4): p. 385-392.
196. Lapenna, A., M. De Palma, and C.E. Lewis, *Perivascular macrophages in health and disease.* Nat Rev Immunol, 2018. **18**(11): p. 689-702.
197. Van Hove, H., et al., *A single-cell atlas of mouse brain macrophages reveals unique transcriptional identities shaped by ontogeny and tissue environment.* Nature Neuroscience, 2019. **22**(6): p. 1021-1035.
198. Goldmann, T., et al., *Origin, fate and dynamics of macrophages at central nervous system interfaces.* Nature Immunology, 2016. **17**(7): p. 797-805.

199. Hickey, W.F. and H. Kimura, *Perivascular microglial cells of the CNS are bone marrow-derived and present antigen in vivo.* Science, 1988. **239**(4837): p. 290-2.
200. Masuda, T., et al., *Specification of CNS macrophage subsets occurs postnatally in defined niches.* Nature, 2022. **604**(7907): p. 740-748.
201. Da Mesquita, S., et al., *Aging-associated deficit in CCR7 is linked to worsened glymphatic function, cognition, neuroinflammation, and β-amyloid pathology.* Sci Adv, 2021. **7**(21).
202. Willis, C.L., C.J. Garwood, and D.E. Ray, *A size selective vascular barrier in the rat area postrema formed by perivascular macrophages and the extracellular matrix.* Neuroscience, 2007. **150**(2): p. 498-509.
203. Mato, M., S. Ookawara, and K. Kurihara, *Uptake of exogenous substances and marked infoldings of the fluorescent granular pericyte in cerebral fine vessels.* Am J Anat, 1980. **157**(3): p. 329-32.
204. Mato, M., et al., *Involvement of specific macrophage-lineage cells surrounding arterioles in barrier and scavenger function in brain cortex.* Proc Natl Acad Sci U S A, 1996. **93**(8): p. 3269-74.
205. Bechmann, I., et al., *Immune surveillance of mouse brain perivascular spaces by blood-borne macrophages.* Eur J Neurosci, 2001. **14**(10): p. 1651-8.
206. Kida, S., et al., *Perivascular cells act as scavengers in the cerebral perivascular spaces and remain distinct from pericytes, microglia and macrophages.* Acta Neuropathol, 1993. **85**(6): p. 646-52.
207. Møller, M., M.F. Rath, and D.C. Klein, *The perivascular phagocyte of the mouse pineal gland: an antigen-presenting cell.* Chronobiol Int, 2006. **23**(1-2): p. 393-401.
208. Henning, E.C., et al., *Feridex preloading permits tracking of CNS-resident macrophages after transient middle cerebral artery occlusion.* J Cereb Blood Flow Metab, 2009. **29**(7): p. 1229-39.
209. Yang, T., R. Guo, and F. Zhang, *Brain perivascular macrophages: Recent advances and implications in health and diseases.* CNS Neurosci Ther, 2019. **25**(12): p. 1318-1328.
210. Zheng, L., et al., *Perivascular macrophages in the CNS: From health to neurovascular diseases.* CNS Neurosci Ther, 2022. **28**(12): p. 1908-1920.
211. Siret, C., et al., *Deciphering the heterogeneity of the Lyve1+ perivascular macrophages in the mouse brain.* Nature Communications, 2022. **13**(1): p. 7366.
212. Hawkes, C.A. and J. McLaurin, *Selective targeting of perivascular macrophages for clearance of beta-amyloid in cerebral amyloid angiopathy.* Proc Natl Acad Sci U S A, 2009. **106**(4): p. 1261-6.
213. Thanopoulou, K., et al., *Scavenger receptor class B type I (SR-BI) regulates perivascular macrophages and modifies amyloid pathology in an Alzheimer mouse model.* Proc Natl Acad Sci U S A, 2010. **107**(48): p. 20816-21.
214. Park, L., et al., *Brain Perivascular Macrophages Initiate the Neurovascular Dysfunction of Alzheimer Aβ Peptides.* Circ Res, 2017. **121**(3): p. 258-269.
215. Drieu, A., et al., *Alcohol exposure-induced neurovascular inflammatory priming impacts ischemic stroke and is linked with brain perivascular macrophages.* JCI Insight, 2020. **5**(4).

216. Pedragosa, J., et al., *CNS-border associated macrophages respond to acute ischemic stroke attracting granulocytes and promoting vascular leakage.* Acta Neuropathologica Communications, 2018. **6**(1): p. 76.
217. Zhang, Z., et al., *Parenchymal accumulation of CD163+ macrophages/microglia in multiple sclerosis brains.* J Neuroimmunol, 2011. **237**(1-2): p. 73-9.
218. Polfliet, M.M.J., et al., *The role of perivascular and meningeal macrophages in experimental allergic encephalomyelitis.* Journal of Neuroimmunology, 2002. **122**(1): p. 1-8.
219. Hofmann, N., et al., *Increased expression of ICAM-1, VCAM-1, MCP-1, and MIP-1 alpha by spinal perivascular macrophages during experimental allergic encephalomyelitis in rats.* BMC Immunol, 2002. **3**: p. 11.
220. Polfliet, M.M., et al., *Meningeal and perivascular macrophages of the central nervous system play a protective role during bacterial meningitis.* J Immunol, 2001. **167**(8): p. 4644-50.
221. Lane, J.H., et al., *Neuroinvasion by simian immunodeficiency virus coincides with increased numbers of perivascular macrophages/microglia and intrathecal immune activation.* J Neurovirol, 1996. **2**(6): p. 423-32.
222. Williams, K.C., et al., *Perivascular macrophages are the primary cell type productively infected by simian immunodeficiency virus in the brains of macaques: implications for the neuropathogenesis of AIDS.* J Exp Med, 2001. **193**(8): p. 905-15.
223. Thompson, K.A., et al., *Cell-specific temporal infection of the brain in a simian immunodeficiency virus model of human immunodeficiency virus encephalitis.* J Neurovirol, 2009. **15**(4): p. 300-11.
224. Thompson, K.A., et al., *Brain cell reservoirs of latent virus in presymptomatic HIV-infected individuals.* Am J Pathol, 2011. **179**(4): p. 1623-9.
225. Faraco, G., et al., *Perivascular macrophages mediate the neurovascular and cognitive dysfunction associated with hypertension.* J Clin Invest, 2016. **126**(12): p. 4674-4689.
226. Santisteban, M.M., et al., *Endothelium-Macrophage Crosstalk Mediates Blood-Brain Barrier Dysfunction in Hypertension.* Hypertension, 2020. **76**(3): p. 795-807.
227. Paxinos, G. and C. Watson, *The Rat Brain in Stereotaxic Coordinates*. 1997: Academic Press.
228. Otsu, N., *A Threshold Selection Method from Gray-Level Histograms.* IEEE Transactions on Systems, Man, and Cybernetics, 1979. **9**(1): p. 62-66.
229. Jiang, H., et al., *DtiStudio: Resource program for diffusion tensor computation and fiber bundle tracking.* Computer Methods and Programs in Biomedicine, 2006. **81**(2): p. 106-116.
230. Le Bihan, D. and H. Johansen-Berg, *Diffusion MRI at 25: exploring brain tissue structure and function.* Neuroimage, 2012. **61**(2): p. 324-41.
231. Koundal, S., et al., *Optimal Mass Transport with Lagrangian Workflow Reveals Advective and Diffusion Driven Solute Transport in the Glymphatic System.* Scientific Reports, 2020. **10**(1): p. 1990.

232. Valnes, L.M., et al., *Apparent diffusion coefficient estimates based on 24 hours tracer movement support glymphatic transport in human cerebral cortex.* Scientific Reports, 2020. **10**(1): p. 9176.
233. Lacolley, P., et al., *Vascular Smooth Muscle Cells and Arterial Stiffening: Relevance in Development, Aging, and Disease.* Physiol Rev, 2017. **97**(4): p. 1555-1617.
234. Toth, P., et al., *Functional vascular contributions to cognitive impairment and dementia: mechanisms and consequences of cerebral autoregulatory dysfunction, endothelial impairment, and neurovascular uncoupling in aging.* Am J Physiol Heart Circ Physiol, 2017. **312**(1): p. H1-h20.
235. Weller, M., et al., *Glioma.* Nature Reviews Disease Primers, 2015. **1**(1): p. 15017.
236. Stupp, R., et al., *Effects of radiotherapy with concomitant and adjuvant temozolomide versus radiotherapy alone on survival in glioblastoma in a randomised phase III study: 5-year analysis of the EORTC-NCIC trial.* Lancet Oncol, 2009. **10**(5): p. 459-66.
237. Peri, C., *What Is Glioblastoma?*
238. Xia, S., et al., *Tumor microenvironment tenascin-C promotes glioblastoma invasion and negatively regulates tumor proliferation.* Neuro Oncol, 2016. **18**(4): p. 507-17.
239. Hu, X., et al., *Meningeal lymphatic vessels regulate brain tumor drainage and immunity.* Cell Res, 2020. **30**(3): p. 229-243.
240. Seker-Polat, F., et al., *Tumor Cell Infiltration into the Brain in Glioblastoma: From Mechanisms to Clinical Perspectives.* Cancers (Basel), 2022. **14**(2).
241. Karl J. Friston, J.A., Stefan Kiebel, Thomas Nichols, William Penny, ed. *Statistical Parametric Mapping: The Analysis of Functional Brain Images*. 2007, Elsevier / Academic Press, Amsterdam, 2007.
242. Xu, D., et al., *Impediment of Cerebrospinal Fluid Drainage Through Glymphatic System in Glioma.* Front Oncol, 2021. **11**: p. 790821.
243. Ma, Q., et al., *Lymphatic outflow of cerebrospinal fluid is reduced in glioma.* Scientific Reports, 2019. **9**(1): p. 14815.
244. Sahar, A., *The effect of pressure on the production of cerebrospinal fluid by the choroid plexus.* J Neurol Sci, 1972. **16**(1): p. 49-58.
245. Welch, K., *The principles of physiology of the cerebrospinal fluid in relation to hydrocephalus including normal pressure hydrocephalus.* Adv Neurol, 1975. **13**: p. 247-332.
246. Diksin, M., S.J. Smith, and R. Rahman, *The Molecular and Phenotypic Basis of the Glioma Invasive Perivascular Niche.* Int J Mol Sci, 2017. **18**(11).
247. Montana, V. and H. Sontheimer, *Bradykinin promotes the chemotactic invasion of primary brain tumors.* J Neurosci, 2011. **31**(13): p. 4858-67.
248. Calias, P., et al., *Intrathecal delivery of protein therapeutics to the brain: A critical reassessment.* Pharmacology & Therapeutics, 2014. **144**(2): p. 114-122.
249. Prins, N.D. and P. Scheltens, *Treating Alzheimer's disease with monoclonal antibodies: current status and outlook for the future.* Alzheimer's Research & Therapy, 2013. **5**(6): p. 56.

250. Banks, W.A., et al., *Passage of amyloid β protein antibody across the blood–brain barrier in a mouse model of Alzheimer's disease.* Peptides, 2002. **23**(12): p. 2223-2226.
251. Wolak, D.J., M.E. Pizzo, and R.G. Thorne, *Probing the extracellular diffusion of antibodies in brain using in vivo integrative optical imaging and ex vivo fluorescence imaging.* Journal of Controlled Release, 2015. **197**: p. 78-86.
252. Plog, B.A., et al., *Transcranial optical imaging reveals a pathway for optimizing the delivery of immunotherapeutics to the brain.* JCI Insight, 2018. **3**(20).
253. Provenzano, D.A., Z. Pellis, and L. DeRiggi, *Fatal gadolinium-induced encephalopathy following accidental intrathecal administration: a case report and a comprehensive evidence-based review.* Reg Anesth Pain Med, 2019.
254. Reeves, C., et al., *Intrathecal Injection of Gadobutrol: A Tale of Caution.* J Pain Palliat Care Pharmacother, 2017. **31**(2): p. 139-143.
255. Samardzic, D. and K. Thamburaj, *Magnetic resonance characteristics and susceptibility weighted imaging of the brain in gadolinium encephalopathy.* J Neuroimaging, 2015. **25**(1): p. 136-9.
256. Eide, P.K., et al., *Sleep deprivation impairs molecular clearance from the human brain.* Brain, 2021. **144**(3): p. 863-874.
257. Eide, P.K., et al., *Altered glymphatic enhancement of cerebrospinal fluid tracer in individuals with chronic poor sleep quality.* J Cereb Blood Flow Metab, 2022. **42**(9): p. 1676-1692.
258. Naganawa, S., et al., *Serial scans in healthy volunteers following intravenous administration of gadoteridol: time course of contrast enhancement in various cranial fluid spaces.* Magn Reson Med Sci, 2014. **13**(1): p. 7-13.
259. Jost, G., et al., *Penetration and distribution of gadolinium-based contrast agents into the cerebrospinal fluid in healthy rats: a potential pathway of entry into the brain tissue.* Eur Radiol, 2017. **27**(7): p. 2877-2885.
260. Berger, F., et al., *Gadolinium Distribution in Cerebrospinal Fluid after Administration of a Gadolinium-based MR Contrast Agent in Humans.* Radiology, 2018. **288**(3): p. 703-709.
261. Nehra, A.K., et al., *Accumulation of Gadolinium in Human Cerebrospinal Fluid after Gadobutrol-enhanced MR Imaging: A Prospective Observational Cohort Study.* Radiology, 2018. **288**(2): p. 416-423.
262. Naganawa, S., et al., *Confirmation of Age-dependence in the Leakage of Contrast Medium around the Cortical Veins into Cerebrospinal Fluid after Intravenous Administration of Gadolinium-based Contrast Agent.* Magn Reson Med Sci, 2020. **19**(4): p. 375-381.
263. Naganawa, S., et al., *Age Dependence of Gadolinium Leakage from the Cortical Veins into the Cerebrospinal Fluid Assessed with Whole Brain 3D-real Inversion Recovery MR Imaging.* Magn Reson Med Sci, 2019. **18**(2): p. 163-169.
264. van de Haar, H.J., et al., *Blood-Brain Barrier Leakage in Patients with Early Alzheimer Disease.* Radiology, 2016. **281**(2): p. 527-535.

265. Naganawa, S., et al., *Intracranial Distribution of Intravenously Administered Gadolinium-based Contrast Agent over a Period of 24 Hours: Evaluation with 3D-real IR Imaging and MR Fingerprinting.* Magn Reson Med Sci, 2021. **20**(1): p. 91-98.
266. Naganawa, S., et al., *Detection of IV-gadolinium Leakage from the Cortical Veins into the CSF Using MR Fingerprinting.* Magn Reson Med Sci, 2020. **19**(2): p. 141-146.
267. Taoka, T., et al., *Evaluation of glymphatic system activity with the diffusion MR technique: diffusion tensor image analysis along the perivascular space (DTI-ALPS) in Alzheimer's disease cases.* Jpn J Radiol, 2017. **35**(4): p. 172-178.
268. Thomas, C., et al., *Impact of time-of-day on diffusivity measures of brain tissue derived from diffusion tensor imaging.* Neuroimage, 2018. **173**: p. 25-34.
269. Demiral, S.B., et al., *Apparent diffusion coefficient changes in human brain during sleep - Does it inform on the existence of a glymphatic system?* Neuroimage, 2019. **185**: p. 263-273.
270. Tuura, R.O., et al., *Sleep-related and diurnal effects on brain diffusivity and cerebrospinal fluid flow.* Neuroimage, 2021. **241**: p. 118420.
271. Harrison, I.F., et al., *Non-invasive imaging of CSF-mediated brain clearance pathways via assessment of perivascular fluid movement with diffusion tensor MRI.* Elife, 2018. **7**.
272. Komlosh, M.E., et al., *A novel MRI phantom to study interstitial fluid transport in the glymphatic system.* Magn Reson Imaging, 2019. **56**: p. 181-186.
273. Taoka, T., et al., *Diffusion analysis of fluid dynamics with incremental strength of motion proving gradient (DANDYISM) to evaluate cerebrospinal fluid dynamics.* Jpn J Radiol, 2021. **39**(4): p. 315-323.
274. Becker, A.S., et al., *Investigation of the pulsatility of cerebrospinal fluid using cardiac-gated Intravoxel Incoherent Motion imaging.* Neuroimage, 2018. **169**: p. 126-133.
275. Surer, E., et al., *Cardiac-gated intravoxel incoherent motion diffusion-weighted magnetic resonance imaging for the investigation of intracranial cerebrospinal fluid dynamics in the lateral ventricle: a feasibility study.* Neuroradiology, 2018. **60**(4): p. 413-419.
276. Orzsik, B., et al., *Higher order diffusion imaging as a putative index of human sleep-related microstructural changes and glymphatic clearance.* Neuroimage, 2023. **274**: p. 120124.
277. Kamagata, K., et al., *Association of MRI Indices of Glymphatic System With Amyloid Deposition and Cognition in Mild Cognitive Impairment and Alzheimer Disease.* Neurology, 2022. **99**(24): p. e2648-60.
278. Ota, M., et al., *Relationships Between the Deposition of Amyloid-beta and Tau Protein and Glymphatic System Activity in Alzheimer's Disease: Diffusion Tensor Image Study.* J Alzheimers Dis, 2022. **90**(1): p. 295-303.
279. Chang, H.I., et al., *Gray Matter Reserve Determines Glymphatic System Function in Young-Onset Alzheimer's Disease: Evidenced by DTI-ALPS and Compared with Age-matched Controls.* Psychiatry Clin Neurosci, 2023.

280. Steward, C.E., et al., *Assessment of the DTI-ALPS Parameter Along the Perivascular Space in Older Adults at Risk of Dementia.* J Neuroimaging, 2021. **31**(3): p. 569-578.
281. Chen, H.L., et al., *Associations among Cognitive Functions, Plasma DNA, and Diffusion Tensor Image along the Perivascular Space (DTI-ALPS) in Patients with Parkinson's Disease.* Oxid Med Cell Longev, 2021. **2021**: p. 4034509.
282. Yokota, H., et al., *Diagnostic Performance of Glymphatic System Evaluation Using Diffusion Tensor Imaging in Idiopathic Normal Pressure Hydrocephalus and Mimickers.* Curr Gerontol Geriatr Res, 2019. **2019**: p. 5675014.
283. Bae, Y.J., et al., *Altered glymphatic system in idiopathic normal pressure hydrocephalus.* Parkinsonism Relat Disord, 2021. **82**: p. 56-60.
284. Kikuta, J., et al., *Water Diffusivity Changes Along the Perivascular Space After Lumboperitoneal Shunt Surgery in Idiopathic Normal Pressure Hydrocephalus.* Front Neurol, 2022. **13**: p. 843883.
285. Yang, G., et al., *Evaluation of Glymphatic System Using Diffusion MR Technique in T2DM Cases.* Front Hum Neurosci, 2020. **14**: p. 300.
286. Qin, Y., et al., *DTI-ALPS: An MR biomarker for motor dysfunction in patients with subacute ischemic stroke.* Front Neurosci, 2023. **17**: p. 1132393.
287. Zhang, W., et al., *Glymphatic clearance function in patients with cerebral small vessel disease.* Neuroimage, 2021. **238**: p. 118257.
288. Tian, Y., et al., *Impaired glymphatic system as evidenced by low diffusivity along perivascular spaces is associated with cerebral small vessel disease: a population-based study.* Stroke Vasc Neurol, 2023.
289. Taoka, T., et al., *Reproducibility of diffusion tensor image analysis along the perivascular space (DTI-ALPS) for evaluating interstitial fluid diffusivity and glymphatic function: CHanges in Alps index on Multiple conditiON acquIsition eXperiment (CHAMONIX) study.* Jpn J Radiol, 2022. **40**(2): p. 147-158.
290. Tatekawa, H., et al., *Improved reproducibility of diffusion tensor image analysis along the perivascular space (DTI-ALPS) index: an analysis of reorientation technique of the OASIS-3 dataset.* Jpn J Radiol, 2023. **41**(4): p. 393-400.
291. Saito, Y., et al., *Reproducibility of automated calculation technique for diffusion tensor image analysis along the perivascular space.* Jpn J Radiol, 2023.
292. Wen, Q., et al., *Assessing pulsatile waveforms of paravascular cerebrospinal fluid dynamics within the glymphatic pathways using dynamic diffusion-weighted imaging (dDWI).* Neuroimage, 2022. **260**: p. 119464.
293. Nguyen, T.D., et al., *Effective motion-sensitizing magnetization preparation for black blood magnetic resonance imaging of the heart.* J Magn Reson Imaging, 2008. **28**(5): p. 1092-100.
294. Song, A.W. and T. Li, *Improved spatial localization based on flow-moment-nulled and intra-voxel incoherent motion-weighted fMRI.* NMR Biomed, 2003. **16**(3): p. 137-43.
295. Maekawa, T., et al., *Choroid plexus cysts analyzed using diffusion-weighted imaging with short diffusion-time.* Magn Reson Imaging, 2019. **57**: p. 323-327.
296. Taoka, T., et al., *Can low b value diffusion weighted imaging evaluate the character of cerebrospinal fluid dynamics?* Jpn J Radiol, 2019. **37**(2): p. 135-144.

297. Bito, Y., et al., *Low b-value diffusion tensor imaging for measuring pseudorandom flow of cerebrospinal fluid.* Magn Reson Med, 2021. **86**(3): p. 1369-1382.
298. Taoka, T., et al., *Evaluating the Effect of Arterial Pulsation on Cerebrospinal Fluid Motion in the Sylvian Fissure of Patients with Middle Cerebral Artery Occlusion Using Low b-value Diffusion-weighted Imaging.* Magn Reson Med Sci, 2021. **20**(4): p. 371-377.
299. Jang, M., S. Han, and H. Cho, *D* from diffusion MRI reveals a correspondence between ventricular cerebrospinal fluid volume and flow in the ischemic rodent model.* J Cereb Blood Flow Metab, 2022. **42**(4): p. 572-583.
300. Boye, D., et al., *Flow dynamics of cerebrospinal fluid between the intracranial cavity and the subarachnoid space of the optic nerve measured with a diffusion magnetic resonance imaging sequence in patients with normal tension glaucoma.* Clin Exp Ophthalmol, 2018. **46**(5): p. 511-518.
301. Berberat, J., et al., *Case Report: Cerebrospinal Fluid Dynamics in the Optic Nerve Subarachnoid Space and the Brain Applying Diffusion Weighted MRI in Patients With Idiopathic Intracranial Hypertension-A Pilot Study.* Front Neurol, 2022. **13**: p. 862808.
302. Grazzini, I., D. Venezia, and G.L. Cuneo, *The role of diffusion tensor imaging in idiopathic normal pressure hydrocephalus: A literature review.* Neuroradiol J, 2021. **34**(2): p. 55-69.
303. Osawa, T., et al., *Changes in Apparent Diffusion Coefficient (ADC) during Cardiac Cycle of the Brain in Idiopathic Normal Pressure Hydrocephalus Before and After Cerebrospinal Fluid Drainage.* J Magn Reson Imaging, 2021. **53**(4): p. 1200-1207.
304. Ye, F.Q., et al., *Correction for vascular artifacts in cerebral blood flow values measured by using arterial spin tagging techniques.* Magn Reson Med, 1997. **37**(2): p. 226-35.
305. Wang, J., et al., *When perfusion meets diffusion: in vivo measurement of water permeability in human brain.* J Cereb Blood Flow Metab, 2007. **27**(4): p. 839-49.
306. Valnes, L.M., et al., *Apparent diffusion coefficient estimates based on 24 hours tracer movement support glymphatic transport in human cerebral cortex.* Sci Rep, 2020. **10**(1): p. 9176.
307. Wymer, D.T., et al., *Phase-Contrast MRI: Physics, Techniques, and Clinical Applications.* Radiographics, 2020. **40**(1): p. 122-140.
308. Yamada, S., et al., *Current and emerging MR imaging techniques for the diagnosis and management of CSF flow disorders: a review of phase-contrast and time-spatial labeling inversion pulse.* AJNR Am J Neuroradiol, 2015. **36**(4): p. 623-30.
309. Korbecki, A., et al., *Imaging of cerebrospinal fluid flow: fundamentals, techniques, and clinical applications of phase-contrast magnetic resonance imaging.* Pol J Radiol, 2019. **84**: p. e240-e250.
310. Tawfik, A.M., et al., *Phase-Contrast MRI CSF Flow Measurements for the Diagnosis of Normal-Pressure Hydrocephalus: Observer Agreement of Velocity Versus Volume Parameters.* AJR Am J Roentgenol, 2017. **208**(4): p. 838-843.

311. Sharma, A.K., et al., *Measurement of peak CSF flow velocity at cerebral aqueduct, before and after lumbar CSF drainage, by use of phase-contrast MRI: utility in the management of idiopathic normal pressure hydrocephalus.* Clin Neurol Neurosurg, 2008. **110**(4): p. 363-8.
312. Konig, R.E., et al., *Phase-Contrast MRI Detection of Ventricular Shunt CSF Flow: Proof of Principle.* J Neuroimaging, 2020. **30**(6): p. 746-753.
313. Kartalci, S., et al., *Evaluation of CSF flow dynamics in patients with schizophrenia using phase-contrast cine MRI.* Psychiatry Res, 2021. **304**: p. 114172.
314. Wagshul, M.E., et al., *Amplitude and phase of cerebrospinal fluid pulsations: experimental studies and review of the literature.* J Neurosurg, 2006. **104**(5): p. 810-9.
315. Mohammadi, H., et al., *Cortical thinning is associated with brain pulsatility in older adults: An MRI and NIRS study.* Neurobiol Aging, 2021. **106**: p. 103-118.
316. Ma, L., et al., *Decreased CSF Dynamics in Treatment-Naive Patients with Essential Hypertension: A Study with Phase-Contrast Cine MR Imaging.* AJNR Am J Neuroradiol, 2021. **42**(12): p. 2146-2151.
317. Patel, R.P., et al., *Phase-contrast cerebrospinal fluid flow magnetic resonance imaging in qualitative evaluation of patency of CSF flow pathways prior to infusion of chemotherapeutic and other agents into the fourth ventricle.* Childs Nerv Syst, 2018. **34**(3): p. 481-486.
318. Saliou, G., et al., *A phase-contrast MRI study of acute and chronic hydrodynamic alterations after hydrocephalus induced by subarachnoid hemorrhage.* J Neuroimaging, 2012. **22**(4): p. 343-50.
319. Attier-Zmudka, J., et al., *Decreased Cerebrospinal Fluid Flow Is Associated With Cognitive Deficit in Elderly Patients.* Front Aging Neurosci, 2019. **11**: p. 87.
320. ElSankari, S., et al., *Concomitant analysis of arterial, venous, and CSF flows using phase-contrast MRI: a quantitative comparison between MS patients and healthy controls.* J Cereb Blood Flow Metab, 2013. **33**(9): p. 1314-21.
321. Pujol, J., et al., *Motion of the cerebellar tonsils in Chiari type I malformation studied by cine phase-contrast MRI.* Neurology, 1995. **45**(9): p. 1746-53.
322. Akay, R., et al., *Evaluation of aqueductal CSF flow dynamics with phase contrast cine MR imaging in idiopathic intracranial hypertension patients: preliminary results.* Eur Rev Med Pharmacol Sci, 2015. **19**(18): p. 3475-9.
323. Jaeger, M., et al., *Relationship between intracranial pressure and phase contrast cine MRI derived measures of intracranial pulsations in idiopathic normal pressure hydrocephalus.* J Clin Neurosci, 2016. **33**: p. 169-172.
324. Ringstad, G., K.E. Emblem, and P.K. Eide, *Phase-contrast magnetic resonance imaging reveals net retrograde aqueductal flow in idiopathic normal pressure hydrocephalus.* J Neurosurg, 2016. **124**(6): p. 1850-7.
325. Sakhare, A.R., G. Barisano, and J. Pa, *Assessing test-retest reliability of phase contrast MRI for measuring cerebrospinal fluid and cerebral blood flow dynamics.* Magn Reson Med, 2019. **82**(2): p. 658-670.
326. Muccio, M., et al., *Upright versus supine MRI: effects of body position on craniocervical CSF flow.* Fluids Barriers CNS, 2021. **18**(1): p. 61.

327. Yildiz, S., et al., *Immediate impact of yogic breathing on pulsatile cerebrospinal fluid dynamics.* Sci Rep, 2022. **12**(1): p. 10894.
328. Kollmeier, J.M., et al., *Deep breathing couples CSF and venous flow dynamics.* Sci Rep, 2022. **12**(1): p. 2568.
329. Oner, Z., et al., *Quantitative Evaluation of Normal Aqueductal Cerebrospinal Fluid Flow Using Phase-Contrast Cine MRI According to Age and Sex.* Anat Rec (Hoboken), 2017. **300**(3): p. 549-555.
330. Spijkerman, J.M., et al., *Phase contrast MRI measurements of net cerebrospinal fluid flow through the cerebral aqueduct are confounded by respiration.* J Magn Reson Imaging, 2019. **49**(2): p. 433-444.
331. Peng, S.L., et al., *Optimization of phase-contrast MRI for the quantification of whole-brain cerebral blood flow.* J Magn Reson Imaging, 2015. **42**(4): p. 1126-33.
332. Magdoom, K.N., et al., *Phase contrast MRI of creeping flows using stimulated echo.* J Magn Reson, 2019. **299**: p. 49-58.
333. Walker-Samuel, S., et al., *Investigating Low-Velocity Fluid Flow in Tumors with Convection-MRI.* Cancer Res, 2018. **78**(7): p. 1859-1872.
334. Williamson, N.H., et al., *Limits to flow detection in phase contrast MRI.* J Magn Reson Open, 2020. **2-3**.
335. Kudo, K., et al., *Indirect Proton MR Imaging and Kinetic Analysis of (17)O-Labeled Water Tracer in the Brain.* Magn Reson Med Sci, 2018. **17**(3): p. 223-230.
336. Tailor, D.R., et al., *Indirect 17(O)-magnetic resonance imaging of cerebral blood flow in the rat.* Magn Reson Med, 2003. **49**(3): p. 479-87.
337. Igarashi, H., et al., *Water influx into cerebrospinal fluid is primarily controlled by aquaporin-4, not by aquaporin-1: 17O JJVCPE MRI study in knockout mice.* Neuroreport, 2014. **25**(1): p. 39-43.
338. Naganawa, S., et al., *The Glymphatic System in Humans: Investigations With Magnetic Resonance Imaging.* Invest Radiol, 2023.
339. Connor, S.E., et al., *SPAMM, cine phase contrast imaging and fast spin-echo T2-weighted imaging in the study of intracranial cerebrospinal fluid (CSF) flow.* Clin Radiol, 2001. **56**(9): p. 763-72.
340. Sakas, D.E., et al., *Chiari malformation: CSF flow dynamics in the craniocervical junction and syrinx.* Acta Neurochir (Wien), 2005. **147**(12): p. 1223-33.
341. Yamada, S., et al., *Visualization of cerebrospinal fluid movement with spin labeling at MR imaging: preliminary results in normal and pathophysiologic conditions.* Radiology, 2008. **249**(2): p. 644-52.
342. Yamada, S., *Cerebrospinal fluid physiology: visualization of cerebrospinal fluid dynamics using the magnetic resonance imaging Time-Spatial Inversion Pulse method.* Croat Med J, 2014. **55**(4): p. 337-46.
343. Ohene, Y., et al., *Non-invasive MRI of brain clearance pathways using multiple echo time arterial spin labelling: an aquaporin-4 study.* Neuroimage, 2019. **188**: p. 515-523.

344. Oshio, K., et al., *The Spatial Distribution of Water Components with Similar T(2) May Provide Insight into Pathways for Large Molecule Transportation in the Brain.* Magn Reson Med Sci, 2021. **20**(1): p. 34-39.
345. Fultz, N.E., et al., *Coupled electrophysiological, hemodynamic, and cerebrospinal fluid oscillations in human sleep.* Science, 2019. **366**(6465): p. 628-631.
346. Rudie, J.D., et al., *Neuroimaging of Dilated Perivascular Spaces: From Benign and Pathologic Causes to Mimics.* J Neuroimaging, 2018. **28**(2): p. 139-149.